UNIVERSITY *of* TASMANIA

A STEP TOWARDS FULLY AUTOMATED 3D PRINTED INSTRUMENTS

By

Farhan Cecil (M. Phil)

School of Physical Sciences

Submitted in fulfilment of the requirement for the Degree of

Doctor of Philosophy

University of Tasmania (July 2018)

DECLARATION

This thesis contains no material which has been accepted for a degree or diploma by the University or any other institution, except by way of background information and duly acknowledged in the thesis, and to the best of my knowledge and belief no material previously published or written by another person except where due acknowledgement is made in the text of the thesis, nor does the thesis contain any material that infringes copyright.

The publishers of the papers in this thesis (comprising Chapters Two to Four) hold the copyright for that content, and access to the material should be sought from the respective journals. The remaining non-published content of the thesis may be made available for loan and limited copying and communication in accordance with the Copyright Act 1968.

The research associated with this thesis abides by the international and Australian codes on human and animal experimentation, the guidelines by the Australian Government's Office of the Gene Technology Regulator and the rulings of the Safety, Ethics and Institutional Biosafety Committees of the University.

Farhan Cecil

2018

3D print

I like to make design and 3D print

But it is not as easy as you think to 3D print

There are issues always with the 3D print

I design detection devices and pumps and 3D print

Some of them work and some not which I 3D print

I am not sure, it was a good idea or not, to 3D print

But still I like to 3D print

By Farhan Cecil

Acknowledgements

I would like to express my sincere gratitude to my supervisor Prof. Michael Breadmore for all his help and support and for making my PhD journey such a great experience despite of all the twists and turns.

I would also like to thank my co-supervisor, Prof. Mirek Macka, for giving me this opportunity to work on such an exciting project and for his contributions to my project. I am also grateful to my co-supervisors, Prof. Rossane Gujit, for insightful discussions, comments and ideas, and Dr. Alan Henderson for suggestions and comments.

Special thanks to Prof. Brett Paull and Prof. Andrew Cole for being part of my supervision team in my first two years. I am also thankful to Jason Smith for being supportive during my PhD and Prof. Emily Hilder for always being very supportive, helping, and encouraging.

I would also like to acknowledge Murray frith, Carol Jacobs and Trish MacKay for their support and co-operation. My gratitude also extends to all my PhD friends specially Ibraam Mikhail, Adam Sutton, Chris Desire, Leo Lebanov, Nirved Upadhyay, Gabriela Cabarrus, Mostafa Ade, Arif Islam, Daniel Gstottenmayr l and Estrella Estrella Rodriguez for all the good memories

Last but not the least; I am thankful to all my family members specially my mom for listening to all my problems about my research even when she had no idea about it. I would also like to thank my best friend and my love for always being there for me during my PhD and being still with me!

Statement of Co-Authorship

Most of the work presented in this thesis was published and include

the contribution of the following authors:

Paper 1.F. Cecil.; M. Zhang, R. M. Guijt, A. Henderson, P. N. Nesterenko, B. Paull, M. C. Breadmore, M. Macka. 3D printed LED based on-capillary detector housing with integrated slit. (2017) Analytica Chimica Acta. http://dx.doi.org/10.1016/j.aca.2017.02.020

This paper constitutes Chapter Two. Mr. Farhan Cecil was the first author and conducted all the experimental work, data analysis and writing the manuscript.

Dr. Min Zhang assisted in metal detection analysis using the 3D printed device. Dr. Alan Henderson, Prof. Rosanne Guijt, Prof. Brett Paull, Prof. Pavel Nestrenko, Prof. Mirek Macka and Prof. Micheal Breadmore contributed equally to the idea, refinement of the 3D design of the device, assistance with specialized instrumentation and development of the work.

Paper 2. F. Cecil, R. M. Guijt, A. Henderson, M. Macka, M. C. Breadmore. One step multi material 3D printing for the fabrication of photometric detector flow cell. (2019) (submitted)

This paper constitutes Chapter Three. Mr. Farhan Cecil was the first author and conducted all the experimental work, data analysis and writing the manuscript.

Dr. Alan Henderson, Prof. Rosanne Guijt, Prof. Mirek Macka and Prof. Micheal Breadmore contributed equally to the idea, refinement of the 3D design of the device, assistance with specialized instrumentation and development of the work.

Paper 3. F. Cecil, R. M. Guijt, A. Henderson, M. Macka, M. C. Breadmore. Non-Terminal Electroosmotic Pump Made by Multi-material 3D Printing. (2019) (submitted)

This paper constitutes Chapter Three. Mr. Farhan Cecil was the first author and conducted all the experimental work, data analysis and writing the manuscript.

Dr. Alan Henderson, Prof. Rosanne Guijt, Prof. Mirek Macka and Prof. Micheal Breadmore contributed equally to the idea, refinement of the 3D design of the device, assistance with specialized instrumentation and development of the work.

We the undersigned agree with the above stated proportion of the work undertaken for each of the above published peer-reviewed manuscript's contributing to this thesis:

Signed:

Professor Michael Breadmore	Professor Mark Hunt
Supervisor	Head of School
School of Natural Sciences	School of Natural Sciences
University of Tasmania	University of Tasmania

Date 2/7/2018

List of Publications

Type of publication	Number
Research articles in peer reviewed journals	3
Oral presentations at international and national conferences	6
Poster presentations at international and national conferences	8

1. F. Cecil.; M. Zhang, R. M. Guijt, A. Henderson, P. N. Nesterenko, B. Paull, M. C. Breadmore, M. Macka. 3D printed LED based on-capillary detector housing with integrated slit. Analytica Chimica Act. (http://dx.doi.org/10.1016/j.aca.2017.02.020)

2. F. Cecil, R. M. Guijt, A. Henderson, M. Macka, M. C. Breadmore. One step multi material 3D printing for the fabrication of photometric detector flow cell. (2018) (submitted)

3. F. Cecil, R. M. Guijt, A. Henderson, M. Macka, M. C. Breadmore. Non-Terminal Electroosmotic Pump Made by Multi-material 3D Printing. (2018) (submitted)

4. F. Cecil, M. C. Breadmore, R. M. Guijt, B. Paull, P. N. Nesterenko, A. Henderson, A. Cole, M. Macka. 3D Printed on-capillary photometric detector "Australian Center for Research on Separation Sciences Annual Meeting" Hobart, Australia (09-10 July 2015) Oral

5. F. Cecil, P. Smejkal, P. N. Nesterenko, M. C. Breadmore, A. Henderson, A. Cole, R. M. Guijt, B. Paull Macka. Low cost on-capillary photometric detector for multiple detection tubing's fabricated by 3D printing. "23rd Annual Royal Australian Chemical

Institute Research and Development Topics Conference" Melbourne, Australia (06-09 Dec 2015). Oral

6. F. Cecil, M. C. Breadmore, R. M. Guijt, B. Paull, P. N. Nesterenko, A. Henderson, A. Cole, M. Macka. 3D printing in rapid design of led on-capillary detection devices. "40th International Symposium On Capillary Chromatography and The '13th Gc×Gc Symposium". Riva del Garda, Italy (May 29 – June 03, 2016) Oral

7. F. Cecil, M. C. Breadmore, R. M. Guijt, B. Paull, P. N. Nesterenko, A. Henderson, A. Cole, M. Macka. 3D printing in rapid design of led on-capillary detection devices. "40th International Symposium On Capillary Chromatography and The '13th Gc×Gc Symposium". Riva del Garda, Italy (May 29 – June 03, 2016) Oral

8. F. Cecil, M. Zhang, R. M. Guijt, A. Henderson, M. Macka and Michael C. Breadmore. 3D printing (Fused deposition modelling) for the fabrication of detection devices for microfluidics. "RACI Centenary Congress". Melbourne, Australia (23rd -28th July 2017) Oral

9. F. Cecil, M. Zhang, R. M. Guijt, A. Henderson, M. Macka and Michael C. Breadmore. Fused deposition modelling 3D printing for the fabrication of detection devices. "Australia New Zealand Nano-Microfluidics Symposium (ANZNMF) symposium". Hobart, Australia (26^{th} -29^{th} June 2017) Oral

10. F. Cecil, R. M. Guijt, A. Henderson, M. Macka and M. C. Breadmore. A step towards fully automated 3D printed Instruments "Australia New Zealand Nano-Microfluidics Conference (ANZNMF)". Auckland, New Zealand (27-29 June 2018) Oral

11. F. Cecil, M. Zhang, R. M. Guijt, A. Henderson, M. Macka and M. Breadmore. 3D Printing with Focus on Fused Deposition Modelling for the Fabrication of Detection Devices for Microfluidics “46th International symposium on High Performance Liquid Phase Separations and related techniques (HPLC 2017)”. Jeju, South Korea (05-09 November 2017) Poster

12. F. Cecil, M. C. Breadmore, R. M. Guijt, B. Paull, P. Nesterenko, A. Henderson, A. Cole and M. Macka. Low cost 3D printed LED based on-capillary detector suited for varying tubing diameters “7th Australia New Zealand Nano-Microfluidics Symposium (ANZNMF) symposium”. Brisbane, Australia (21st -23rd march 2016) Poster

13. F. Cecil, M. C. Breadmore, R. M. Guijt, B. Paull, P. Nesterenko, A. Henderson, A. Cole and M. Macka. The role of spatial orientation in FDM 3D printing to spatial definition of printed slit and optical detection performance “The Pittsburgh Conference on Analytical Chemistry and Applied Spectroscopy Pittcon conference and Expo 2017”. Chicago USA (03-09 March. 2017). Poster

14. F. Cecil, M. C. Breadmore, R. M. Guijt, B. Paull, P. Nesterenko, A. Henderson, A. Cole and M. Macka. Low cost FDM 3D printing and its role in spatial orientation of printing slit and detection. “ASASS 2 - ACROSS International Symposium on Advances in Separation Science”. Hobart Australia (30th Nov.-2nd Dec. 2016). Poster

15. F. Cecil, M. C. Breadmore, R. M. Guijt, B. Paull, P. Nesterenko, A. Henderson, A. Cole and M. Macka. Relating spatial orientation in 3D printing to spatial definition of slit and performance of optical detector. “Royal Australian Chemical Institute RACI Analytical and Environmental Chemistry Division Symposium (Adelaide 18-20 July 2016). Poster

16. F. Cecil, M. C. Breadmore, R. M. Guijt, B. Paull, P. Nesterenko, A. Henderson, A. Cole and M. Macka. Low cost 3D printed led based on-capillary detector suited for varying tubing diameters “7th Australia New Zealand Nano-Microfluidics Symposium (ANZNMF) symposium”. Brisbane, Australia (21st -23th march 2016) Poster

17. F. Cecil, M. C. Breadmore, R. M. Guijt, B. Paull, P. Nesterenko, A. Henderson, A. Cole and M. Macka. The role of spatial orientation in 3D printing to spatial definition of printed slit and detection performance. “Graduate research conference University of Tasmania”. Hobart Australia (01-02 September 2016) Poster

18. F. Cecil, P. Smejkal, N. Nuchtavorn, M. C. Breadmore, A. Henderson, A. Cole, M. Macka. 3D Printed on-capillary photometric detection/sensors"22nd Annual RACI R&D Topics Conference" Finder University Adelaide Australia (13-15 December 2014) Poster

List of Abbreviations

ABS	Acrylonitrile butadiene styrene
Abs.	Absorbance
AU	Absorbance units
BGE	Background electrolyte
CAD	Computer aided design
CE	Capillary electrophoresis
CNC	Computer Numerical Control
Conc.	Concentration
3D	Three dimensional
E	Molar absorptivity constant
EDM	Electro discharge manufacturing
EOF	Electroosmotic flow
EOP	Electroosmotic pump
FDM	Fused deposition modelling
FIA	Flow injection analysis
GND	ground voltage

I	Intensity of the radiation beam incident upon the sample cell for that wavelength
I_0	Intensity of the radiation beam incident upon the reference cell
kV	kilo volts
LED	Light emitting diodes
LC	Liquid chromatography
LOD	Limit of detection
mAU	Milli absorbance unit
mm	Millimetre
nL	Nanoliter
nm	Manometer
Orange G	1-phenylazo-2-naphthol-6,8-disulfonic acid disodium salt
Pa	Pressure
PAR	4-(2-pyridylazo) resorcinol, monosodium salt hydrate
PLA	Ploylactic acid
RSD	Relative standard deviation
Sen.	Sensitivity
S/N	Signal to noise ratio

STL	Stereolithography
TAPS	N-tris[Hydroxymethyl]methyl-3-aminopropane-sulphonic acid
UV	Ultra voilet
V	Voltage
ℓ	Pathlength (units of measurement)
µm	Micrometre
%	Percentage
µA	Microampere

Abstract

In the past few decades, significant advancement has been made towards the development of automated microfluidic platforms because of their unique advantages such as integration of different functions, minimum consumption of samples/reagents, low cost, and quick sample analysis. Various components of an instrument e.g. detectors, flow cell, pumps etc., are usually customised in order to improve instrument performance in terms of analysis time, liquid sample and reagents consumption, and reliability through automation. 3D printing, a rapidly growing manufacturing technique, is an attractive alternative to traditional manufacturing techniques (e.g. subtractive manufacturing) because of its ability to print almost any structure on demand with minimal time and cost. The focus of this study was to fabricate and characterise key components of the microfluidic systems including detectors, flow cell, and pumps, and potentially integrate them to produce automated analytical instrument for application in microfluidics.

First, this study explored the potential of a commonly available low cost FDM 3D printer to manufacture a photometric detector body consisting of integrated slit and hollow structures, to position a LED and photodiode, on either side of capillary tubing (Chapter 2). The spatial orientation for printing was investigated to facilitate the printing of a narrow size slit suitable for capillaries and tubing (i.d. 50 μm to 10 mm). A slit of 70 μm was printed when the slit was positioned in the XY plane in parallel with the print direction. The detection body with integrated slit showed satisfactory performance for both large diameter tubing and narrow capillaries. The performance of the 3D printed housing with a 70 μm slit was compared with a commercial CE interface for the CE separation of Zn^{2+} and Cu^{2+} complexes with PAR.

The second aim of this study was to develop a flow cell with an integrated channel to avoid the need for external capillaries and tubing. Chapter 3 describes the use of multi-material 3D printing technology for the fabrication of a complex photometric detector flow cell with integrated channel and slit. Multi material 3D printing allowed the fabrication of detection window using transparent material, and channel and flow cell body using an opaque material, all printed in one piece. The flow-cell was optimised by varying the design features including slit dimension and optical path-length. The performance of the printed flow cell devices was characterised with a standard dye solution by determining the stray light %, effective path-length and the signal to noise ratio. A device consisting of 500 µm slit with 10 mm optical path-length showed best performance.

Third, the use of multi-material FDM 3D printing to manufacture an electroosmotic pump (EOP) with multiple functionalities was investigated as fluid pumping is a key feature of a microfluidic system and usually requires a micro pump manipulate liquid flow at a smaller scale (≤ 1 mm). Chapter 4 presents the first use of this technology for the fabrication of an EOP with integrated electrodes in a single piece. The key component of the EOP is a multiple channel (mesh) and integrated 3D printed electrodes. The novel design feature, mesh was used to create the first asymmetrical surface-area EOP. The EOP was printed by using a non-conductive Acrylonitrile butadiene styrene (ABS) and a conducting ABS material was used for printing of the three electrodes around the pumping channel. These three electrodes were printed to provide an electrode for applying the voltage and two electrodes to ground the liquid within the EOP by decoupling the electric field in the pump channels from the other parts of the device. The newly developed EOP was characterised by calculating current, flow rate and pressure at various voltages ranging from 0.1- 0.5 kV. The satisfactory performance of the 3D printed EOP showed the potential of multi-material 3D printing as an alternative

approach for the fabrication of low-cost microfluidic pumping devices. Repeatability and accuracy of the fabrication method is critical for the manufacturing of reliable devices and instruments. Chapter 5 describes the repeatability and accuracy experiments conducted to investigate the repeatability and accuracy of the printing method for the manufacturing of newly developed devices presented in this thesis.

Table of Contents

Chapter 1 Introduction and Literature Review

1.1. 3D printing

3D printing, also known as additive manufacturing, has become increasingly popular in the past few decades as a versatile and inexpensive technology [1-4]. 3D printing is expanding immensely in more or less all fields of science and technology [5, 6]. It has applications in medical science to engineering, chemical science to forensic science, fashion industry to food industry [1-4, 7-21], and now it comes to the point that it can replicate itself as well [22, 23]. The remarkable thing about 3D printers is that a 3d printer can be purchased for less than $500 and can be used for variety of materials in 3D printing from plastic to metals [24].

In 3D printing the digital designs are transformed into physical models by printing layer by layer until the whole object is completed [25-27]. For 3D printing, complex three dimensional objects are designed by freely available computer aided design (CAD) drawing software, converted to STL files by slicing software like “Kissslicer” freely available at www.kisslicer.com, and are printed layer-by-layer until the whole object is fully printed [28-30].

3D printing allows fabrication of the prototype or design on demand and it can be shared on the internet or as a part of a research publication to share the technology between the researchers in a reproducible manner [30-32]. The ability to print designs on demand has made this technique highly suitable for fabrication of detection and reaction devices with complex features [33-40]. 3D printing is becoming increasingly popular in all areas of research due to low cost, quick fabrication, and a wide range of available materials, and simplicity of fabrication advantages [41-43]. The following

sections describe the most common methods of additive manufacturing and their working principle.

1.1.1. Stereolithography

Stereolithography (SLA or SL) is one of the oldest and most commonly used printing approaches. Typical SLA based printers utilize a computer controlled focused laser beam for the polymerisation of each resin layer until the whole object is fabricated [44-48]. A typical SLA set-up consists of a vat, moving platform, light source and a

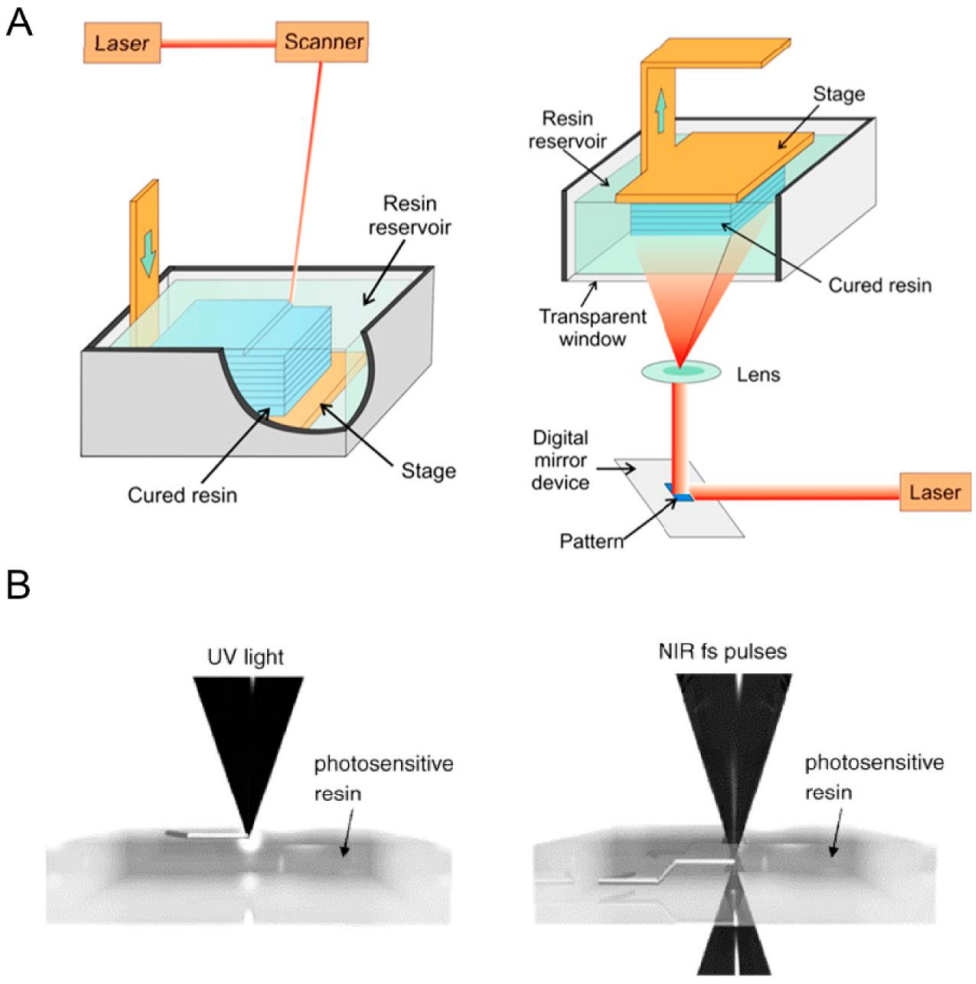

Fig.1.1. Schematic diagram of bath configuration of SLA printing (fig. taken from the reference) [7]

photopolymerisable resin (Fig.1.1). Free surface also known as bath configuration and constrained surface configurations are generally used to describe the print orientations in SLA. In free surface configuration, the platform stage descends into the reservoir containing the resin while each layer is polymerised at the surface of the photocurable resin with the help of a light source, usually a UV laser [7, 48-64]. A major obstacle to free radical polymerisation of photocurable resins is oxygen inhibition resulting in delays and reduced resolution. However, efforts to control oxygen inhibition through continuous liquid interface production, in which an oxygen permeable window (thickness maintained at the order of tens of micrometres) is created to generate a dead zone resulting in inhibition of photopolymerization between the window and the cured part, resulting in reduced printing time and improved resolution. The other limitation of this configuration is that the product height is limited by the height of the resin reservoir. Contrary to this in constrained surface configuration the printing stage is reversed to facilitate polymerisation at the bottom of the resin vat which is separated from the UV source through a transparent window. The build stage rises slightly after polymerization of each layer and the resulting void is filled by the resin and the polymerisation process continues. The advantages of the constrained configuration include minimum resin consumption, fast curing time and the building platform does not restrict the height of the final product. Although SLA based printers can provide high resolution (<25 μm) there is only limited number of commercially available printable materials which restrict the use of this technique for certain applications. For example, printing of detectors and detection devices, particularly a photometric detector, requires an opaque material and electronic devices which require conducting material are difficult to achieve using this

approach. A multi-material stereolithography (MMSL) system containing four resins has been developed[65]. This system provides the opportunity to print using multiple material allowing the integration of components or structures of variable functionality in to a single object. However, they are expensive and time consuming in terms of moving the printed body between the various resins making this technique less suitable.

1.1.2. Inkjet Printing

The working principle of Inkjet printing is similar to the classic inkjet office printers in which a jet is used to propel tiny droplets of ink on to the surface of a paper. However, in the inkjet 3D printer, thermoplastic and wax materials are used instead of ink. Typical inkjet printer consists of two reservoirs, containing the build material in one and support material in other [66-84]. The materials are propelled in the form of tiny droplets from the print head, moving in x-y plane to form printing structure layer-by-layer. The deposited materials solidify instantly because of cooling for thermoplastic materials or UV radiation in case of photo-curable resins. After printing of each layer, a milling roller moves across the surface to smoothly finish each layer. Fig.1.2 shows a typical inkjet printer employing thermoplastic print material. Although inkjet 3D printers provide excellent surface finish and high resolution, their use is limited by the cost, slow build speed, narrow range of print material and difficulty in removing the wax materials.

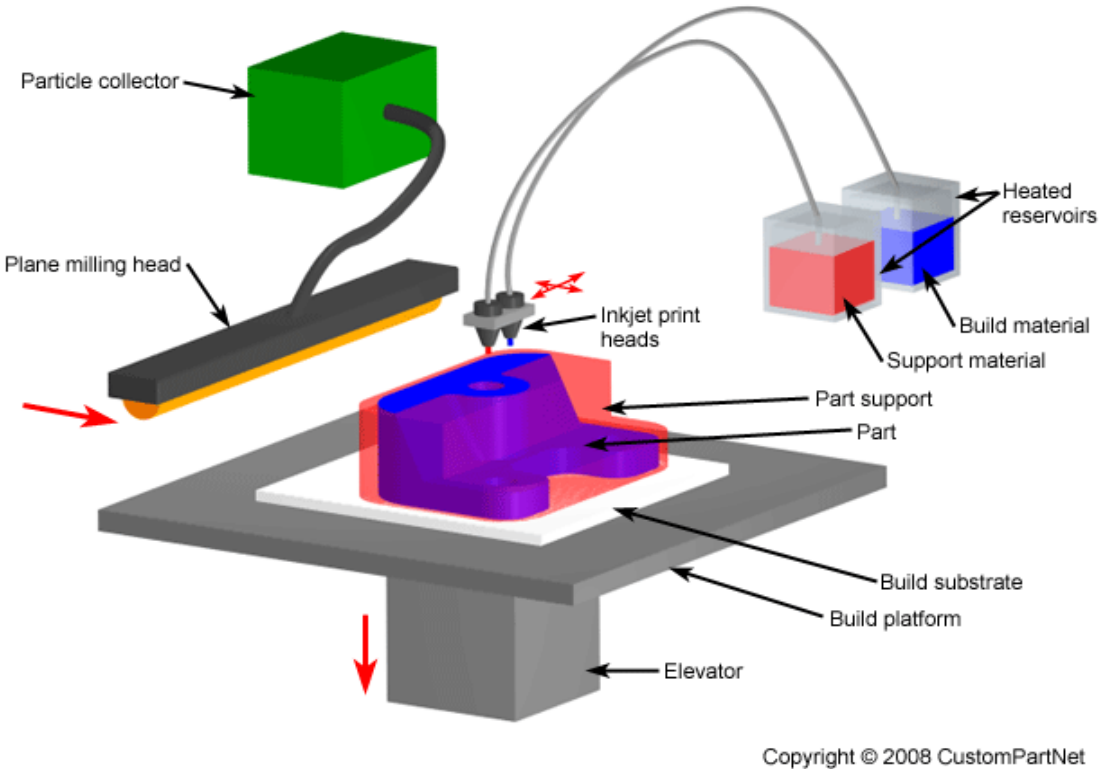

Fig.1.2. Schematic of inkjet printing process (fig. taken from the reference) [85]

1.1.3. Fused deposition modelling printing

FDM 3D printing, also known as thermoplastic extrusion, was developed by Scott Cramp in the early 1990s is one of the most cost efficient and widely used printing approaches [85, 86] In FDM, a thermoplastic is extruded through a heated nozzle and deposited layer-by-layer onto a moveable printing platform. The printing bed descends after the completion of printing of each layer and the process continuous until the whole object is fabricated [87-98]. (Fig.1.3). In FDM as the filament is extruded through

a round nozzle, the resulting layers have round profile that leads to a grainy finish and therefore limiting the resolution and surface smoothness [8]. The low resolution of FDM 3D printer (XYZ, 300 × 300 × 50 µm) particularly in the xy plane as previously reported by McDonalds *et al* (321 ± 5 µm) particularly in the XY plane showed the incompatibility of this technique for manufacturing features with small dimension [99].However, efforts to improve the surface quality by manipulating the print direction shows great opportunities to overcome the current limitation of low resolution. For example; Wang et al proposed a segmentation method suggesting the partitioning of the printing model into several pieces to allow printing of each piece in a direction that produced minimum error and surface roughness [100]. Furthermore, continuous development in FDM printers improving print quality and reducing cost and an ever increasing number of thermoplastic materials including poly(lactic acid) (PLA), poly(vinyl alcohol) (PVA), acrylonitrile-butadiene-styrene (ABS), poly(carbonate) (PC), nylon, poly(ethylene terephthalate) (PET), nylon, thermoplastic elastomers (TPE) and an increasing variety of functional materials) [101, 102] make FDM a technique of choice for a wide range of applications.

Additionally, printers with multiple nozzles capable of printing multiple materials can be used during printing to fabricate a sacrificial support or devices with integrated components of variable functions. Multi-material FDM printers allow the fabrication of parts with different properties in a single device during a print. Materials with different properties (e.g. porosity, thermal or electrical conductivity, rigidity etc.), are chosen prior to the fabrication process to produce devices/systems containing parts of different functional properties. Multi-material FDM 3D printers have been employed for fabrication of analytical devices with integrated components of varying properties.

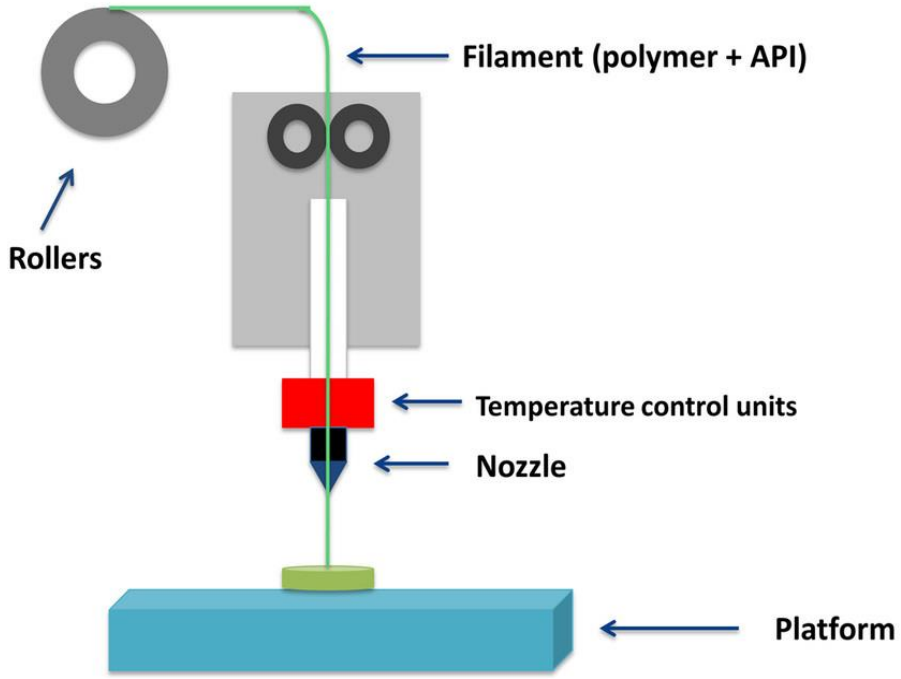

Fig.1.3. Schematic of FDM 3D printing (fig. taken from the reference). [86]

For example, Li et al., (2016) recently used ABS for printing the microfluidic device and LayFelt material, containing a water soluble polyvinyl alcohol (PVA) component, for membrane fabrication using a dual head FDM 3D printer in a single print run [103].

The advantages of FDM such as; no post-processing of the print (such as wax removal), low cost, and availability of a wide range of materials make it a very attractive technique for the fabrication of low cost customised analytical devices and instruments [1].

The aim of this project is to explore the potential of low cost FDM 3D printing for customisation and integration of various components of an instrument e.g. detectors, flow cell, pumps etc. that can potentially be used to develop a fully integrated automated miniaturised analytical instrument.

1.2. Analytical instrumentation

Analytical instruments are used to obtain qualitative and/or quantitative information about the composition of an unknown samples, such as the presence or absence of certain components in a sample [104]. Modern analytical instruments have evolved from the traditional methods that relied on mass or volumes measurement. For example, titrimetric analysis, a commonly used laboratory-based method relies on volume measurement to determine the concentration of a known analyte. In tritrimetry a known volume and concentration of the standard solution (titrant) reacts with the solution of analyte and its concentration is estimated by measuring the volume of the titrant reacted. The main drawbacks of the classical methods include time consumption, contamination due to manual handling, low sensitivity and non-automation. In contrast to classical methods, modern analytical instruments provide the distinct benefits including; quick analysis, improved accuracy due to elimination of errors from personal bias, enhanced sensitivity and improved performance due to automation.

Flow injection analysis (FIA) is one of the simplest analytical techniques with simple instrumentation. It is based on the injection of a liquid sample into a flowing carrier stream of a suitable liquid [105-107]. The injected sample is transported toward a detector which continuously records the changes in absorbance, in case of the photometric detector, resulting from the passage of the sample material through the flow cell. The simplest FIA system consists of a pump, which is used to transport fluid; an injection port, a reaction/mixing chamber [108] which is used to conduct the

reaction of the sample components with the carrier stream forming a species, and a detector to record the signals (Fig.1.4).

The following sections will provide details on key components of the analytical instrument including; pump, flow cell and detectors and the application of 3D printing, if any, for the fabrication of these components.

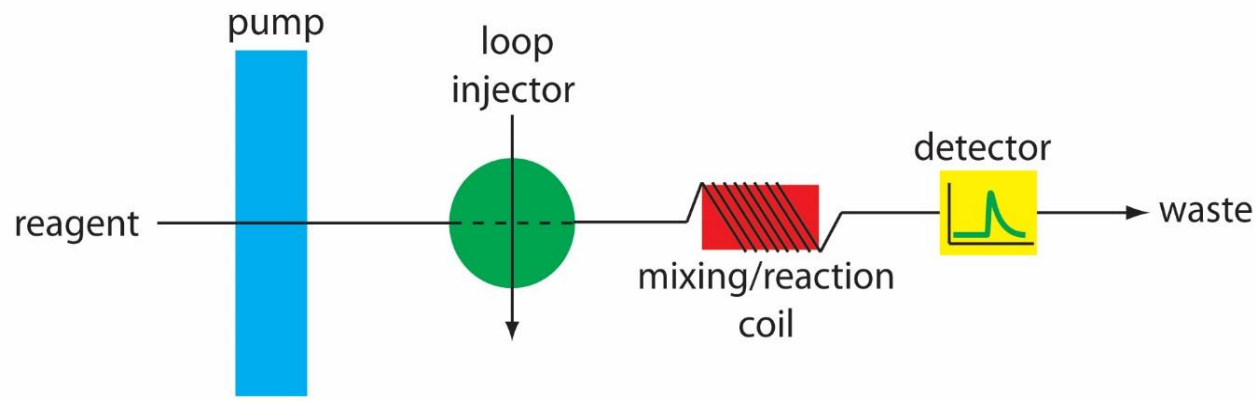

Fig.1.4: Schematic representation of the elementary components of a simple FIA instrument (Fig. taken from the reference). [106]

1.2.1. Detectors/ detection Assembly

In recent years, there has been an increasing demand for the customisation and integration of the detectors/ detection assemblies within the microfluidic systems due to low volume sample handling and faster response time advantages. Integrated microfluidic systems allow sample introduction directly to the detection techniques thus introducing automation through minimising sample handling and human intervention. Optical detection techniques e.g. absorption photometric, chemiluminescence or fluorescence are commonly used to record the analyte signals

after separation in capillary electrophoresis or liquid chromatography or colour-forming reaction in FIA system.

Photometric detection is the most frequently used detection technique due to its operational simplicity and low cost. In a photometric detection assembly, the concentration of the analyte is measured as it passes through the flow channel and the flow cell of the detector. The photometric detector delivers signal in the form of current or voltage which is proportional to the impinging photons which is recorded in the form of a peak, the signal intensity changes based on the light absorbed by the liquid, by measuring the difference in the absorbance of the analyte and the buffer. A typical photometric detector consists of a light source (e.g. LED), a flow cell, and a light sensor or photodiode (Fig.1.5). In the absence of a UV absorbing analyte, light passing through the flow cell generates a maximum signal at the photodiode which is then reduced when the UV absorbing analyte enters the detector and results in the change of detector current or voltage and therefore resulting signal/peak. This signal is electronically inverted by the software and results in a positive peak for the analyte. The detector response increases in with an increase in the concentration of the analyte in the flow cell.

Rapid advancement in light-emitting diode (LED) sources and photodetector technologies provide opportunities for compact, low power and inexpensive detectors for integration with microfluidic systems or on-capillary separation formats [109]. LEDs have gained significant attention over past few decades as light source for optical sensing and chemical analysis [109]. They have been increasingly used in miniaturised analytical systems for fluorescence and absorbance measurements since the first report by Flaschka *et al*. in 1973 [110]. For example, the commercially available 235 nm LED based photometric detector was integrated with capillary ion-exchange chromatography (IEC). The LED based photometric detector consisted of commercial Agilent interface placed within an in-build Al holder with LED light source fitted on each

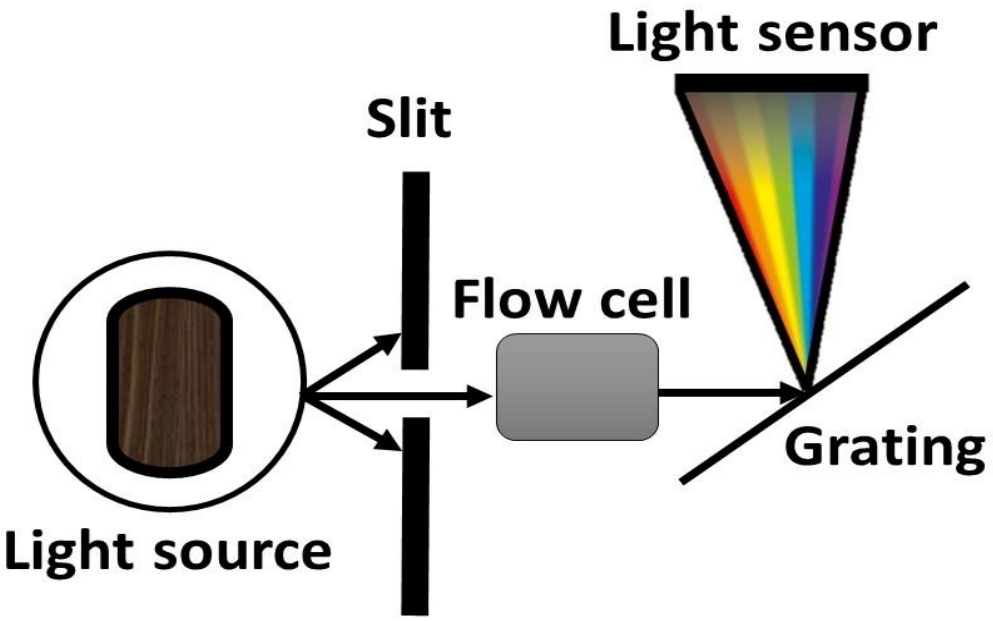

Fig.1.5: Schematic of a photometric detection assembly

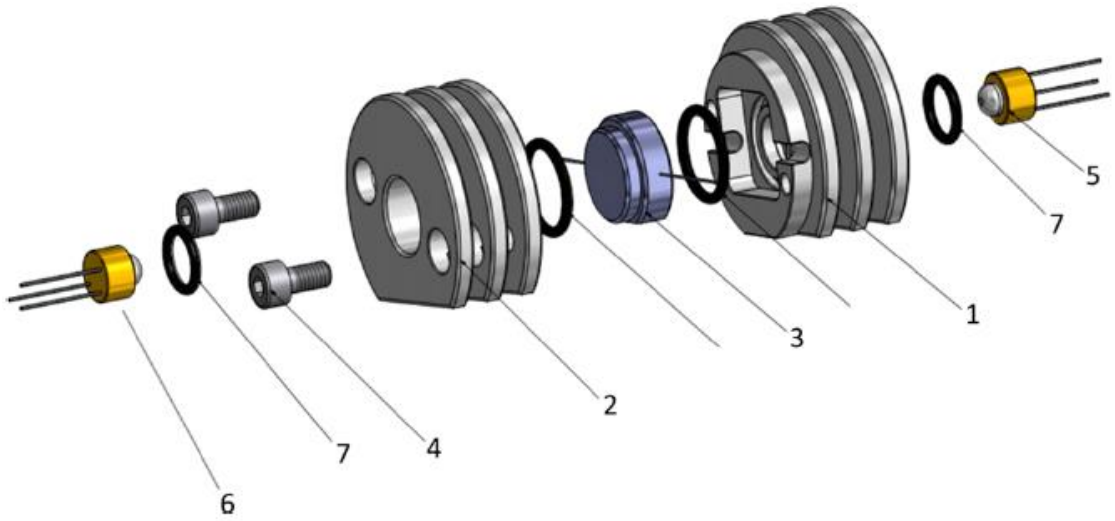

Fig.1.6. Schematic of the on-capillary photometric detector (1) Al housing for LED; (2) Al housing for photodiode; (3) Agilent interface (4) head cap screw; (5) LED (6) photodiode; and (7) O-ring for sealing (fig. taken from the reference). [109]

side of the holder (Fig.1.6). Their system demonstrated a great potential for LED based detectors for applications in low-cost miniaturised analytical devices [111]. Similarly, the use of deep-UV 255 nm LED as light sources for photometric detector for HPLC has also been reported [112]. Recently, a LED (260 nm) based photometric detector, with sensitivity at ppb level, was fabricated for on-column detection in capillary liquid chromatography [113].

Traditional methods for detector manufacturing are based on subtractive manufacturing techniques such as such as computer numerical control (CNC) routing [114]. However, using these machining techniques, the production of complex features such as hollow structures within a single object is difficult to achieve. However, the

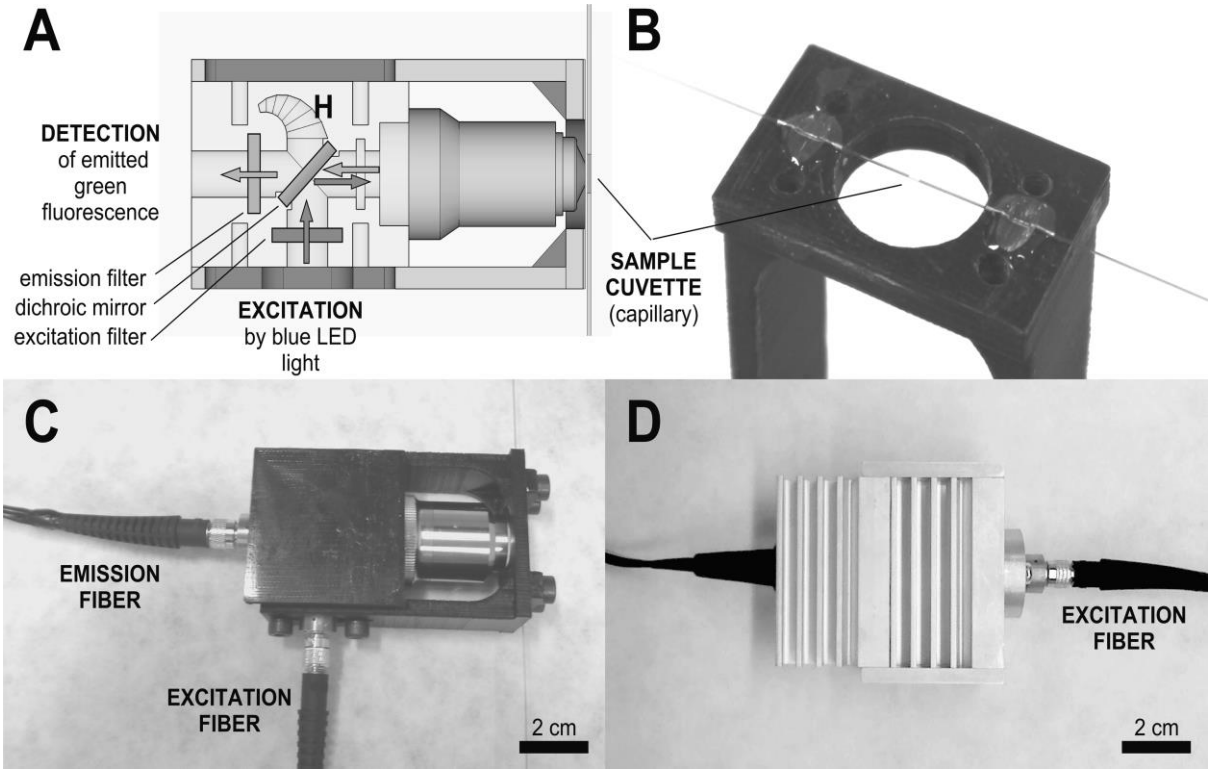

Fig.1.7. 3D printed fluorescence detection head scheme: the horn shaped hole H minimizes the excitation beam back reflection (A). Detail of the capillary guide: sample cuvette (B). The printed and assembled detection system including the capillary holder with mounted fused silica capillary(C). The LED source in an aluminium housing (D) (fig. taken from the reference). [113]

customisation and easy fabrication when using 3D printing has prompted many groups to tailor and optimise their own detection devices. For example, Prikryl and Foret used a low cost FDM 3D printer for fabricating a horn shape hollow structure within the fluorescence detection head, which could simply not be produced using standard machining methods. This detector was employed for fluorescent detection of oligosaccharides labelled by 8-aminopyrene-1,3,6-trisulfonate (APTS). The performance of developed 3D printed fluorescence detector was tested by comparing

it with semiconductor photodiode and photomultiplier as light sensing components [115]. By employing 3D printing parts, they were able to reduce cost, simplify customisation of spatial arrangement, and introduce miniaturisation as shown in Fig.1.7.

1.2.2. Flow cells

The integration of detection techniques with microscale separation systems such as CE and capillary LC usually requires various assembly parts and results in alignment and configuration issues. For example, for photometric detection, the alignment of the capillary/tubing with the detector components is a critical factor for optimal performance of an instrument, and may also limit user-friendliness. One way of circumventing this issue is integration of the channel with the detection assembly [116, 117]. Dias et al., 2014 designed a photometric flow cell consisting of a flow channel integrated with the detection components including a LED and photodiode on the opposite sides (Fig.1.8). This photometric flow cell was used for highly sensitive analysis of iron thiocyanate compound with minimum time (125 determination/hr) and reagent consumption [117]. The sensitivity achieved using these flow cells was improved due to long optical pathlength in comparison to traditional on-column/capillary UV-visible absorbance detectors in which the detection sensitivity is limited by short optical path length [118]. However, the flow cell required several assembly parts including: supporting blocks for LED and photodiode; glass cylinders to seal the channel ends and provide the transparent detection window inside the body for the light to travel from the light source through the sample to the detector; inlet and outlet tips, joined to the channel body by melting a small surface using a torch

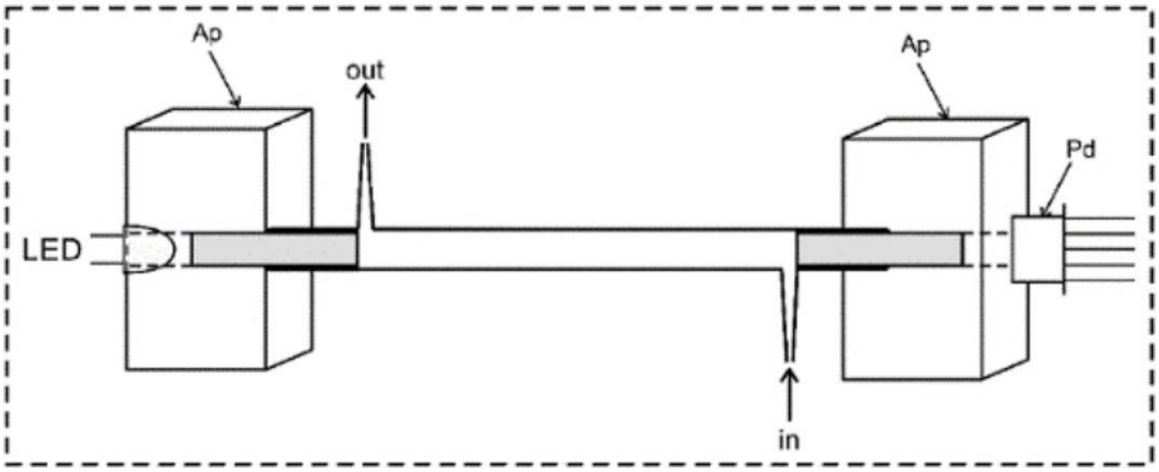

Fig.1.8: Photometric flow cell assembling detection components i.e. LED = light emitting diode and photodetector; and Ap = PVC blocks to support the flow cell body (fig. taken from the reference).[117]

[119]. The manufacturing and manual assembly of various parts of the flow cell is a labour intensive and time-consuming process and is prone to errors due to human intervention.

3D printing has been used for the fabrication of flow cells for chemiluminescence detector with features that were difficult to achieve using classical coiled tubing technique or by channel etching into polymeric materials. For example, Spilstead et al. fabricated a chemiluminescence detection flow cell using a Pro-Jet HD 3000 3-D moduler system [120]. 3D printing allowed the fabrication of the customised flow cell that was successfully used to distribute the post-column eluate into two different serpentine channel detection zone and therefore providing detection with two chemiluminescence systems for highly sensitive and reproducible detection (Fig.1.9). Similarly, Gupta *et al*. used Object Eden 260VS, (Stratasys, Australia) printer for the fabrication of a chemiluminescence flow cell that provided less tortuous flow and

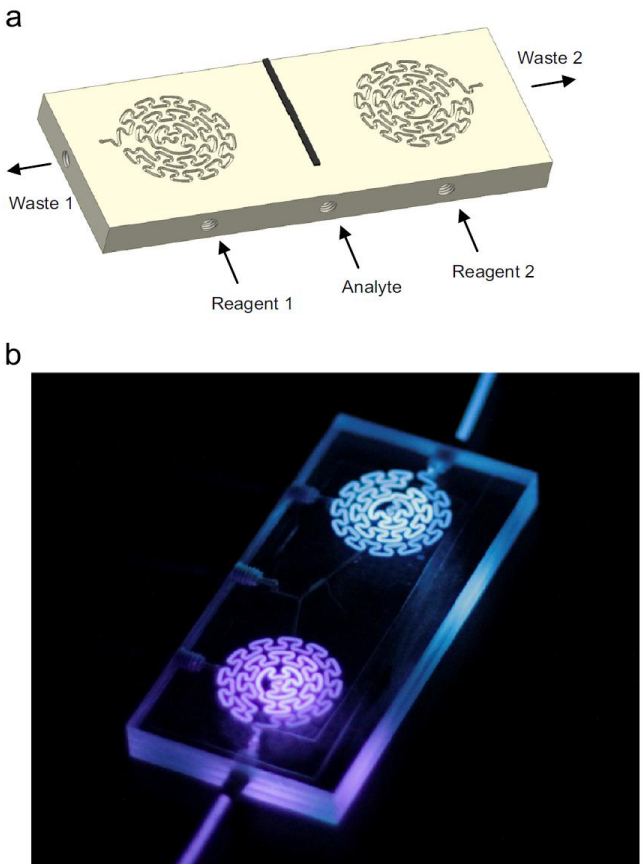

Fig.1.9. (a) The CAD design and (b) 3D printed image of the dual serpentine detection zone flow-cell (fig. taken from the reference) [119].

higher chemiluminescence signal (Fig.9)[121]. However, the cost of the printer and difficulty in removing the support material were the major limiting factors.

1.2.3. Pumps

Fluid pumping is a key feature of a microfluidic system and usually requires a micro pump to monitor and manipulate liquid flow at a smaller scale (≤ 1 mm). The fluid transport through micro pump is usually based on pressure, current, magnetic field, capillary action or electro osmosis [122-124]. Electro-osmotic pumps (EOPs) are one of the most commonly employed pumps with wide range of applications in high

performance liquid chromatography (HPLC) [125-127], chip based assays [128-130], microchannel cooling system [131], drug delivery [132, 133], device actuation [132], etc.

In an EOP, fluidic movement is driven by the electroosmotic flow which is caused by the electric double layer, consisting of a compact layer on the channel walls and a diffused layer in the liquid, formed due the electrostatic interaction between the channel surface and uncharged liquid (e.g. aqueous solution) [13] [134]. The EOPs have been commonly used in microfluidic systems due to their advantages such as; simple integration, compatibility with the micro technology [134] and capability to provide high pressure on chip devices [135, 136]. Furthermore they provide a pulse free stable flow rate which is essential for reliable operation of microfluidic devices and flow injection systems [137]. Other significant advantages of EOPs over the conventional pumping systems are that they exclude the need for moving parts, simplicity in controlling the flow magnitude and direction, and ability to achieve high flow rates [138, 139]. These advantages make EOP highly suitable for miniaturised and portable system where downscaling/downsizing of the instruments is a critical requirement. Heuck and Staufer fabricated a low voltage EOP (2V- 5V) with small foot prints (100 µm × 15 µm, L × W) for integration with microfluidic devices [140]. Similarly, Lazar and Karger developed a novel miniaturised pumping system consisting of shallow microchannels (1-100) to deliver liquid to larger diameter channels on to the microfluidic chip. A common inlet, outlet and reservoir was used for all pumping channels (Fig.1.10). The developed micropumping unit was used to pump samples to electrospray ionization (ESI) emitter for MS analysis [141]. The sufficiently small size of the pump and its ability to achieve satisfactory flowrate (0.05-1 µL min^{-1}) and

backpressure (up to 100 psi) makes it highly suitable for applications in common analytical microfluidic devices.

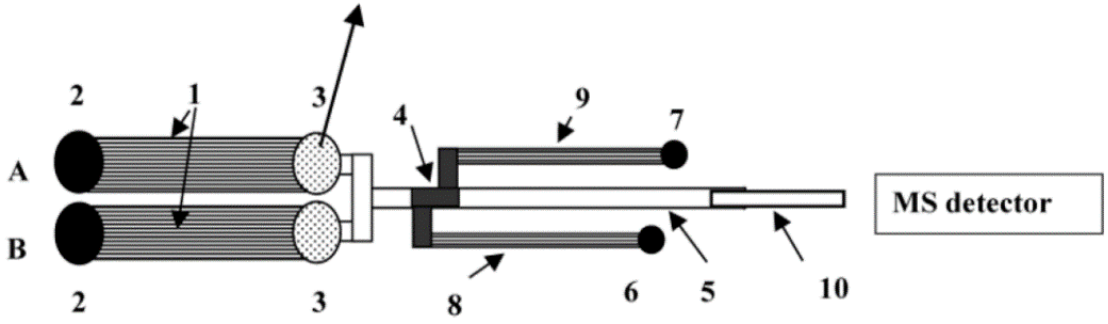

Fig.1.10: Schematic of EOP system 1) open channel EOP 2) EOP inlet reservoir 3) EOP outlet reservoir4) injection element 5) channel for separation/infution of sample 6) sample inlet reservoir 7) outlet reservoir for sample 8) sample inlet channels 9) and sample outlet channels 10) ESI emitter (fig. taken from the reference) [139].

A key requirement of all EOPs is that the electrodes generating electric current should be in direct contact with the ionic solutions, however, a significant challenge with this is that the voltage applied on the electrodes is automatically transferred to the rest of the fluidic system resulting in a fluidic system that is not electric field free [141]. Therefore, it is important to ground the liquid in the channels to prevent the leakage of current to the rest of the system. Ion-exchange membranes have long been used to ground the liquid at the electrically conductive joint that allows pumped liquid to be coupled with the microfluidic channels without leakage [142] Liu and Lu designed a stand-alone EOP consisting of an ion-exchange membrane that not only maintained the fluid flow but also grounded the liquid in the microfluidic conduit at the joint with

the help of an external electrode, therefore decoupling the electric field in the pump from the microfluidic channel [143]. The added advantage of this pump was that it was fabricated on a microchip which provides opportunities to integrate the pump with the microfluidic devices. A comparison of electro-osmotic pumps and their performance for microfluidic devices is provided in Table 1.1.

EOPs are usually fabricated with subtractive manufacturing techniques such micromachining [144] which is expensive, time consuming and provide limited options for design modification. In addition, external electrodes need to be incorporated into the device which are again produced by complicated, expensive and time consuming techniques such as CNC milling [145], electro discharge manufacturing(EDM) [146, 147].

There are few reports on the use of 3D printing for the fabrication of the pump [148-151]. For example, Lo et al. recently employed lithographic high resolution 3D printer for printing a micro Tesla pump integrated with the microfluidic device. The developed pump was used to transport the dyes into the microfluidic device without the need for external pumping system [148]. Wang et. al. in 2017 developed a 3D printed peristaltic microfluidics pumping system using FDM 3D printing technique. The pump was printed using a flexible thermoplastic polymer which provided flexibility and control of large mechanical actuation, similar to previously reported pneumatic PDMS systems, for mixing and active pumping. The flow rate of the microfluidic system, comprising of two micropumps and a micromixer, was tested at various pneumatic pressures and actuation frequencies. This system was applied for the detection of insulin concentration through a chemiluminescence immunoassay and the results were comparable with the previously reported PDMS microfluidics chips [152]

Table 1.1. A comparison of various electro-osmotic pumps and their performance for microfluidic devices

No.	Pumping electrolyte	Applied voltage	Flow rates	Pressure	Reference
1	DI water	40 V	0.01 µL/min	65 pa	[153]
2	10 mM phosphate buffer	1 kV	0.26 µL/min	-	[154]
3	10 mM carbonate buffer	400 V	0.0023 µL/min	-	[155]
3	25 mM phosphate buffer	3 kV	2 µL/min	-	[137]
5	DI water	1 kV	15 µL/min	33.4kpa	[156]
6	1/10 phosphate buffer	40 V	-	5 kpa	[157]
7	10 mM	1 kV	1.25 µL/min	-	[158]

1.3. Project Aims

The main goal of this project is to design and 3D print a simple FIA instrument. To achieve this customisation, the projects was fragmented down into 3D printing of various components of FIA instrument to evaluate their potential for automation and miniaturisation, which will be then integrated into an instrument later.

1. Multi-material FDM 3D printing and characterisation of customised phtometric flow cells with integrated slit and channel for applications in microfluidic.

2. 3D printing of highly customised electroosmotic pumps using low cost FDM 3D printer and evaluation of the pump performance for fluid manipulation in microfluidics.

1.4. Research outline, methods and techniques

The following section will describe the outline of the research framework, designing, fabrication and characterisation methods/techniques used in this project. This section provides a detailed overview of each experiment, and a link between different chapters in this thesis. The content here is presented in the same order as the chapters in this thesis.

1.4.1. Designing, 3D printing and characterisation of photometric detection assembly

In Chapter 2, a photometric detection assembly with integrated slit was designed and fabricated using cost-effect FDM 3D printer. The assembly was used to position a LED on one side of the capillary or tubing and a photodiode on the other side. The device design with V-shape feature facilitated in steady self-alignment of the capillaries and tubing, determined by consistent peak heights obtained for tubing repositioning between various FIA measurements. The size of the integrated slit is critical element of the device particularly for smaller diameter capillaries that require a smaller size slit to minimise the stray light, detected light that does not belong to the bandwidth of the given wavelength. The potential of an inexpensive low-resolution FDM 3D printer was investigated for its ability to fabricate the smallest slit size. This was achieved by exploring various printing orientations including; across

the slit, diagonal to the slit, and in parallel to the slit. The smallest slit size (70 µm) was printed for housing designed with a slit positioned in the XY plane parallel to the print direction. The characterisation of the 3D printed detection assembly consisting of 70 µm slit was acheived by using FIA to determine the linear range, effective path length and stray light for Orange G, the model analyte. The performance of the 3D printing detection body was compared with the commercial CE interface for separation of inorganic cations ($Zn^{2+}$and Cu^{2+}) complexes with PAR 4-(2-pyridylazo) resorcinol.

1.4.2. Designing, 3D printing and characterisation of photometric flow cell

Chapter 3 extends and improves the work described in Chapter two. To improve automation and miniaturisation, photometric flow cell with integrated channel and slit was designed and fabricated using multi-material 3D printer. The integration of channel and slit within a single device body provided advantages of minimum alignment and set-up requirement as compared to the previous device (Chapter 2) which required positioning of the capillaries/tubing for improved optical performance. The integrated slit also facilitated in improving the optical performance of the device due to minimum stray light. The other features of the device include; housing for LED and photodiode, transparent detection window, inlet and outlet ports. The device body including channels, inlet and outlet ports were printed using opaque material and transparent material was used for printing of the detection window. The flow-cell design was optimised by varying the slit dimension and optical path-length. The 3D printed flow cells with various slit sizes and optical pathlength were characterised by determining the % stray light and effective path length using Orange G as the test analyte.

1.4.3. Designing, 3D printing and characterization of electroosmotic pump

In Chapter 4, designing, fabrication and characterisation of electroosmotic pump (EOP) to provide fluid control is illustrated. The novel design of the device included a single channel divided into multiple channels which resulted in two regions with significantly different surface area therefore producing uni-directional flow of the fluid. The other novel feature of the pump is three integrated electrodes, two ground electrodes and one electrode for applying voltage. The ground electrodes facilitated in decoupling the conductive components from the rest of the device and therefore preventing current leakage. The non-conducting parts of the device such as a multiple channel (mesh) and a hollow channel were printed from non-conductive Acrylonitrile butadiene styrene (ABS), and the electrodes were printed from a commercially available conductive material. The design of the 3D printed device was validated by comparing the flow rate and fluid direction of the fully integrated pump with two pump halves. Therefore, two halves of the pump including two electrodes and the single pumping channel, and the mesh and two electrodes were 3D printed individually. Flow rate, pressure and current measurement of each half at various voltages was compared with the values obtained for the whole device with fully integrated components. The newly developed 3D printed pump was characterised by measuring current, pressure and flow rate at various voltages [86].

1.4.4. Repeatability and accuracy of the FDM printing method

Chapter 5 describes the various experiments that were performed to evaluate the efficiency of the FDM printing process in terms of repeatability and accuracy. The repeatability and accuracy of the devices developed in this project including photometric detection assembly,

photometric flow cell, and electro-osmotic pump was investigated by determining the consistency between the replicates of the printed objects and comparing the designed parts with the printed dimensions.

1.5. Reference

[1] K.V. Wong, A. Hernandez, A Review of additive manufacturing, Inetnational scholary Research Notes Mechanical Engineering (2012) 208760 (208710 pp.)-208760 (208710 pp.).

[2] T. Rayna, L. Striukova, From rapid prototyping to home fabrication: How 3D printing is changing business model innovation, Technological Forecasting and Social Change 102 (2016) 214-224.

[3] Z.-X. Low, Y.T. Chua, B.M. Ray, D. Mattia, I.S. Metcalfe, D.A. Patterson, Perspective on 3D printing of separation membranes and comparison to related unconventional fabrication techniques, Jornal of Membrane Science 523 (2017) 596-613.

[4] S.C. Ligon, R. Liska, J. Stampfl, M. Gurr, R. Mülhaupt, Polymers for 3D Printing and Customized Additive Manufacturing, Chemical Reviews 117 (2017) 10212-10290.

[5] R. Jiang, R. Kleer, F.T. Piller, Predicting the future of additive manufacturing: A delphi study on economic and societal implications of 3D printing for 2030, Technological Forecasting and Social Change 117 (2017) 84-97.

[6] J.P. Martins, M.P.A. Ferreira, N.Z. Ezazi, J.T. Hirvonen, H.A. Santos, G. Thrivikraman, C.M. França, A. Athirasala, A. Tahayeri, L.E. Bertassoni, Chapter 4 - 3D printing: prospects and challenges A2 - Uskoković, Vuk, in: D.P. Uskoković (Ed.) Nanotechnologies in Preventive and Regenerative Medicine, Elsevier, 2018, pp. 299-379.

[7] B.C. Gross, J.L. Erkal, S.Y. Lockwood, C. Chen, D.M. Spence, Evaluation of 3D printing and Its potential impact on biotechnology and the chemical sciences, Analytical Chemistry 86 (2014) 3240-3253.

[8] S. Waheed, J.M. Cabot, N.P. Macdonald, T. Lewis, R.M. Guijt, B. Paull, M.C. Breadmore, 3D printed microfluidic devices: enablers and barriers, Lab on a Chip 16 (2016) 1993-2013.

[9] S.W. Morton, K.P. Herlihy, K.E. Shopsowitz, Z.J. Deng, K.S. Chu, C.J. Bowerman, J.M. DeSimone, P.T. Hammond, Scalable manufacture of built-to-order nanomedicine: spray-assisted layer-by-layer functionalization of PRINT nanoparticles, Advance Materials 25 (2013) 4707-4713.

[10] J.R. Tumbleston, D. Shirvanyants, N. Ermoshkin, R. Janusziewicz, A.R. Johnson, D. Kelly, K. Chen, R. Pinschmidt, J.P. Rolland, A. Ermoshkin, E.T. Samulski, J.M. DeSimone, Continuous liquid interface production of 3D objects, Science 347 (2015) 1349-1352.

[11] I. Zein, D.W. Hutmacher, K.C. Tan, S.H. Teoh, Fused deposition modeling of novel scaffold architectures for tissue engineering applications, Biomaterials 23 (2002) 1169-1185.

[12] A.K. Au, W. Lee, A. Folch, Mail-order microfluidics: evaluation of stereolithography for the production of microfluidic devices, Lab on a Chip. 14 (2014) 1294-1301.

[13] M. Agarwala, D. Bourell, J. Beaman, H. Marcus, J. Barlow, Direct selective laser sintering of metals, Rapid Prototyping Journal 1 (1995) 26-36.

[14] S.F.S. Shirazi, S. Gharehkhani, M. Mehrali, H. Yarmand, H.S.C. Metselaar, N.A. Kadri, N.A. Abu Osman, A review on powder-based additive manufacturing for tissue engineering: selective laser sintering and inkjet 3D printing, Science and Technology of Advanced Materials 16 (2015).

[15] B. Gross, S.Y. Lockwood, D.M. Spence, Recent advances in analytical chemistry by 3D printing, Analytical Chemistry 89 (2017) 57-70.

[16] L.E. Diment, M.S. Thompson, J.H.M. Bergmann, Clinical efficacy and effectiveness of 3D printing: a systematic review, British Medical Journal 7 (2017).

[17] A.W. Feinberg, J.S. Miller, Progress in three-dimensional bioprinting, Material Research Society Bulletin 42 (2017) 557-562.

[18] D. Han, Z.C. Lu, S.A. Chester, H. Lee, Micro 3D Printing of a Temperature-Responsive Hydrogel Using Projection Micro-Stereolithography, Scientific Reports 8 (2018).

[19] K.Y. Hwa, B. Subramani, Synthesis of zinc oxide nanoparticles on graphene-carbon nanotube hybrid for glucose biosensor applications, Biosensors and Bioelectronics 62 (2014) 127-133.

[20] Y.X. Luo, Y.X. Li, X.L. Qin, Q.D. Wa, 3D printing of concentrated alginate/gelatin scaffolds with homogeneous nano apatite coating for bone tissue engineering, Materials & Design 146 (2018) 12-19.

[21] W. Zhu, H.T. Cui, B. Boualam, F. Masood, E. Flynn, R.D. Rao, Z.Y. Zhang, L.G. Zhang, 3D bioprinting mesenchymal stem cell-laden construct with core-shell nanospheres for cartilage tissue engineering, Nanotechnology 29 (2018).

[22] M. Kreiger, J.M. Pearce, Environmental life cycle analysis of distributed three-dimensional printing and conventional manufacturing of Polymer Products, Sustainable Chemistry & Engineering 1 (2013) 1511-1519.

[23] B. Satyanarayana, K.J. Prakash, Component replication using 3D printing technology, Procedia Materials Science 10 (2015) 263-269.

[24] T. Baden, A.M. Chagas, G. Gage, T. Marzullo, L.L. Prieto-Godino, T. Euler, Open Labware: 3-D Printing Your Own Lab Equipment, Public Libarary of Science Biology 13 (2015) e1002086.

[25] A.I. Shallan, P. Smejkal, M. Corban, R.M. Guijt, M.C. Breadmore, Cost-effective three-dimensional printing of visibly transparent microchips within minutes, Analytical Chemistry 86 (2014) 3124-3130.

[26] K.V. Wong, A. Hernandez, A Review of Additive Manufacturing, ISRN Mechanical Engineering 2012 (2012) 10.

[27] C.S. Tucker, D.B. Saint John, I. Behoora, A. Marcireau, Asme, Open Source 3D Scanning and Printing for Design Capture and Realization, 2014.

[28] D.W. Hutmacher, M. Sittinger, M.V. Risbud, Scaffold-based tissue engineering: rationale for computer-aided design and solid free-form fabrication systems, Trends in Biotechnology 22 (2004) 354-362.

[29] A.M. Tothill, M. Partridge, S.W. James, R.P. Tatam, Fabrication and optimisation of a fused filament 3D-printed microfluidic platform, Journal of Micromechanics and Microengineering 27 (2017).

[30] K.B. Anderson, S.Y. Lockwood, R.S. Martin, D.M. Spence, A 3D Printed Fluidic Device that Enables Integrated Features, Analytical Chemistry 85 (2013) 5622-5626.

[31] B. Berman, 3-D printing: The new industrial revolution, Business Horizons 55 (2012) 155-162.

[32] M. Bernhard, Additive manufacturing technologies – Rapid prototyping to direct digital manufacturing, Assembly Automation 32 (2012).

[33] K. Kadimisetty, J.Z. Song, A.M. Doto, Y. Hwang, J. Peng, M.G. Mauk, F.D. Bushman, R. Gross, J.N. Jarvis, C.C. Liu, Fully 3D printed integrated reactor array for point-of-care molecular diagnostics, Biosensors & Bioelectronics 109 (2018) 156-163.

[34] K. Li, H. Wei, W.G. Liu, H. Meng, P.X. Zhang, C.Y. Yan, 3D printed stretchable capacitive sensors for highly sensitive tactile and electrochemical sensing, Nanotechnology 29 (2018).

[35] Q.J. Luo, F. Yu, F. Yang, C. Yang, P. Qiu, X.L. Wang, A 3D-printed self-propelled, highly sensitive mini-motor for underwater pesticide detection, Talanta 183 (2018) 297-303.

[36] C.L.M. Palenzuela, F. Novotny, P. Krupicka, Z. Sofer, M. Pumera, 3D-Printed graphene/polylactic acid electrodes promise high sensitivity in electroanalysis, Analytical Chemistry 90 (2018) 5753-5757.

[37] C.K. Su, W.C. Chen, 3D-printed, TiO2 NP-incorporated minicolumn coupled with ICP-MS for speciation of inorganic arsenic and selenium in high-salt-content samples, Microchimica Acta 185 (2018).

[38] R. Walczak, K. Adamski, W. Kubicki, Inkjet 3D printed chip for capillary gel electrophoresis, Sensors and Actuators B-Chemical 261 (2018) 474-480.

[39] P.J. Kitson, M.H. Rosnes, V. Sans, V. Dragone, L. Cronin, Configurable 3D-Printed millifluidic and microfluidic 'lab on a chip' reactionware devices, Lab on a Chip 12 (2012) 3267-3271.

[40] M.D. Symes, P.J. Kitson, J. Yan, C.J. Richmond, G.J.T. Cooper, R.W. Bowman, T. Vilbrandt, L. Cronin, Integrated 3D-printed reactionware for chemical synthesis and analysis, Nature Chemistry 4 (2012) 349-354.

[41] M.N. Islam, B. Boswell, A. Pramanik, An investigation of dimensional accuracy of parts produced by three-dimensional printing, in: S.I. Ao, L. Gelman, D.W.L. Hukins, A. Hunter, A.M. Korsunsky (Eds.) World Congress on Engineering - Wce 2013, Vol I, 2013, pp. 522-525.

[42] H.P. Le, Progress and trends in ink-jet printing technology, Journal of Imaging Science and Technology 42 (1998) 49-62.

[43] A. Rida, L. Yang, R. Vyas, M.M. Tentzeris, Conductive inkjet-printed antennas on flexible low-cost paper-based substrates for RFID and WSN applications, Antennas and Propagation Magazine 51 (2009) 13-23.

[44] C.M. N., F.J. P., D. David, R. Clare, M.A. G., Use of stereolithography to manufacture critical-sized 3D biodegradable scaffolds for bone ingrowth, Journal of Biomedical Materials Research Part B: Applied Biomaterials 64B (2003) 65-69.

[45] S.H. Huang, P. Liu, A. Mokasdar, L. Hou, Additive manufacturing and its societal impact: a literature review, The International Journal of Advanced Manufacturing Technology 67 (2013) 1191-1203.

[46] S. Brian, Y. Yanzhe, M. Arunesh, S. Brent, N.K. Truong, A review of materials, fabrication methods, and strategies used to enhance bone regeneration in engineered bone tissues, Journal of Biomedical Materials Research Part B: Applied Biomaterials 85B (2008) 573-582.

[47] U. Steve, F. Richard, The rapid prototyping technologies, Assembly Automation 23 (2003) 318-330.

[48] X. Yan, P. Gu, A review of rapid prototyping technologies and systems, Computer-Aided Design 28 (1996) 307-318.

[49] F.P.W. Melchels, J. Feijen, D.W. Grijpma, A review on stereolithography and its applications in biomedical engineering, Biomaterials 31 (2010) 6121-6130.

[50] Y.-M. Huang, S. Kuriyama, C.-P. Jiang, Fundamental study and theoretical analysis in a constrained-surface stereolithography system, The International Journal of Advanced Manufacturing Technology 24 (2004) 361-369.

[51] X. Zheng, J. Deotte, M.P. Alonso, G.R. Farquar, T.H. Weisgraber, S. Gemberling, H. Lee, N. Fang, C.M. Spadaccini, Design and optimization of a light-emitting diode projection micro-stereolithography three-dimensional manufacturing system, Review of Scientific Instruments 83 (2012) 125001.

[52] Y. Pan, C. Zhou, Y. Chen, A Fast mask projection stereolithography process for fabricating digital models in minutes, Journal of Manufacturing Science and Engineering 134 (2012) 051011-051011-051019.

[53] T. Billiet, M. Vandenhaute, J. Schelfhout, S. Van Vlierberghe, P. Dubruel, A review of trends and limitations in hydrogel-rapid prototyping for tissue engineering, Biomaterials 33 (2012) 6020-6041.

[54] C. Sun, N. Fang, D.M. Wu, X. Zhang, Projection micro-stereolithography using digital micro-mirror dynamic mask, Sensors and Actuators A: Physical 121 (2005) 113-120.

[55] W. Ansgar, W. Björn, S. Katja, R.B. E., Maskless projection lithography for the fast and flexible generation of grayscale protein patterns, Small 8 (2012) 1570-1578.

[56] G. Comina, A. Suska, D. Filippini, PDMS lab-on-a-chip fabrication using 3D printed templates, Lab on a Chip 14 (2014) 424-430.

[57] H.N. Chan, Y. Chen, Y. Shu, Y. Chen, Q. Tian, H. Wu, Direct, one-step molding of 3D-printed structures for convenient fabrication of truly 3D PDMS microfluidic chips, Microfluidics and Nanofluidics 19 (2015) 9-18.

[58] G. Comina, A. Suska, D. Filippini, Low cost lab-on-a-chip prototyping with a consumer grade 3D printer, Lab on a Chip 14 (2014) 2978-2982.

[59] T. S., S. B., E. E., B. M., S. Th., S.M. J., W. T., Fabrication of biocompatible lab-on-chip devices for biomedical applications by means of a 3D-printing process, physica status solidi (a) 212 (2015) 1347-1352.

[60] X. Wang, X. Cai, Q. Guo, T. Zhang, B. Kobe, J. Yang, i3DP, a robust 3D printing approach enabling genetic post-printing surface modification, Chemical Communications 49 (2013) 10064-10066.

[61] S.M. Oskui, G. Diamante, C. Liao, W. Shi, J. Gan, D. Schlenk, W.H. Grover, Assessing and reducing the toxicity of 3D-printed parts, Environmental Science & Technology Letters 3 (2016) 1-6.

[62] T. Femmer, A.J.C. Kuehne, M. Wessling, Print your own membrane: direct rapid prototyping of polydimethylsiloxane, Lab on a Chip 14 (2014) 2610-2613.

[63] H. Gong, M. Beauchamp, S. Perry, A.T. Woolley, G.P. Nordin, Optical approach to resin formulation for 3D printed microfluidics, RSC Advances 5 (2015) 106621-106632.

[64] K.C. Bhargava, B. Thompson, N. Malmstadt, Discrete elements for 3D microfluidics, Proceedings of the National Academy of Sciences 111 (2014) 15013-15018.

[65] J.-W. Choi, H.-C. Kim, R. Wicker, Multi-material stereolithography, Journal of Materials Processing Technology 211 (2011) 318-328.

[66] S. Madhusudan, H.H. M., D. Parul, J.G. E., Inkjet printing—process and its applications, Advanced Materials 22 (2010) 673-685.

[67] d.G. B.-J., D.P. C., S.U. S., Inkjet Printing of Polymers: State of the Art and Future Developments, Advanced Materials 16 (2004) 203-213.

[68] W.N. A., D. Philip, Rapid product development in the USA, Europe and Japan, World Class Design to Manufacture 1 (1994) 27-36.

[69] D.T. Pham, R.S. Gault, A comparison of rapid prototyping technologies, International Journal of Machine Tools and Manufacture 38 (1998) 1257-1287.

[70] T. Kamesh, F. Georges, B. Amit, A. Nadim, Efficient slicing for layered manufacturing, Rapid Prototyping Journal 4 (1998) 151-167.

[71] M.P. Pulak, V.R. N., D.S. G., Slicing procedures in layered manufacturing: a review, Rapid Prototyping Journal 9 (2003) 274-288.

[72] D. Anand, D.T. M., W.J. J., N.R. J., Inkjet printing of bioadhesives, Journal of Biomedical Materials Research Part B: Applied Biomaterials 89B (2009) 28-35.

[73] N.P. Macdonald, F. Zhu, C.J. Hall, J. Reboud, P.S. Crosier, E.E. Patton, D. Wlodkowic, J.M. Cooper, Assessment of biocompatibility of 3D printed photopolymers using zebrafish embryo toxicity assays, Lab on a Chip 16 (2016) 291-297.

[74] J.L. Erkal, A. Selimovic, B.C. Gross, S.Y. Lockwood, E.L. Walton, S. McNamara, R.S. Martin, D.M. Spence, 3D printed microfluidic devices with integrated versatile and reusable electrodes, Lab on a Chip 14 (2014) 2023-2032.

[75] B.C. Gross, K.B. Anderson, J.E. Meisel, M.I. McNitt, D.M. Spence, Polymer coatings in 3D-Printed fluidic device channels for improved cellular adherence prior to electrical Lysis, Analytical Chemistry 87 (2015) 6335-6341.

[76] R.D. Sochol, E. Sweet, C.C. Glick, S. Venkatesh, A. Avetisyan, K.F. Ekman, A. Raulinaitis, A. Tsai, A. Wienkers, K. Korner, K. Hanson, A. Long, B.J. Hightower, G. Slatton, D.C. Burnett, T.L. Massey, K. Iwai, L.P. Lee, K.S.J. Pister, L. Lin, 3D printed microfluidic circuitry via multijet-based additive manufacturing, Lab on a Chip 16 (2016) 668-678.

[77] O.H. Paydar, C.N. Paredes, Y. Hwang, J. Paz, N.B. Shah, R.N. Candler, Characterization of 3D-printed microfluidic chip interconnects with integrated O-rings, Sensors and Actuators A: Physical 205 (2014) 199-203.

[78] S.A.N. Gowers, V.F. Curto, C.A. Seneci, C. Wang, S. Anastasova, P. Vadgama, G.-Z. Yang, M.G. Boutelle, 3D Printed Microfluidic Device with Integrated Biosensors for Online Analysis of Subcutaneous Human Microdialysate, Analytical Chemistry 87 (2015) 7763-7770.

[79] P. Andreas, L. Rüdiger, L. Andres, H. Ute, S. Rainer, M. Rolf, Biofunctional rapid prototyping for tissue-engineering applications: 3D bioplotting versus 3D printing, Journal of Polymer Science Part A: Polymer Chemistry 42 (2004) 624-638.

[80] F. Tim, F. Ina, W. Matthias, Additive manufacturing in fluid process engineering, Chemie Ingenieur Technik 88 (2016) 535-552.

[81] Y. Hwang, O.H. Paydar, R.N. Candler, 3D printed molds for non-planar PDMS microfluidic channels, Sensors and Actuators A: Physical 226 (2015) 137-142.

[82] J.M. Lee, M. Zhang, W.Y. Yeong, Characterization and evaluation of 3D printed microfluidic chip for cell processing, Microfluidics and Nanofluidics 20 (2016) 5.

[83] W. Rafał, A. Krzysztof, Inkjet 3D printing of microfluidic structures—on the selection of the printer towards printing your own microfluidic chips, Journal of Micromechanics and Microengineering 25 (2015) 085013.

[84] J.C. McDonald, M.L. Chabinyc, S.J. Metallo, J.R. Anderson, A.D. Stroock, G.M. Whitesides, Prototyping of microfluidic devices in poly(dimethylsiloxane) using solid-object printing, Analytical Chemistry 74 (2002) 1537-1545.

[85] Chee Kai Chua, Kah Fai Leong, C.S. Lim, Rapid prototyping principles and applications (with companion CD-ROM) World Scientific Publishing Co. Pte. Ltd., Singapore, 2010.

[86] A. Konta, M. García-Piña, D. Serrano, Personalised 3D Printed Medicines: Which Techniques and Polymers Are More Successful?, Bioengineering 4 (2017) 79.

[87] P.J. Kitson, M.D. Symes, V. Dragone, L. Cronin, Combining 3D printing and liquid handling to produce user-friendly reactionware for chemical synthesis and purification, Chemical Science 4 (2013) 3099-3103.

[88] Z. C.W., C. P.M., Computer aided decision support for fused deposition modeling, Rapid Prototyping Journal 7 (2001) 138-147.

[89] H.N. Chia, B.M. Wu, Recent advances in 3D printing of biomaterials, Journal of Biological Engineering 9 (2015) 4.

[90] R.A. L., H.K. E., J.A. E., B.W. R., S.R. N., A multi-material bioink method for 3D printing tunable, cell-compatible hydrogels, Advanced Materials 27 (2015) 1607-1614.

[91] B.R. Ringeisen, R.K. Pirlo, P.K. Wu, T. Boland, Y. Huang, W. Sun, Q. Hamid, D.B. Chrisey, Cell and organ printing turns 15: Diverse research to commercial transitions, Material Research Society Bulletin

38 (2013) 834-843.

[92] D. Lidia, G. Laura, L. Alfio, M. Giacomo, N. Alfio, R. Marco, Experimental validation of a simple, low-cost, T-junction droplet generator fabricated through 3D printing, Journal of Micromechanics and Microengineering 25 (2015) 035013.

[93] L. Krejcova, L. Nejdl, M.A.M. Rodrigo, M. Zurek, M. Matousek, D. Hynek, O. Zitka, P. Kopel, V. Adam, R. Kizek, 3D printed chip for electrochemical detection of influenza virus labeled with CdS quantum dots, Biosensors and Bioelectronics 54 (2014) 421-427.

[94] G.W. Bishop, J.E. Satterwhite, S. Bhakta, K. Kadimisetty, K.M. Gillette, E. Chen, J.F. Rusling, 3D-Printed fluidic devices for nanoparticle preparation and flow-injection amperometry using integrated prussian blue nanoparticle-modified electrodes, Analytical Chemistry 87 (2015) 5437-5443.

[95] K. Kadimisetty, I.M. Mosa, S. Malla, J.E. Satterwhite-Warden, T.M. Kuhns, R.C. Faria, N.H. Lee, J.F. Rusling, 3D-printed supercapacitor-powered electrochemiluminescent protein immunoarray, Biosensors and Bioelectronics 77 (2016) 188-193.

[96] J.L. Moore, A. McCuiston, I. Mittendorf, R. Ottway, R.D. Johnson, Behavior of capillary valves in centrifugal microfluidic devices prepared by three-dimensional printing, Microfluidics and Nanofluidics 10 (2011) 877-888.

[97] W. Zhong, F. Li, Z. Zhang, L. Song, Z. Li, Short fiber reinforced composites for fused deposition modeling, Materials Science and Engineering: A 301 (2001) 125-130.

[98] G. Wu, N. A. Langrana, R. Sadanji, S. Danforth, Solid freeform fabrication of metal components using fused deposition of metals, Materials & Design 23 (2002) 97-105.

[99] N. Macdonald, J. Cabot, P. Smejkal, R. Guijt, B. Paull, M. Breadmore, Comparing microfluidic performance of 3D printing platforms, Analytical Chemistry 89 (2017).

[100] W.W. M., Z. C., K. L., Improved surface quality in 3D printing by optimizing the printing direction, Computer Graphics Forum 35 (2016) 59-70.

[101] U. Kalsoom, P.N. Nesterenko, B. Paull, Recent developments in 3D printable composite materials, RSC Advances 6 (2016) 60355-60371.

[102] U. Kalsoom, A. Peristyy, P.N. Nesterenko, B. Paull, A 3D printable diamond polymer composite: a novel material for fabrication of low cost thermally conducting devices, RSC Advances 6 (2016) 38140-38147.

[103] F. Li, P. Smejkal, N.P. Macdonald, R.M. Guijt, M.C. Breadmore, One-step fabrication of a microfluidic device with an integrated membrane and embedded reagents by multi-material 3D printing, Analytical Chemistry 89 (2017) 4701-4707.

[104] R.S.K. Dr, Fundamentals of analytical instruments, McGraw Hill Professional, Access Engineering, 2006.

[105] W. Xu, R.C. Sandford, P.J. Worsfold, A. Carlton, G. Hanrahan, Flow injection techniques in aquatic environmental analysis: recent applications and technological advances, Critical Reviews in Analytical Chemistry 35 (2005) 237-246.

[106] J.F. Tyson, Flow injection analysis techniques for atomic-absorption spectrometry. A review, Analyst 110 (1985) 419-429.

[107] N. Anastos, N.W. Barnett, B.J. Hindson, C.E. Lenehan, S.W. Lewis, Comparison of soluble manganese(IV) and acidic potassium permanganate chemiluminescence detection using flow

injection and sequential injection analysis for the determination of ascorbic acid in Vitamin C tablets, Talanta 64 (2004) 130-134.

[108] http://community.asdlib.org/imageandvideoexchangeforum/2013/08/05/manifolds-for-flow-injection-analysis/, in, accessed on 22 May 2018.

[109] M. O'Toole, D. Diamond, Absorbance based light emitting diode optical sensors and sensing devices, Sensors 8 (2008) 2453.

[110] H. Flaschka, C. McKeithan, R. Barnes, Light emitting diodes and phototransistors in photometric modules, Analytical Letters 6 (1973) 585-594.

[111] Y. Li, P.N. Nesterenko, B. Paull, R. Stanley, M. Macka, Performance of a New 235 nm UV-LED-Based On-Capillary Photometric Detector, Analytical Chemistry 88 (2016) 12116-12121.

[112] S. Schmid, M. Macka, P.C. Hauser, UV-absorbance detector for HPLC based on a light-emitting diode, Analyst 133 (2008) 465-469.

[113] S. Sharma, H.D. Tolley, P.B. Farnsworth, M.L. Lee, LED-based uv absorption detector with low detection limits for capillary liquid chromatography, Analytical Chemistry 87 (2015) 1381-1386.

[114] F. Cecil, M. Zhang, R.M. Guijt, A. Henderson, P.N. Nesterenko, B. Paull, M.C. Breadmore, M. Macka, 3D printed LED based on-capillary detector housing with integrated slit, Anal. Chim. Acta 965 (2017) 131-136.

[115] J. Prikryl, F. Foret, Fluorescence detector for capillary separations fabricated by 3D printing, Analytical Chemistry 86 (2014) 11951-11956.

[116] D.S. Silva, B.F. Reis, Evaluation of the schlieren effect employing a LED-based photometer with a long-pathlength flow cell for reagentless photometric determination of ethanol in distilled ethanolic beverages, Microchemical Journal 129 (2016) 325-331.

[117] T.R. Dias, M.A.S. Brasil, M.A. Feres, B.F. Reis, A flow cell with a new design to improve the utilization of the radiation emitted by LED and employed as a radiation source for photometric detection, Sensors and Actuators B: Chemical 198 (2014) 448-454.

[118] K. Suhyeon, K. Weonseop, H.H. Jong, Extended path length post-column flow cell for UV-visible absorbance detection in capillary electrophoresis, Journal of Chromatography A 680 (1994) 109-116.

[119] T. R. Dias, M. Brasil, M. Feres, B. Reis, A flow cell with a new design to improve the utilization of the radiation emitted by LED and employed as a radiation source for photometric detection, Sensors and Actuators B: Chemical 198 (2014) 448-454.

[120] K.B. Spilstead, J.J. Learey, E.H. Doeven, G.J. Barbante, S. Mohr, N.W. Barnett, J.M. Terry, R.M. Hall, P.S. Francis, 3D-printed and CNC milled flow-cells for chemiluminescence detection, Talanta 126 (2014) 110-115.

[121] V. Gupta, P. Mahbub, P.N. Nesterenko, B. Paull, A new 3D printed radial flow-cell for chemiluminescence detection: Application in ion chromatographic determination of hydrogen peroxide in urine and coffee extracts, Analytica chimica acta 1005 (2018) 81-92.

[122] D.J. Laser, J.G. Santiago, A review of micropumps, Journal of Micromechanics and Microengineering 14 (2004) R35.

[123] N.-T. Nguyen, X.Y. Huang, T. Kok Chuan, MEMS-micropumps: A review, Journal of Fluids Engineering 124 (2002) 384-392.

[124] B.D. Iverson, S.V. Garimella, Recent advances in microscale pumping technologies: a review and evaluation, Microfluidics and Nanofluidics 5 (2008) 145-174.

[125] V. Pretorius, B.J. Hopkins, J.D. Schieke, Electro-osmosis - New concept for high speed liquid chromatography, Journal of Chromatography 99 (1974) 23-30.

[126] L.X. Chen, J.P. Ma, Y.F. Guan, An electroosmotic pump for packed capillary liquid chromatography, Microchemical Journal 75 (2003) 15-21.

[127] L.X. Chen, J.P. Ma, Y.F. Guan, Study of an electroosmotic pump for liquid delivery and its application in capillary column liquid chromatography, Journal of Chromatography A 1028 (2004) 219-226.

[128] J.P. Kutter, S.C. Jacobson, J.M. Ramsey, Integrated microchip device with electrokinetically controlled solvent mixing for isocratic and gradient elution in micellar electrokinetic chromatography, Analytical Chemistry 69 (1997) 5165-5171.

[129] P.C.H. Li, D.J. Harrison, Transport, manipulation, and reaction of biological cells on-chip using electrokinetic effects, Analytical Chemistry 69 (1997) 1564-1568.

[130] A.G. Hadd, D.E. Raymond, J.W. Halliwell, S.C. Jacobson, J.M. Ramsey, Microchip device for performing enzyme assays, Analytical Chemistry 69 (1997) 3407-3412.

[131] J. Linan, J. Mikkelsen, K. Jae-Mo, D. Huber, Y. Shuhuai, Z. Lian, Z. Peng, J.G. Maveety, R. Prasher, J.G. Santiago, T.W. Kenny, K.E. Goodson, Closed-loop electroosmotic microchannel cooling system for VLSI circuits, Transactions on Components and Packaging Technologies 25 (2002) 347-355.

[132] P.H. Paul, D.J. Rakestraw, Electrokinetic high pressure hydraulic system, in, ; SANDIA CORP, 2000, pp. Medium: ED.

[133] M.J. Pikal, The role of electroosmotic flow in transdermal iontophoresis, Advanced Drug Delivery Reviews 46 (2001) 281-305.

[134] X. Wang, C. Cheng, S. Wang, S. Liu, Electroosmotic pumps and their applications in microfluidic systems, Microfluidics and nanofluidics 6 (2009) 145.

[135] W. Wang, C.Y. Gu, K.B. Lynch, J.J. Lu, Z.Y. Zhang, Q.S. Pu, S.R. Liu, High-pressure open-channel on-chip electroosmotic pump for nanoflow high performance liquid chromatography, Analytical Chemistry 86 (2014) 1958-1964.

[136] I.M. Lazar, P. Trisiripisal, H.A. Sarvaiya, Microfluidic liquid chromatography system for proteomic applications and biomarker screening, Analytical Chemistry 78 (2006) 5513-5524.

[137] T.T. Razunguzwa, A.T. Timperman, Fabrication and characterization of a fritless microfabricated electroosmotic pump with reduced pH dependence, Analytical Chemistry 76 (2004) 1336-1341.

[138] Q. Lu, G.E. Collins, A fritless, EOF microchip pump for high pressure pumping of aqueous and organic solvents, Lab on a Chip 9 (2009) 954-960.

[139] C.Y. Gu, Z.J. Jia, Z.F. Zhu, C.Y. He, W. Wang, A. Morgan, J.J. Lu, S.R. Liu, Miniaturized electroosmotic pump capable of generating pressures of more than 1200 bar, Analytical Chemistry 84 (2012) 9609-9614.

[140] F.C.A. Heuck, U. Staufer, Low voltage electroosmotic pump for high density integration into microfabricated fluidic systems, Microfluidics and Nanofluidics 10 (2011) 1317-1332.

[141] I.M. Lazar, B.L. Karger, Multiple Open-Channel Electroosmotic Pumping System for Microfluidic Sample Handling, Analytical Chemistry 74 (2002) 6259-6268.

[142] P.K. Dasgupta, S. Liu, Electroosmosis: A reliable fluid propulsion system for flow injection Analysis, Analytical Chemistry 66 (1994) 1792-1798.

[143] S. Liu, Q. Pu, J.J. Lu, Electric field-decoupled electroosmotic pump for microfluidic devices, Journal of Chromatography A 1013 (2003) 57-64.

[144] V. Singhal, S.V. Garimella, A. Raman, Microscale pumping technologies for microchannel cooling systems, Applied Mechanics Reviews 57 (2004) 191-221.

[145] J. Kechagias, V. Iakovakis, M. Katsanos, S. Maropoulos, EDM electrode manufacture using rapid tooling: a review, Journal of Materials Science 43 (2008) 2522-2535.

[146] F.T. Weng, R.F. Shyu, C.S. Hsu, Fabrication of micro-electrodes by multi-EDM grinding process, Journal of Materials Processing Technology 140 (2003) 332-334.

[147] N.M. Elsiti, M.Y. Noordin, A.U. Alkali, Fabrication of high aspect ratio micro electrode by using EDM, in: Z. Hamedon (Ed.) 2nd International Manufacturing Engineering Conference and 3rd Asia-Pacific Conference on Manufacturing Systems, 2016.

[148] J.F. Lo, J. Hallgath, H. Mawari, Fluid transient characteristics of a 3D printed microfluidic tesla pump (Conference Presentation), in: SPIE BiOS, SPIE, 2018.

[149] Y.S. Lee, N. Bhattacharjee, A. Folch, 3D-printed quake-style microvalves and micropumps, Lab on a Chip 18 (2018) 1207-1214.

[150] M. Alam, F. Hossain, A. Vale, A. Kouzani, Design and fabrication of a 3D printed miniature pump for integrated microfluidic applications, International Journal of Precision Engineering and Manufacturing 18 (2017) 1287-1296.

[151] H. Gong, A.T. Woolley, G.P. Nordin, High density 3D printed microfluidic valves, pumps, and multiplexers, Lab on a Chip 16 (2016) 2450-2458.

[152] J. Wang, C. McMullen, P. Yao, N. Jiao, M. Kim, J.-W. Kim, L. Liu, S. Tung, 3D-printed peristaltic microfluidic systems fabricated from thermoplastic elastomer, Microfluidics and Nanofluidics 21 (2017) 105.

[153] K. Seibel, L. Schöler, H. Schäfer, M. Böhm, A programmable planar electroosmotic micropump for lab-on-a-chip applications, Journal of Micromechanics and Microengineering 18 (2007) 025008.

[154] S. Joo, T.D. Chung, H.C. Kim, A rapid field-free electroosmotic micropump incorporating charged microchannel surfaces, Sensors and Actuators B: Chemical 123 (2007) 1161-1168.

[155] J.M.E. IV, M.N. Hamblin, H.V. Fuentes, B.A. Peeni, M.L. Lee, A.T. Woolley, A.R. Hawkins, Thin film electro-osmotic pumps for biomicrofluidic applications, Biomicrofluidics 1 (2007) 014101.

[156] C. Chuan-Hua, J.G. Santiago, A planar electroosmotic micropump, Journal of Microelectromechanical Systems 11 (2002) 672-683.

[157] Y. Takamura, H. Onoda, H. Inokuchi, S. Adachi, A. Oki, Y. Horiike, Low-Voltage Electroosmosis Pump and Its Application to on-Chip Linear Stepping Pneumatic Pressure Source, in, Springer Netherlands, Dordrecht, 2001, pp. 230-232.

[158] O.T. Guenat, D. Ghiglione, W.E. Morf, N.F. de Rooij, Partial electroosmotic pumping in complex capillary systems: Part 2: Fabrication and application of a micro total analysis system (μTAS) suited for continuous volumetric nanotitrations, Sensors and Actuators B: Chemical 72 (2001) 273-282.

Chapter 2
3D printed LED based on-capillary detector housing with integrated slit

This chapter has been published in Analytica Chimica Acta. 2017, Volume 965, Pages 131-136 as a research article. Minor changes e.g. numbering font size, layout and style were introduced in order to match the formatting style of the thesis, keeping the original features of the article as much as possible.

2.1. Abstract

A 3D printed photometric detector body with integrated slit was fabricated to position a LED and photodiode either side of capillary tubing using a fused deposition modelling (FDM) printer. To make this approach suitable for capillaries down to 50 μm i.d. the dimension of the in-built slit is the critical element of the printed housing. The spatial orientation of the model for printing was found to significantly impact on the resolution of the structures and voids that can be printed. By designing a housing with a slit positioned in the XY plane in parallel with the print direction, the narrowest void (slit) that could be printed was 70 μm. The potential use of the 3D printed slit for photometric detection was characterised using tubing and capillary from 500 down to 50 μm i.d, demonstrating a linear response from 632- 40 mAU. The effective pathlength and stray light varied from 383- 22 μm and 77- 50 % for 500- 50 μm i.d tubing and capillary. The use of a V-shaped alignment feature allowed for easy and reliable positioning of the tubing inside the detector, as demonstrated by a RSD of 1.9% (n=10) in peak height when repositioning the tubing between measurements using flow injection analysis (FIA). The performance of the 3D printed housing and 70 μm slit was benchmarked against a commercially available interface using the CE separation of Zn^{2+} and Cu^{2+} complexes with PAR. The limit of detection with the 3D printed slit was 6.8 and 4.5 μM and is 2.8 and 1.6 μM with the commercial interface.

2.2. Introduction:

Liquid chromatography (LC), capillary electrophoresis (CE), and flow injection analysis (FIA), are fundamental analytical techniques applicable to a wide variety of samples, primarily to non-volatile analytes [1-5]. Optical detection techniques (absorption photometric, fluorescence or chemiluminescence) are often used to record the separation (in CE, LC) or colour-forming reaction (in FIA) [6, 7]. In CE and FIA, photometric detection is often performed on-capillary (on-column) [8] employing a detector body to align optical components with the tubing or capillary.

Traditionally, the detector body is fabricated using subtractive manufacturing techniques, such as Computer Numerical Control (CNC) routing, removing material until the desired shape is achieved [9]. However, it is difficult to make hollow elements inside a single object as the tool needs to be able to reach the material to be removed. For example, the horn-shape detector made by Přikryl and Foret [10] designed to refocus and direct the excitation light away from the detector to reduce the scattered light entering the detector, would be very expensive to make from a single piece of material on smaller scale. This design can be made using additive manufacturing, also known as 3D printing. 3D printing has emerged as a simple low-cost alternative to machining [11] and is capable of creating complex 3D structures including those containing hollow elements and eliminates the need for assembly. A computer aided design (CAD) drawing is digitally sliced into layers and saved as an STL (stereolithography) file, which is sent to the printer where the part is created in a layer-by-layer manner within a few hours. 3D printing allows for the adoption of a “fail fast, fail often” approach highly suited for optimising complex designs. There are a number of 3D printing approaches, with STL, inkjet and fused deposition modelling (FDM) are frequently used for laboratory-based sciences [12]. While not renowned for its resolution, FDM is attractive because of its low cost, and the capability to print a wide

range of materials including those used in traditional manufacturing [13], and because structures can be printed without a support.

Here we report the use of a FDM printer for the fabrication of an on-capillary photometric detector assembly. Key to the optical performance of the photometric detector is construction of a sufficiently narrow slit to reduce scattering and stray light, and the printing process was optimised to yield a 70 µm wide slit using a consumer-grade FDM printer. Using a 470 nm LED as light source, the printed detector housing containing the slit was characterised by FIA with Orange G as a probe. Its performance was found to be comparable with a commercially available CE detection interface when employed for the CE separation of metal complexes with PAR [14].

2.3. Materials and method

2.3.1. Chemicals

Orange G (1-phenylazo-2-naphthol-6,8-disulfonic acid disodium salt) of Standard Fluka quality was obtained from Fluka (Buchs, Switzerland). TAPS (N-tris[Hydroxymethyl]methyl-3-aminopropane-sulphonic acid), PAR 4-(2-pyridylazo) resorcinol, monosodium salt hydrate and Zinc Chloride were obtained from Sigma Aldrich (Sydney, Australia). Copper (II) Nitrate was obtained from AJAX Chemicals (Sydney, Australia).

Water was purified from deionized water using a Milli-Q water purification system (Millipore, Bedford, MA, USA).

2.3.2. CAD design

The computer aided design (CAD) of the 3D printed housing and slit was created using Inventor Pro (Autodesk, San Rafael, USA) with the final STL available in the supplementary information. The CAD of an Agilent interface holder was created using AutoCAD (Autodesk, San Rafael, USA) and the STL file is also available in the supplementary information.

2.3.3. Fabrication

A FDM printer (Felix 3.0, Felix robotics, the Netherlands) used in combination with black PLA (Matter Hackers, CA, USA) was used to print the detector parts from the STL files using the printer's proprietary software. The extruder temperature was 210 °C, the print bed was 80 °C and the extruded filament size ranged from 100 to 250 µm depending on the settings.

2.3.4. Instrumentation for FIA

The flow injection system comprised two programmable syringe pumps (SPS01, each 100 µL), two automated selector valves (AV201), and electronic interface board (EIB), valve manifold (4vm) and breadboard (upb-08) from Lab Smith (Livermore, CA, USA).

The injection valve was a low pressure Cheminert 6 port 2 position valve (C22-3186EH-FL, VICI, Houston, TX, USA). The µProcess software was used for control of all components from Lab Smith (Livermore, CA, USA). An Ecorder (eDAQ Pty Ltd, NSW, Australia) was used for data collection, display and analysis of the detector signals. A blue LED (470 nm) was used as light source (Mfr. Part No.L-7113VBC-D, 5 mm, 30 mA maximum steady current, Kingbright, CA, USA) and the transmitted light was detected using a silicon photodiode (Part number: IPL 10530 DAL,IPL, Dorset, UK).

2.3.5. CE Instrumentation

A Hewlett Packard 3D CE (Waldbron, Germany) instrument equipped with a diode array UV absorbance detector and Agilent Chemstation software Rev. A. 08.03 (847) was used for analysis. The cassette was set at 25 °C. Untreated fused silica capillaries (Polymicro, Phoenix, AZ, USA) with an internal diameter of 75 µm and outer diameter of 360 µm were used for separation unless otherwise stated. The length of capillary was kept at 70 cm (effective length of 49.5 cm to the 3D printed slit/3D printed Agilent interface holder) and the separation voltage was +25 kV.

New capillaries were conditioned sequentially with 0.1 M NaOH, water and BGE for 15 min each at approximately 900 mbar using the flush setting. The same procedure was repeated at the start of the day. At the end of each day, the capillary was flushed with 0.1 M NaOH and water at 960 mbar for 2 min and stored in water. The capillary was flushed with BGE for 2 min prior to each injection.

2.3.6. FIA procedure and detector performance characterisation

FEP (Fluorinated ethylene propylene) tubing with an i.d. of 200 µm and 500 µm and o.d. 1000 µm and 1500 µm, respectively, (IDEX, WA, USA) and untreated fused silica capillaries (Polymicro, Phoenix, AZ, USA) , i.d. 100, 75 and 50 µm and o.d. 360 µm, were flushed with water before use. A series of standards was prepared by serial dilution of stock solution of Orange G [15-17]. The LED was positioned in the FDM printed detection assembly and the light passed through the slit and the detection tubing onto the photodiode. The absorbance was calculated by the data acquisition system from the signal as its logarithmic function. Absorbance measurements at 470 nm were performed by flushing the detection tubing with concentrations of Orange G from 0.03 to 20 mM. A graph of sensitivity (absorbance/Orange

G concentration) *vs*. absorbance was plotted to determine effective path length and % of stray light [15, 16, 18].

2.4. Result and discussion

2.4.1. Detector design and general considerations

For optimal photometric detector performance (high linear range, low stray light and high signal to noise ratio), alignment of the capillary/tubing with the light source, slit, and silicon diode detector are critical [19]. Positioning of capillary respective to slit is a well-discussed issue and it must be given close attention when a detector is introduced/designed. To accomplish the self-aligning of the on-capillary detection tubing, a V-shape design was implemented using this well-established approach.

The detector body serves to accurately position capillaries and tubing with o.d. ranging from 375 µm to 10 mm and to align the capillary/tubing with the LED, slit and detector. The design elements of the detection body for capillary/tubing and optical alignment are indicated in Fig.2.1.1 To align the capillary with the optical elements, an open-ended insertion slot ending in a V-shape was introduced, together with a lever to keep the capillary/tubing down in the V. This open design allows positioning of the tubing by sliding it into place from the side, eliminating the need to remove any fittings as required for designs where the tubing is threaded through a narrow hole. As illustrated in Fig.2.1A and B, the relatively wide opening at the side allows for the use of tubing with an o.d. up to 10 mm.

To accurately and easily position the light source, in our case a LED, and photodiode for photometric detection, the detection body design includes a cavity on either side of the slit to accommodate the LED and photodiode, respectively. Based on dimensions, the slit is the most critical element of the detection

body. It defines the light beam passing through the capillary/tubing to the photodetector and should have a width that is about the same as the capillary/tubing i.d. It also should be positioned in parallel with the tubing [20]. Slit dimensions of 50 μm x 1000 μm (width x length) are typically used for CE while 100-200 μm x 2-5 mm slits are typically used for larger i.d. tubing as used in capillary LC. Being positioned between the light source and photodetector, the slit is located in the core of the detection housing. This makes the machining of such a high precision feature in a single piece detection body difficult using traditional manufacturing techniques, hence detection bodies are typically assembled from two or more pieces. For ease of use and to prevent manual alignment, a monolithic detection body would be preferred. In this work, a consumer-grade FDM printer was used to create a monolithic detection body including a slit, as shown in Fig.2.1B.

2.4.2. 3D Printing and Characterisation

The FDM printer selected for use has spatial Z resolution defined by the manufacturer of 50 μm and allows variation of the thickness of the extrudate between 50 μm and 250 μm, providing a means for adjusting the resolution, theoretically in both XY and Z dimensions. With the ambition to make a detector housing for CE, typically using capillaries of 50-75 μm i.d., slits with an equivalent width were required. Given that the spatial definition for most FDM printers, determined by layer thickness and layer orientation, is currently around 50 μm, creating a feature of these dimensions is challenging and required optimisation.

After optimisation of the printing parameters (extruder temperature 210^0 C and print bed temperature 80°C) the first parameter that was examined was the printing orientation. Three different orientations of the body were explored, with Fig.2.2A showing the printed slits with widths ranging from 250-50 μm with a length of 1000 μm printed with three different orientations organised according to the way in

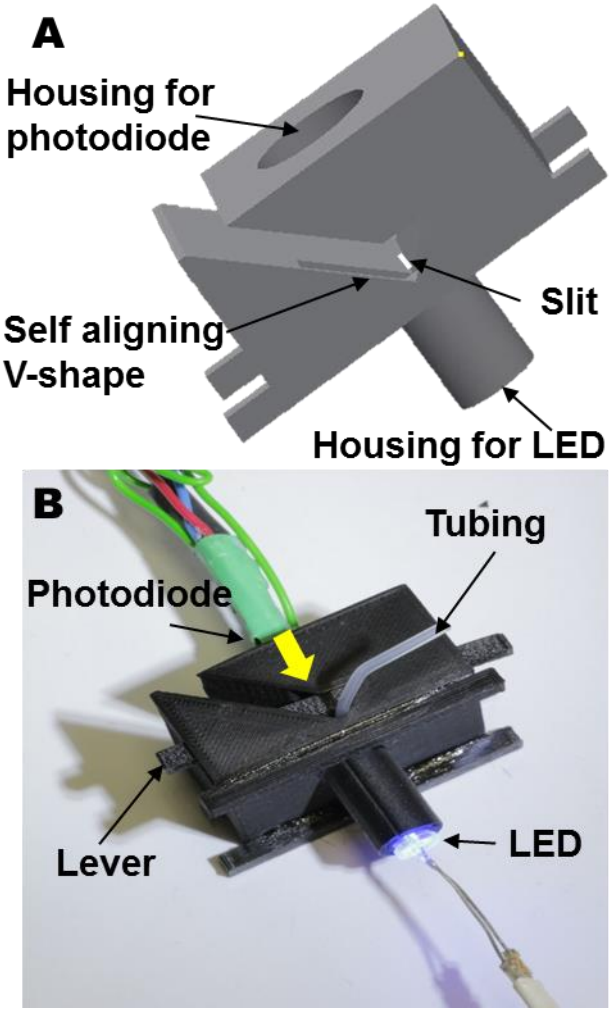

Fig.2.1. A) CAD design of the detector and illustration of its different parts B) 3D printed on capillary photometric detector. The yellow arrow shows the plastic housing pushing the capillary into the self-aligning V shape.

which the printer prints each layer. Fig.2.2A shows the 3D printed slits with various widths when the slit is printed across multiple layers. As can be seen, the printer was able to print the slits with a large dimension (250 and 200 µm), but not down to the 50-75 µm required for CE. The poor shape of the slit was due to compression of layers onto each other and turns in the extrudate where the slit area was

defined. Fig.2.2B shows slits fabricated by printing the slit within a single layer by orientating the slit so that it is printed directly on the bed. However, no slits were printed in this orientation presumably due to the printer outlining the slit prior to beginning to print the rest of the layer. Fig.2.2C shows the slit printed in multiple layers, but in a way that the length of the slit was in parallel with the print direction. This way, compression and bends at the edges could be minimised. As depicted in Fig.2.2C, the minimum slit width that could be printed in this orientation was 70 µm, within the 50-75 µm required for CE. This printing orientation was selected for the remainder of this work.

2.4.3. Optical performance of the 3D printed housing and slit

The performance of the 3D printed detector body with 70 µm slit was characterised by FIA experiments with Orange G to determine the linear range, effective pathlength and stray light. The linear range was defined as the absorbance from the limit of detection (LOD) up to the absorbance where the sensitivity had decreased by 5 % relative to the extrapolated linear trend constructed from lower concentrations.

The absorbance of Orange G at concentrations ranging from 0.03 to 20 mM was measured and the collected data are plotted for different width slits in Fig.2.3A. Stray light and effective path length can be derived from the sensitivity plot by extrapolating the curves as shown by the arrows in Fig.2.3B [15-17].

Absorption and concentration are linked through the Beer-Lambert law, $A=\varepsilon \ell c$ where A is absorbance, ~~ε~~ ε = molar absorption coefficient for orange G. (18546 $L.mol^{-1}cm^{-1}$); c= concentration of the sample in mM and length ℓ = m.

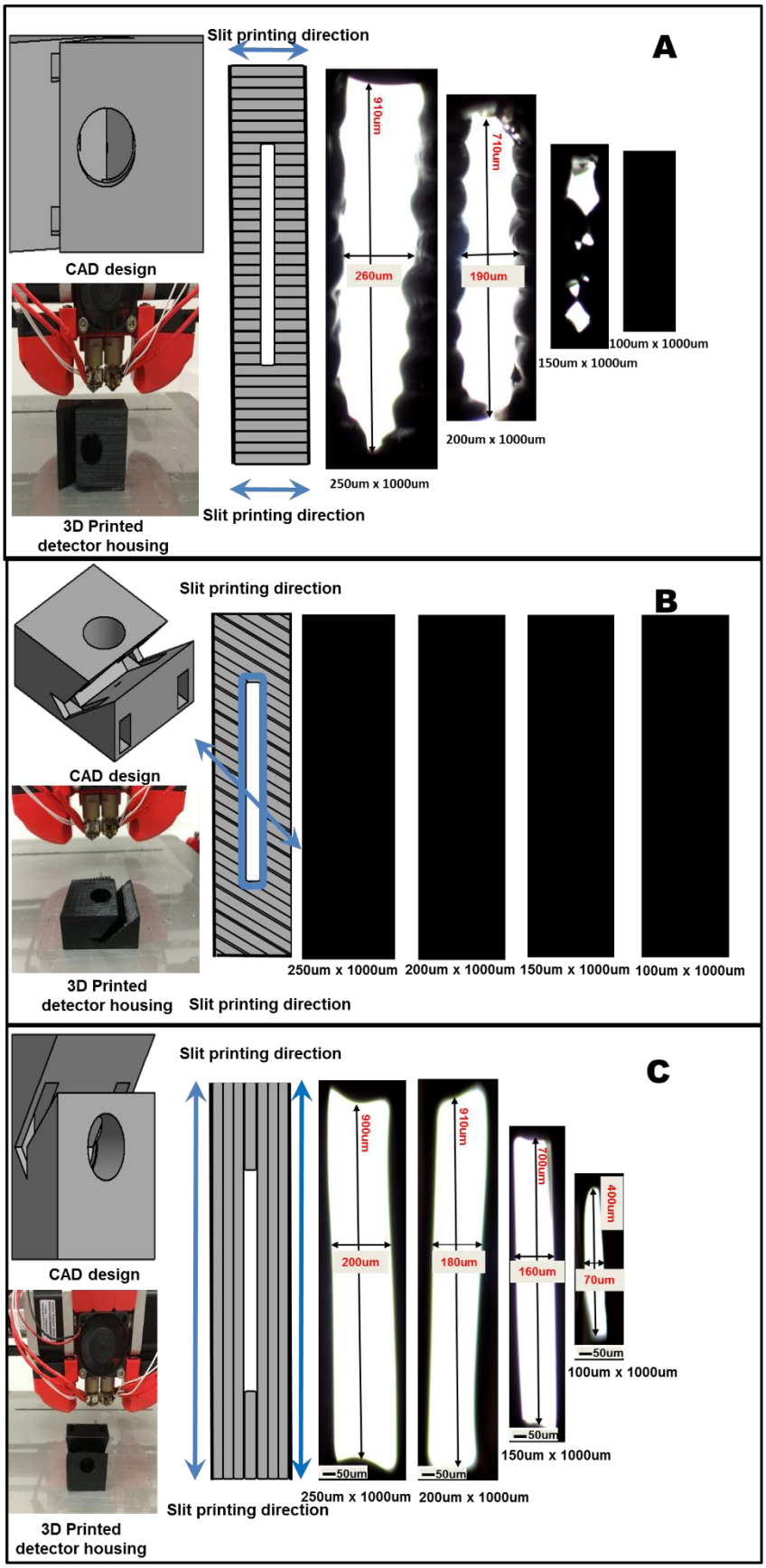

Fig.2.2 Evaluation of various printing/layering orientation for the fabrication of slits.

Across the linear response range of the detector, the value of A/c is constant for the absorbance measurements. When out of the linear response range, the value of A/c

will change, making a plot of A/c vs A useful in deriving information about the upper linear range of the detector response. Here, the upper end of the linear range (mAU), corresponding to a 5% decrease in A/c, was determined as 632, 584, 54, 45 and 40 mAU for the 500 µm and 200 µm i.d. tubing and 100 µm, 75 µm and 50 µm i.d. capillary, respectively.

Through the Beer-Lambert law, the plot of A/c vs A can also be used to determine the effective pathlength, extrapolating the graph to zero absorbance and dividing this A/c by ε. For the 500 µm and 200 µm i.d. tubing and 100 µm, 75 µm and 50 µm i.d. capillary, the extrapolated sensitivity (A/c) were 748, 300, 118, 89 and 860 AU.L/mol., respectively.

The effective pathlength is defined as the 'average' path length the light travels through the solution. The stray light was calculated as the percentage relative to the incident light. The last two parameters have been shown to often correlate, with a relatively large effective path length typically associated with a lower % of stray light [15-18, 21, 22].Using a value of 19511 $L.mol^{-1}cm^{-1}$ for the molar absorptivity of Orange G [16], the effective pathlength was determined to be 383 µm and 153 µm for the 500 µm and 200 µm i.d. tubing and 61 µm, 45 µm and 22 µm for the 100 µm, 75 µm and 50 µm i.d. capillary, respectively. This corresponds to 77 and 76 % of the tubing i.d. and 61, 60 and 50 % of the i.d. capillary, respectively. These values are comparable to some commercial CE instruments, [18, 21, 23] which indicates the satisfactory performance of the detector with the 3D printed slit.

Finally, the percentage of stray light is also estimated from the A/c vs A plot from the last point at the highest concentration in each graph in Fig.2.3B. The % stray light was calculated to be 3.80 % and 13 % for the 500 µm and 200 µm i.d. tubing and 18 %, 23 % and 44 % for the 100 µm, 75 µm and 50 µm i.d.

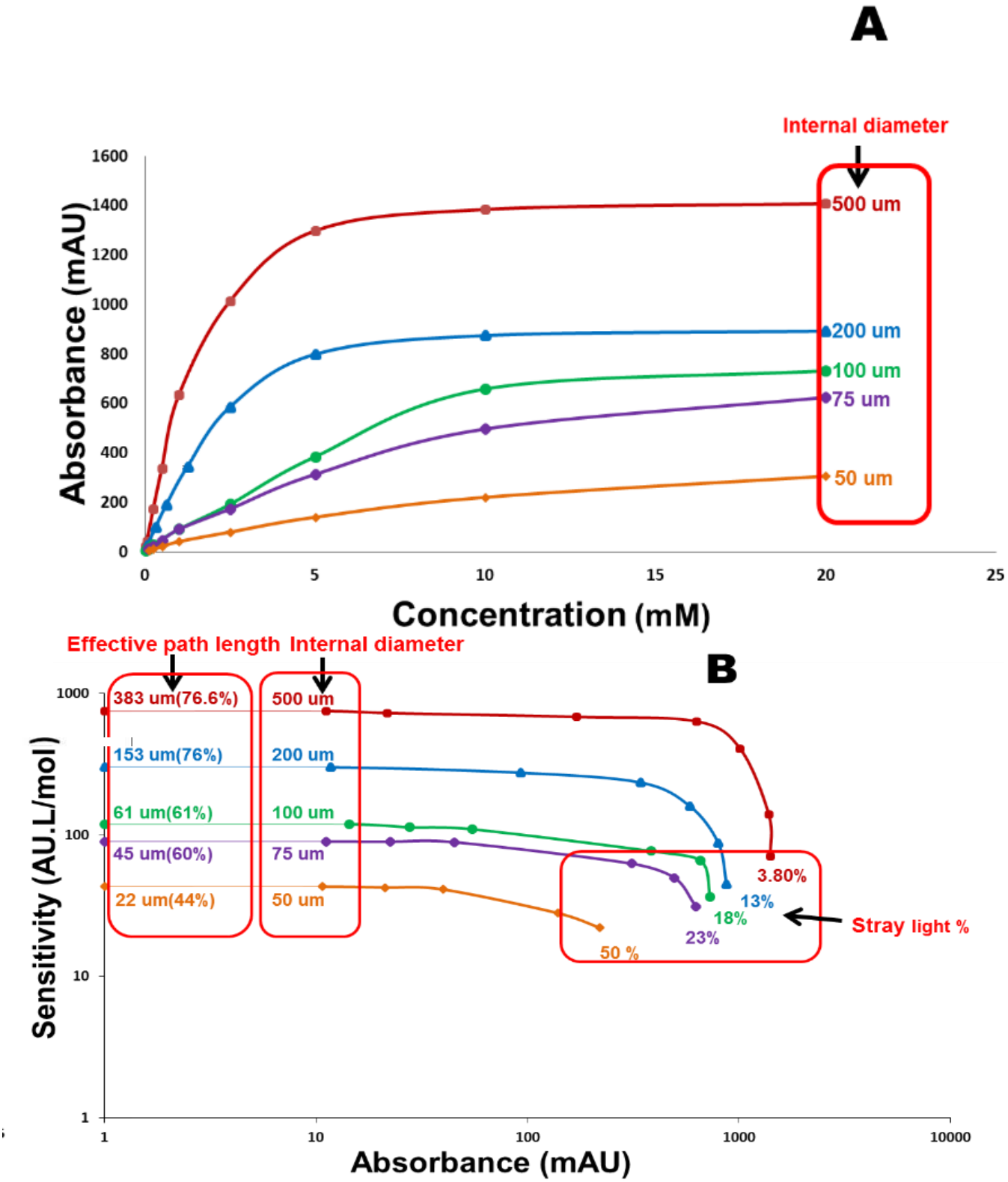

Fig.2.3. A) Graph of absorbance (mAU) vs concentration (mM), B) Graph of sensitivity (AU.L/mol) vs absorbance. (mAU).

500 µm and 200 µm i.d. tubing and, 100 µm, 75 µm and 50 µm i.d. capillary used for experiment.

tubing and capillary, respectively. As expected, stray light decreased with increasing tubing i.d., as the ratio of the effective pathlength over slit width increased. To make the detector assembly more suitable for capillary with i.d. <50 µm, a slit width <50 µm would be desirable, but was not possible to achieve with the current printer and settings.

To determine the repeatability of the self-alignment feature of the detector assembly, absorbance values were recorded after the 75 µm i.d. capillary had been removed and re-positioned in the assembly, and 0.125 mM of Orange G injected. Fig.2.1.2 shows the overlay of absorbance traces for 10 replicate measurements, with an RSD of 1.9 % for the absorbance at the peak maximum.

The final numerical parameter determined to characterise the detector performance was the baseline noise. The stability of the position of the tubing in the V-shape affects the vibration of capillary, with enhanced stability reducing baseline noise thus helping in achieving a baseline noise of 0.060 mAU peak to peak (unfiltered data). The signal for the peak corresponding to 0.125 mM Orange G peak in FIA mode was 13.5 mAU, which corresponds to a LOD of 2.1 µM (S/N=3), which is a value comparable to literature values for similar dyes [24].

2.4.4. Performance of the 3D printed housing and slit in comparison to commercial capillary interface

On-capillary absorbance detection is the most common detection method for CE [8, 25].

To benchmark the performance of the 3D printed detector body against the commercially available Agilent interface, CE separations of Zn^{2+} and Cu^{2+} as PAR complexes [14] were carried out using both the 3D printed detector body and the Agilent interface housed in a 3D printed holder to provide the same effective length for both types of slits. As can be seen in Fig.2.4A the

peak heights compared well between the 3D printed slit and Agilent interface, with a slight difference due to slight variation in the EOF. The LOD, noise (N), and S/N ratio for Cu^{2+} and Zn^{2+} are provided in table 2.1. The data show that the detector provides detection limits 2-3 times higher than the commercial interface.

The 3D printed detector body was used for the analysis of metals in river water collected from the west coast of Tasmania [26]. The river water samples were filtered prior to injection, and spiking confirmed peaks with migration times around 4 min and 5 min to be Cu^{2+} and Zn^{2+} (Fig.2.4.B). This application demonstrates FDM printing can be used for the fabrication a monolithic detector body containing high precision elements. The affordability and flexibility in design offered by 3D printing makes this approach attractive for developing custom-designed instrumentation, for example portable CE systems. Furthermore, the developed detector also has the potential to replace detectors

using traditional light sources in the UV regions thanks to the increasing commercial availability of LEDs in the UV region (currently down to 235 nm).[27]

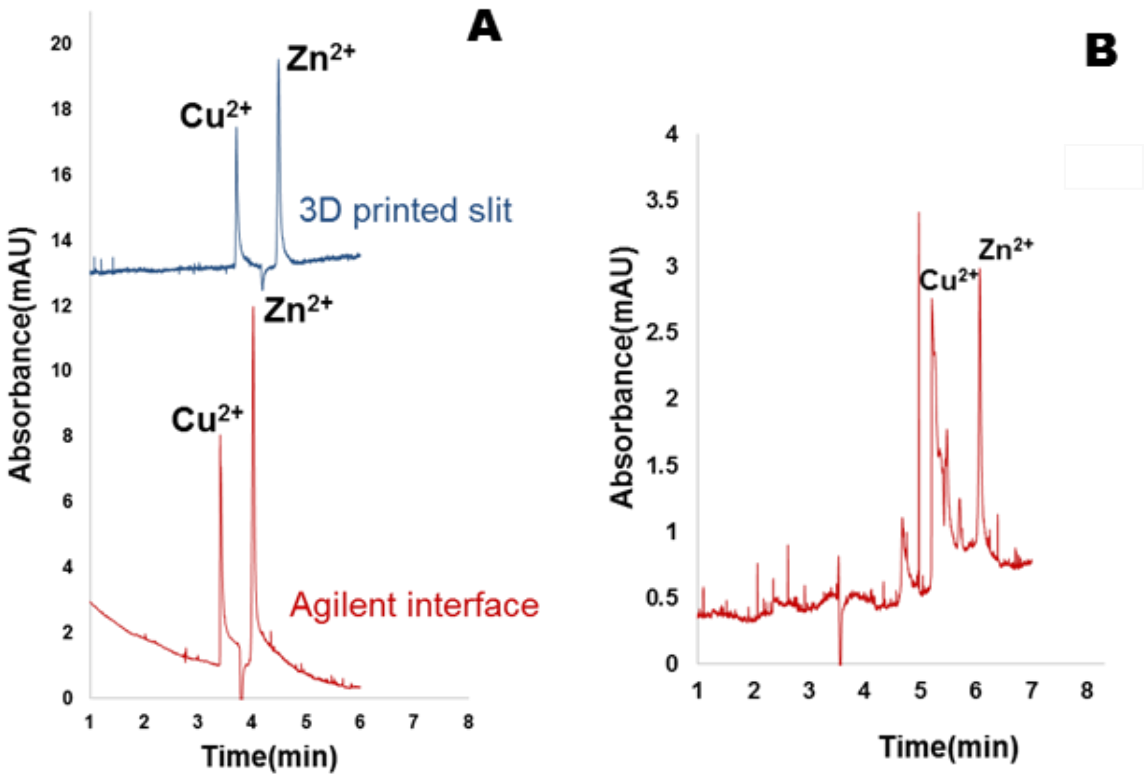

Fig.2.4.A).Electropherograms for separation of Cu2+(0.1mM) and Zn2+(0.1mM) cations in standard solution. Experimental conditions: sample was injected for 1 sec at 10 mbar into a 70 cm long with effective length of 49 cm and 75 µm I.D. capillary. Separation at +25 kV, LED detection at 470 nm using 50 mM TAPS buffer containing 0.1 mM PAR adjusted to pH 8.47 using NaOH as BGE.,B).Electropherograms for separation of cations in river water using 3D printed slit. Experimental conditions: sample was injected for 1sec at 10 mbar into a 70 cm long with effective length of 49 cm and 75 µm I.D. capillary. Separation at +25 kV, LED detection at 470 nm using 50 mM TAPS buffer containing 0.1 mM PAR adjusted to pH 8.47 using NaOH as BGE.

Table 2.1. Determination of LOD, noise, and signal to noise (S/N) ratio for Cu^{2+}(0.1mM) and Zn^{2+}(0.1mM) using 3D printed slit and Agilent interface

	3D Printed Slit		Agilent Interface	
	Cu^{2+}	Zn^{2+}	Cu^{2+}	Zn^{2+}
Noise(mAu)	0.10	0.10	0.06	0.06
s/n	44	67	130	180
LOD (µM)	6.8	4.5	2.8	1.6

2.5. Conclusion

In this work, a single piece detector body containing a slit for photometric detection was fabricated using a FDM printer. Optimisation of the print orientation allowed for the printing of slits with widths down to 70 µm. Equipped with a LED and photodiode, the detector's performance was equivalent to detector bodies made using traditional means based on linear range, effective path length and stray light. The performance of the 3D printed housing was compared with a commercially available detection interface for the CE analysis of Cu^{2+} and Zn^{2+} complexes and was applied to the analysis of river water collected from the Tasmanian West Coast.

This work demonstrated the use of a FDM printer for the fabrication of a detector body containing a high precision slit, where easy design modifications provide an attractive means to custom-designed instrumentation.

2.6. Acknowledgements

MCB and MM wish to acknowledge Australian Research Council Future Fellowship awards (No FT120100559 and FT130100101, respectively). RMG would like to acknowledge the Alexander von Humboldt Foundation for the award of a fellowship for Experienced Researchers.MZ wish to acknowledge University of Tasmania REGS grant (OP.108709).

2.7. Electronic supplementary material

2.7.1. Abstract

This Electronic supplementary material contains additional information on the design elements of the detection body for on-capillary/tubing detection and the optical alignment and further shows the repeatability of the self-alignment feature of the detector assembly.

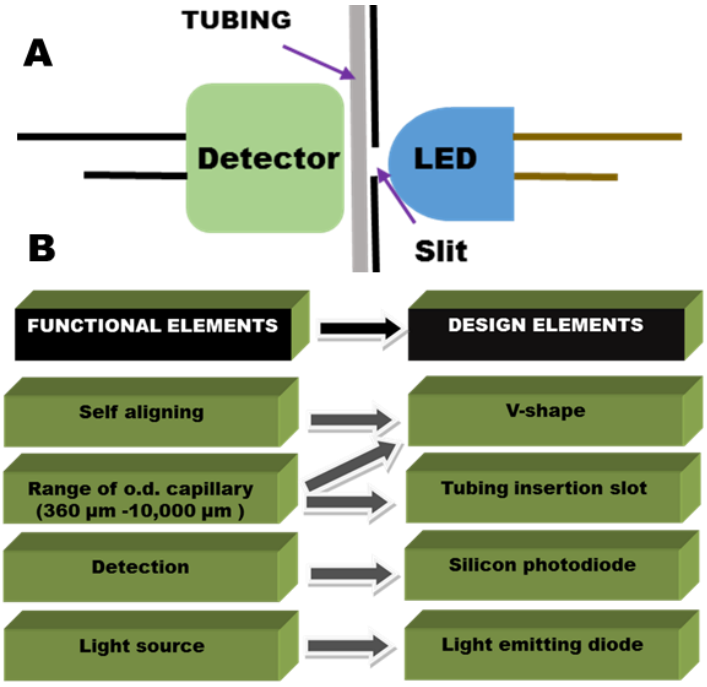

Fig.2.1.1. A Schematic on-capillary photometric detection simplified design. B) Schematic representation of functional elements relating to design elements.

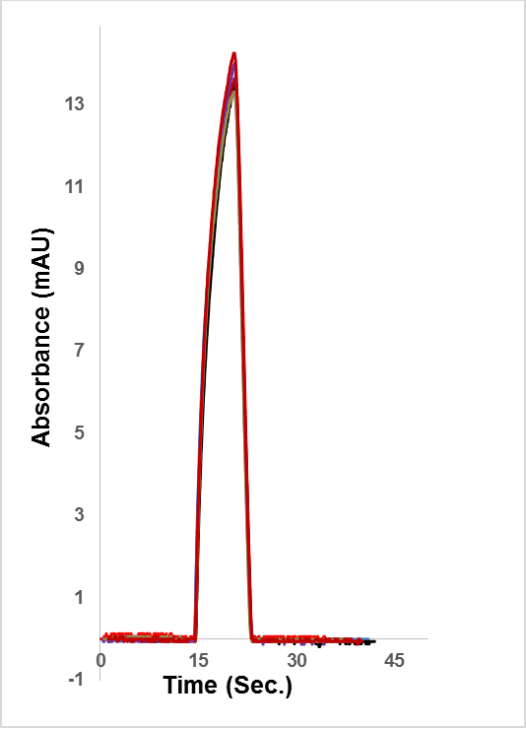

Fig. 2.1.2. Absorbance *vs* time graph for 10 replicates of flow injection analysis of 15 µL Orange G (0.125mM) at 90 µL/min flow rate using 75 µm i.d capillary.

2.7. Reference

[1] M. Macka, T. Piasecki, P.K. Dasgupta, Light-emitting diodes for analytical chemistry, Annual Review Analytical Chemistry 7 (2014) 183-207.

[2] M. Trojanowicz, Applications of flow injection methods in routine analysis, in: M. Trojanowicz (Ed.) Flow Injection Analysis: Instrumentation and Applications, World Scientific Publishing, Singapore, 2000, pp. 298-418.

[3] S.F.Y. Li, Journal of chromatography library, in: S.F.Y. Li (Ed.) Capillary electrophoresis: principles, practice and applications, Elsevier Science Publisher, Netherlands, 1993, pp. 377-531.

[4] S. Fanali, P.R. Haddad, C. Poole, P. Schoenmakers, D.K. Lloyd, Liquid chromatography: Applications, Elsevier USA, 2013.

[5] D.A. Bui, P.C. Hauser, Analytical devices based on light-emitting diodes - a review of the state-of-the-art, Analytica Chimica Acta 853 (2015) 46-58.

[6] G.J. Opiteck, K.C. Lewis, J.W. Jorgenson, R.J. Anderegg, Comprehensive on-line LC/LC/MS of proteins, Analytical Chemistry 69 (1997) 1518-1524.

[7] M. Trojanowicz, J. Szpunarlobinska, Simultaneous flow-injection determination of aluminium and zinc using LED photometric detection, Analytica Chimica Acta 230 (1990) 125-130.

[8] R.M. Guijt, C.J. Evenhuis, M. Macka, P.R. Haddad, Conductivity detection for conventional and miniaturised capillary electrophoresis systems, Electrophoresis 25 (2004) 4032-4057.

[9] G. Witzel, A.M. Ghez, M.R. Morris, B.N. Sitarski, A. Boehle, S. Naoz, R. Campbell, E.E. Becklin, G. Canalizo, S. Chappell, T. Do, J.R. Lu, K. Matthews, L. Meyer, A. Stockton, P. Wizinowich, S. Yelda, Detection of galactic center source G2 at 3.8 μm during periapse passage, The Astrophysical Journal Letters 796 (2014) 1-8.

[10] J. Prikryl, F. Foret, Fluorescence detector for capillary separations fabricated by 3D printing, Analytical Chemistry 86 (2014) 11951-11956.

[11] S. Sandron, B. Heery, V. Gupta, D.A. Collins, E.P. Nesterenko, P.N. Nesterenko, M. Talebi, S. Beirne, F. Thompson, G.G. Wallace, D. Brabazon, F. Regan, B. Paull, 3D printed metal columns for capillary liquid chromatography, Analyst 139 (2014) 6343-6347.

[12] S. Waheed, J.M. Cabot, N.P. Macdonald, T. Lewis, R.M. Guijt, B. Paull, M.C. Breadmore, 3D printed microfluidic devices: enablers and barriers, Lab on a Chip 16 (2016) 1993-2013.

[13] B.C. Gross, J.L. Erkal, S.Y. Lockwood, C. Chen, D.M. Spence, Evaluation of 3D printing and Its potential impact on biotechnology and the chemical sciences, Analytical Chemistry 86 (2014) 3240-3253.

[14] F.B. Regan, M.P. Meaney, S.M. Lunte, Determination of metal ions by capillary electrophoresis using on-column complexation with 4-(2-pyridylazo) resorcinol following trace enrichment by peak stacking, Journal of Chromatography B-Biomedical Applications 657 (1994) 409-417.

[15] C. Johns, M. Macka, P.R. Haddad, Measurement of detector linearity and effective pathlength in capillary electrophoresis, Lc Gc Europe 16 (2003) 290-+.

[16] C. Johns, M. Macka, P.R. Haddad, Design and performance of a light-emitting diode detector compatible with a commercial capillary electrophoresis instrument, Electrophoresis 25 (2004) 3145-3152.

[17] M. Macka, P. Andersson, P.R. Haddad, Linearity evaluation in absorbance detection: The use of light-emitting diodes for on-capillary detection in capillary electrophoresis, Electrophoresis 17 (1996) 1898-1905.

[18] M. King, B. Paull, P.R. Haddad, M. Macka, Performance of a simple uv LED light source in the capillary electrophoresis of inorganic anions with indirect detection using a chromate background electrolyte, Analyst 127 (2002) 1564-1567.

[19] R.P. Oda, J.P. Landers, Introduction to capillary electrophoresis, in: J.P. Landers (Ed.) Handbook of Capillary Electrophoresis, CRC Press LLC, USA, 1996, pp. 1-49.

[20] M.L.M. Antonio L Crego, UV-Vis absorbance detection in capillary electrophoresis, in: A.R. Maria Luisa Marina, Miguel Valcárcel (Ed.) Comprehensive analytical chemistry: Analysis and Detection by Capillary Electrophoresis, Elsevier, Amsterdam, The Netherlands, 2005, pp. 225-296.

[21] C. Johns, M. Macka, P.R. Haddad, M. King, B. Paull, Practical method for evaluation of linearity and effective pathlength of on-capillary photometric detectors in capillary electrophoresis, Journal of Chromatography A 927 (2001) 237-241.

[22] L. Krcmova, A. Stjernlof, S. Mehlen, P.C. Hauser, S. Abele, B. Paull, M. Macka, Deep-UV-LEDs in photometric detection: A 255 nm LED on-capillary detector in capillary electrophoresis, Analyst 134 (2009) 2394-2396.

[23] M. Ryvolova, J. Preisler, F. Foret, P.C. Hauser, P. Krasensky, B. Paull, M. Macka, Combined contactless conductometric, photometric, and fluorimetric single point detector for capillary separation methods, Analytical Chemistry 82 (2010) 129-135.

[24] L. Van der Sneppen, C. Gooijer, W. Ubachs, F. Ariese, Cavity ring-down spectroscopy in analytical chemistry, in: R.E. Giel Berden (Ed.) Cavity Ring-Down Spectroscopy: Techniques and Applications, Wiley, United Kingdom, 2009, pp. 89-108.

[25] K.L. Sutton, C. B'Hymer, J.A. Caruso, Ultraviolet absorbance and inductively coupled plasma mass spectrometric detection for capillary electrophoresis - A comparison of detection modes and interface designs, Journal of Analytical Atomic Spectrometry 13 (1998) 885-891.

[26] O.C.R. Program, https://research.cbc.osu.edu/reel/research-modules/environmental-chemistry/chemistry-221-h221/significance-of-analytes-water/metals/

(2016 (accessed 09.09.2016).).

[27] Y. Li, P.N. Nesterenko, B. Paull, R. Stanley, M. Macka, Performance of a New 235 nm UV-LED-Based On-Capillary Photometric Detector, Analytical Chemistry 88 (2016) 12116-12121.

Chapter 3
One step multi-material 3D printing for the fabrication of a photometric detector flow cell

This chapter in in the process of submission as a research article. Minor changes e.g. numbering font size, layout and style were introduced in order to match the formatting style of the thesis, keeping the original features of the article as much as possible.

3.1. Abstract

Optical detection is the most common detection mode for many analytical assays. Photometric detection systems and their integration with analytical systems usually require several assembly parts and manual alignment of the capillary/tubing which affects sensitivity and repeatability. 3D printing is an innovative technology for the fabrication of integrated complex detection systems. One step multi-material 3D printing has been explored to fabricate a photometric detector flow cell from optically transparent and opaque materials using a dual-head FDM 3D printer. Integration of the microchannel, the detection window and the slit in a single device eliminates the need for manual alignment of fluidic and optical components, and hence improves sensitivity and repeatability. 3D printing allowed for rapid design optimisation by varying the slit dimension and optical path-length. The optimised design was evaluated by determining stray light, effective path length and the signal to noise ratio using orange G. The optimised flow cell with extended path length of 10 mm and 500 µm slit yielded 0.02 % stray light, 89% effective path length and detection limit of 2 nM. The sensitivity was also improved by 80% in the process of optimization, using a blue 470 nm LED as a light source.

3.2. Introduction

Optical detection is a common mode for many analytical analyses [1-3]. In recent years, there has been an increasing demand for the customisation and integration of detectors/ detection assemblies within microfluidic systems due to low volume sample handling and faster response time advantages. Integrated microfluidic systems allow sample introduction directly to the detection techniques thus introducing automation through minimising sample handling and human intervention. Customised detection assemblies for photometric detection [4] and combined three detection methods (contactless conductometric, photometric and fluorometric) for single point simultaneous detection of three signals[5] have been studied. However, the detection assemblies usually require various assembly parts and manual alignment of the capillary/tubing which limits the sensitivity and repeatability of the method. Therefore, the integration of the channel within the detection assembly and extended optical path length will result in improved sensitivity and repeatability of photometric detection. A photometric flow cell with integrated channel and extended path length (200 mm), resulting in four-fold increase in sensitivity, has been reported previously [6].

The flow cell design offers flexibility in adjusting the path length, however, it requires assembly of several parts including supporting blocks for housing the LED and photodiode; glass cylinders to seal the channel ends and provide the transparent detection window inside the body for the light to travel from the light source through the sample to the detector; and inlet and outlet tips, joined to the channel body by melting a small surface using a torch [6]. The manufacturing and manual assembly of various parts of the flow cell is a labour intensive and time-consuming process and is prone to error due to manual intervention. Furthermore, traditional machining methods (e.g. CNC milling) used for manufacturing

detection assembly/flow cell are time consuming, expensive and not suitable for repetitive design modifications.

3D printing/additive manufacturing converts 3D models into a physical object in a one-step manufacturing approach that can significantly quicken the innovation and product development cycle [7-12]. Recent improvements in 3D printers and the development of a wider variety of materials has seen an increase in the use of this technique for detectors [13-16], electronics [17, 18] and pneumatics valves and pumps [19, 20]. 3D printing has been used previously for the fabrication of detection assemblies for photometric and fluorescence detection due to its ability to create complex hollow structures which is otherwise challenging to achieve using traditional manufacturing techniques [13, 14]. Fused Deposition Modelling (FDM) benefits from a wide range of available materials and the availability of low-cost multiple nozzle FDM printers allow combination of different materials with varying functionality and properties into a single object [12, 13]

In our previous report, 3D printing was used to fabricate a LED detector body containing a slit for photometric detection that could be positioned on any external capillary or tubing with an outer diameter from 360 μm to 10 mm [14]. Equipped with a LED and photodiode, the detector's performance was equivalent to commercially available detection interface, and served well for on-capillary detection, primarily exploited for traditional fused silica o.d. 360 um capillaries used typically in CE or capillary LC [14]. In a different and complementary approach to our previous detector design, alternative designs of flow cells with the liquid in contact with the 3D printed cell offer some advantages worth investigating.

Here we report on the use of multi-material fused deposition modelling (FDM) 3D printing for manufacturing a single piece flow cell; consisting of an integrated slit and flow channel in an opaque body, and a transparent detection window; for photometric detection. The opaque device body and

transparent detection window were printed simultaneously using a dual-head FDM 3D printer with opaque and optically transparent materials. Integration of the flow channel, the detection window and the slit in the single device eliminated the need for manual alignment of fluidic and optical components, and hence improved repeatability. 3D printing allowed for rapid design optimisation by varying the slit dimension and optical path-length. The optimised design was characterised by determining stray light, effective path length and the signal to noise ratio using orange G.

3.3. Materials and method

3.3.1. Chemicals and detector characterisation

Orange G (1-phenylazo-2-naphthol-6,8-disulfonic acid disodium salt) of Standard Fluka quality was obtained from Fluka (Buchs, Switzerland). Water was purified from deionized water using a Milli-Q water purification system (Millipore, Bedford, MA, USA).

A series of standards was prepared by serial dilution of stock solution of Orange G. The absorbance was calculated by the data acquisition system from the signal as its logarithmic function. The detector flow cell channel was first flushed with water and then with the Orange G standards. The flow was stopped and the absorbance was measured under static conditions. Each test solution was measured in triplicate and in order of increasing concentration. From the sensitivity vs absorbance curve, the effective path length and percentage of stray light values were calculated. Determination of stray light by filling the detection cell with a highly absorbing solution is well justified in principle, well established and has been used previously [14].

3.3.2. Designing and fabrication

The computer aided design (CAD) of the detector flow cell was made by using Inventor Pro. A FDM printer (Felix 3.0, Felix robotics, the Netherlands) used in combination with black Polylactic acid (PLA) material and transparent PLA (Matter Hackers, CA, USA) was used to print the flow-detector from the STL files using the printer's proprietary software. The extruder temperature was 210°C, the print bed was 70 °C and the extruded filament size was 150 µm.

3.3.3. Instrumentation

The detection system comprised of a multicolour (Red 630 nm, Blue 470 nm, Green 525 nm) LED (5 mm, 30 mA maximum steady current) from LigCom Group (Glen Cove, NY, USA) and a silicon photodiode (TSL RS-LF) from RS Australia (Smithfield, NSW, Australia). Labview (SP1 2011) software was used for control of all components from National instruments (Macquarie park, NSW, Australia). An I/O module (NI-DAQ National instruments (Macquarie park, NSW, Australia) was used for data collection, display and analysis of the detector flow cell signals.

3.4. Result and discussion

3.4.1. Flow-cell design and general considerations

The key elements for the flow-cell design include: (i) minimum or no assembly supporting repeatability and robustness, (ii) housing for the LED and photodiode, (iii) integrated slits to reduce stray light and provide optimum optical performance, (iv) transparent detection windows at a pre-defined distance determining the optical path length, (v) fluidic ports for interfacing at the flow cell's inlet and outlet. This was achieved by designing and 3D printing the entire flow cell including all the functional parts

integrated into a single device body. A multi-material 3D printer with dual nozzle allowed printing of the device body with an opaque material, black PLA, and the transparent detection window using a visibly transparent PLA filament. Integration of the slit and flow channel in a single body reduced the time required for setup compared with our previous report, where positioning of the tubing within the optical path was critical for optimal optical performance [21], as defined by low stray light, high effective path and high signal to noise ratio. In our new design, the cavities for the LED and photodiode were positioned on each side of the slit which facilitated quick plugging of the LED and photodiode on the device, with the path length defined by the length between the slits. The novel design resulted in a simple device which required no assembly parts. The CAD design and a photograph of the 3D printed photometric detector flow cell are shown in Fig.3.1.

To examine the repeatability of the cell, four cells with path lengths ranging from ranging from 7.5 to 15 mm, were printed three times (n=3) and a coloured dye was used to observe the length of the cells under the microscope. The data in Table S.3.1 shows good agreement between the design and printed

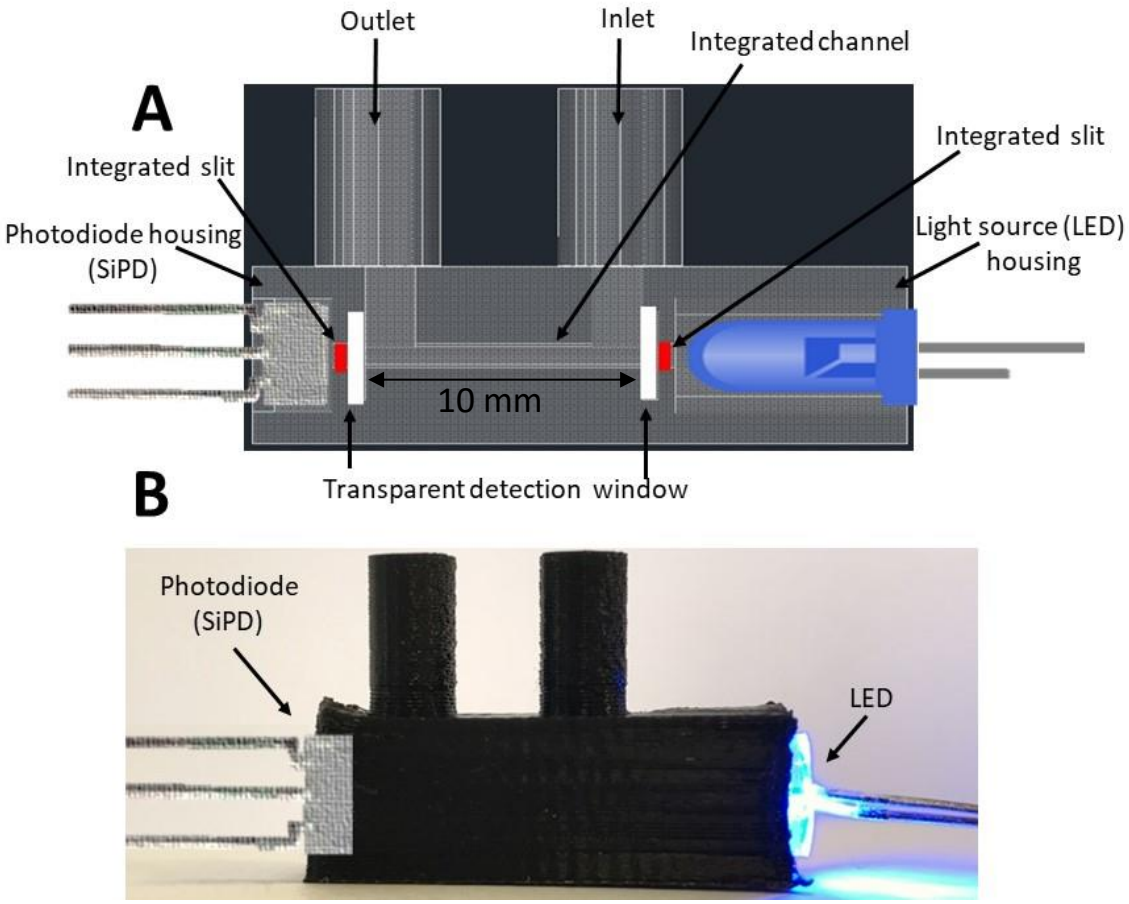

Fig.3.1. A) CAD design of the detector flow cell and illustration of its different parts B) 3D printed photometric detector flow cell

pathlengths, with on average, the design length being ~ 99% of the design length. The repeatability of each design was also acceptable, with an error of % RSD ranging from 0.06 to 0.27 %. These results demonstrate the excellent repeatability of the 3D printed cells and a close agreement of the designed parameters with the printed parts for our device.

3D printers print the object layer by layer and transparent walls will have impression of the layers. To see that behaviour and its effect on optical performance the optical characterization for the flow cell

including transparent detection window was performed. Orange G has been commonly used in previous studies as the model analyte for the characterisation of the optical detectors/ detection methods [22, 23], therefore it was chosen as the test analyte for the characterisation of the newly developed flow cell.

3.4.2 LED emission spectrum

The prerequisite of choosing an LED as a light source that its emission spectrum and the absorption spectrum of the compound under study should present a wide overlap [6, 24]. To confirm that orange G is a suitable compound spectrally matching the blue LED, the absorption spectrum of orange G and emission spectrum of the LED were recorded, which are shown in Fig.3.2. It can be seen that two spectra present a wide overlap with the maximum of LED emission measured at 466 nm, and the maximum absorption of the orange G compound is measured at 472 nm. These results showed that 470 nm blue LED could be chosen as the light source for photometric detection of the Orange G, therefore this compound was chosen for the characterization of the flow cell.

3.4.3. Comparison and optimization of optical performance of the detector flow cell design

Practically, the performance of a photometric detector is determined by the signal to noise ratio that can be obtained. Optimum performance is associated with low stray light and high effective optical path length, which are influenced by the actual detection cell length and slit size. Therefore, the performance of the 3D printed photometric flow cell was characterised by measuring the % stray light and effective optical path length. Flow cells with various slit sizes and optical pathlengths were characterised to

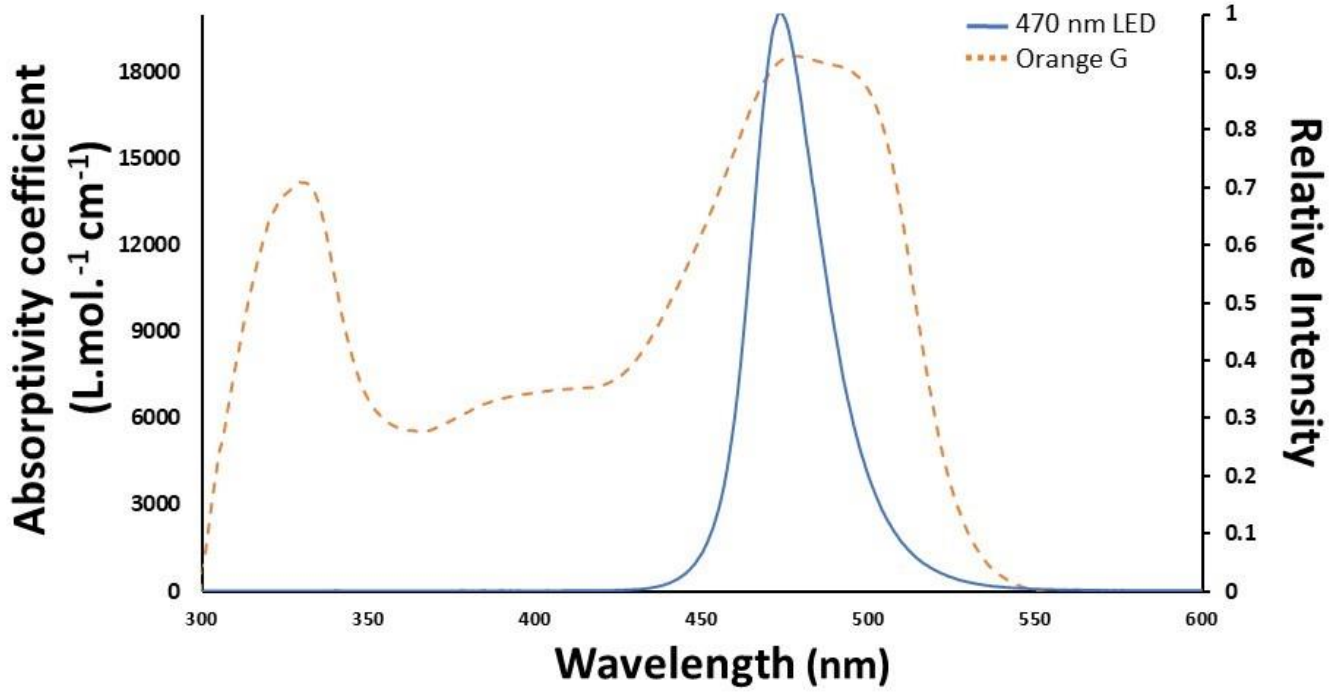

Fig.3.2. Superimpose of the absorption spectrum of Orange G and emission spectrum of blue 470

investigate the device with optimum performance. The signal to noise and detection limit were determined using orange G solutions.

Theory

The flow cell was designed to accommodate silicon photodiode and LED on each side, allowing optimal use of the radiation emitted by the blue LED. Flow cells with various optical path lengths (7.5–15 mm) and slit sizes (200–500 µm, squared shaped slits with 300 µm depth i.e. 200 x 200 x 300 to 500 x 500 x 300) were fabricated, further details on printing parameters and slit geometry are provided elsewhere [4]. Each flow cell was assessed on agreement with Beer–Lambert law [25, 26], Eq. 1, Although the Beer-

Lambert-Bouguer law used in the form of Eq. 1 is valid for monochromatic light, the influence of non-monochromacity of LED emission spectra has been examined in detail and shown that its effect on detection linearity is negligible [25, 26].

$$A_{real} = \log\frac{I_0}{I} = \varepsilon.\ell.c \qquad \text{(Eq.1)}$$

where (A_{real}) = absorbance of the analyte; I_0= Intensity of light incident upon the sample cell; I =Intensity of light leaving sample cell; ε = molar absorption coefficient (18546 $L.mol^{-1}cm^{-1}$); c= concentration of the sample; ℓ= path length of the cell.

The sensitivity (S), the signal of the analyte per unit concentration, is calculated by dividing the measured absorbance (A_{eff}) with the concentration (used for absorbance measurement) of the sample [26, 27],

$$S = \frac{A_{eff}}{C} \qquad \text{(Eq.2).}$$

The effective path length, ℓ_{eff}, was determined by rearranging the Beer-Lambert law, the plot of S (A/C) vs (A_{eff}) Fig.3.2 could be used to determine the effective path length by extrapolating the graph to zero absorbance or dividing this S by ε.[14].

The Following equations were used for calculations;

$A = \varepsilon.\ell.c$ (from Eq. (1) (Eq. 3),

$$\ell = \frac{A_{eff}}{\varepsilon.c} \qquad \text{(Eq. 4)}$$

$$\ell_{eff.} = \frac{S}{\varepsilon} \qquad \text{(Eq.5)}$$

Any light coming from the LED outside of the cell, is not going to be detected by the detector, which is the case for stray light. The stray light- detected light that does not belong to the bandwidth of the selected wavelength - was determined as the percentage relative to the incident light and is calculated from the maximum absorbance ($A_{max.}$) of the analyte.[5, 14],

stray light % = 100 x $10^{-(A_{max})}$ (Eq. 6)

3.4.4. Optimisation of slit size

In photometric detection, the slit plays a vital role in light collimation and optical performance [14, 26, 28, 29]. Ro et al. reported a significant increase in effective path length by introduction of a slit when compared to a similar detector design without a slit [29]. In this work is we used an opaque channel with transparent detection window to see the effect on sensitivity, effective path length and stray light. In this design the LED housing was made in a way so that LED was inserted inside the opaque long housing which minimise the stray light and black opaque walls of the channel absorb stray light as well. To pass the light, transparent detection windows were printed on each end of the flow cell, with a small opaque slit printed adjacent to the transparent material. Square slits ranging from 200 - 500 µm were incorporated on both ends of the flow-cell and their effect on detector performance was studied by determining the linearity, effective path length, and stray light of Orange G as previously reported [26, 27, 30]. A flow cell with 10 mm optical path length (average channel length of each flow cell after 3D printing (*n*=3) is 9.98) was used for optimising the slit size. The detector performance was determined by measuring the absorbance of Orange G over a concentration range of 0.0097 to 20 mM by Eq.1, which

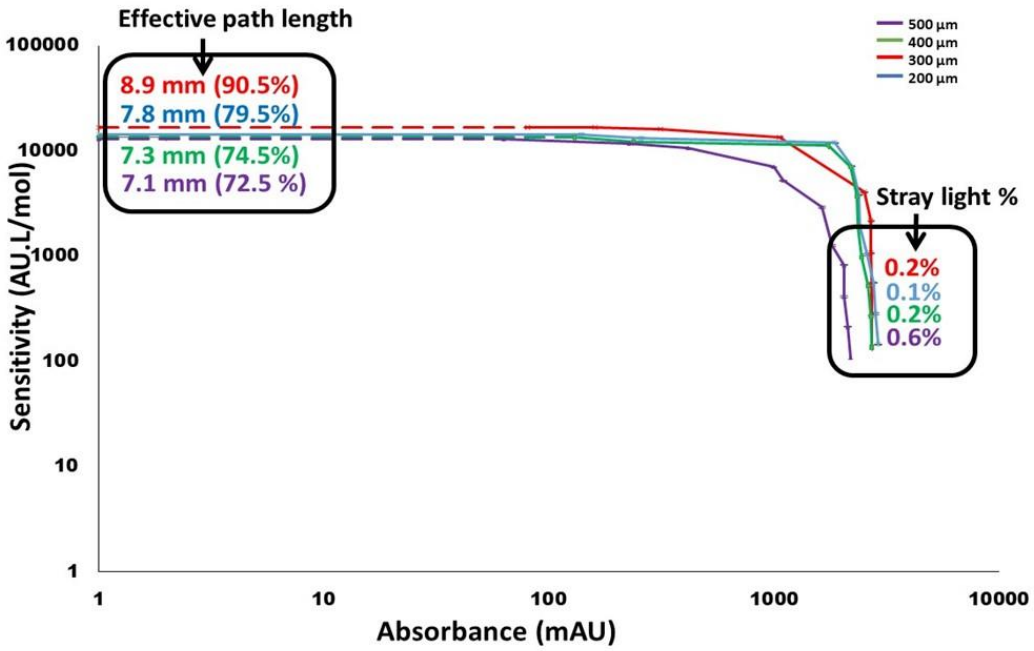

Fig.3.3. The plot of detection linearity depicted as a sensitivity (AU.L/mol) vs absorbance (mAU) graph. The average channel length of each flow cell after 3D printing (*n*=3) is 9.98 mm and the slit sizes ranges from 200 to 500 µm in examined cells. The test analyte was Orange G (measured molar absorption coefficient = 18546 $L.mol^{-1}cm^{-1}$).

was used to calculate the sensitivity. The sensitivity calculated by Eq.2 was found to be in the range of 13046 to 16683 AU.L/ mol. for the 200 to 500 µm slits.

The Beer-Lambert law allows for determining the effective path length by extrapolating the S vs A graph to zero absorbance and dividing this by ε obtained from Eq.5. For a flow cell with 10 mm path length, effective path-lengths of 7.1 mm (72.5 %), 7.3 mm (74.53 %), 7.8 mm (79.5 %) and 8.9 mm (90.5 %) were obtained for the 200, 300, 400 and 500 µm slits, respectively, values that are comparable to the literature values for photometric detection systems [14, 26, 29-32]. This is graphically depicted in Fig.3.3.

Table 3.1. LOD, noise, and signal to noise (S/N) ratio calculted for orange G (0.0097 mM) using 3D printed photometric detector f low cell with various slit sizes (path length = 10 mm designed)

Slit size	200 µm	300 µm	400 µm	500 µm
Noise(mAU)	0.40	0.26	0.18	0.011
s/n	320	490	800	15000
LOD (µM) ±SD	0.091±0.0097	0.059±0.0042	0.036±0.0019	0.0020±0.00010

The percentage of stray light can also be determined from Fig.3.3, and was determined using Eq.6. Values for stray light ranged from 0.1 to 0.6 % for the slits ranging from 200 to 500 µm. This is almost a 35 fold improvement in comparison with our previously reported LED based 3D printed photometric detection assembly, where stray light was 3.8 % [14]. This improvement is most likely due to the improved positioning of the flow cell within the optical path and agrees well with previously reported values ranging from 0.6 to 50 % for LED based detectors [29, 31-33]

The final numerical parameter used to characterise the photometric detector performance was the baseline noise. The stability with which the LED and photodiode are positioned affects the vibration, with enhanced stability reducing baseline noise. With the detection limit determined by the signal to noise ratio, decreasing the baseline noise results in a lower limit of detection. The noise (n=3) was calculated by estimating the short time variation of the baseline, average value provided in Table 3.1 and the limits of detection (LOD) for the method were calculated based on a signal to noise ratio of 3. The noise, signal to noise ratio and detection limit were determined for Orange G using the 200, 300, 400 and 500 µm slit and are given in Table 3.1, with values comparable to literature reports for similar dyes [34]. It was observed that the slit in this arrangement is reducing the light intensity which could be

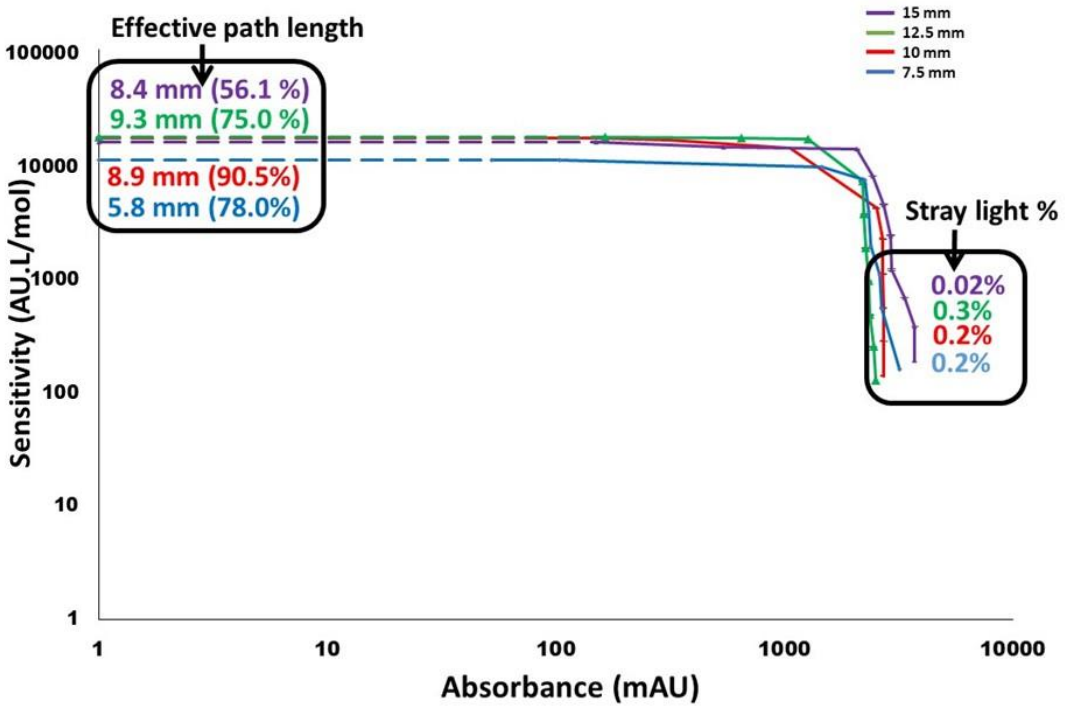

Fig.3.4. The plot of detection linearity depicted as a sensitivity (AU.L/mol) vs absorbance (mAU) graph. The size of the slit is 500 µm in all the flow cells. The average channel length, 7.47, 9.98, 12.47 and 14.98 mm (designed path length 7.5, 10, 12.5 and 15 mm respectively), for each 3D printed flow cell was used for performing the calculations. Orange G, molar absorption coefficient measured to be 18546 $L.mol^{-1}cm^{-1}$, was used as the test the reason for the increase in noise values. These results also showed that the slit also has minimal effect of stray light on these extended path length flow cells. Based on these results, a 500 µm slit provided the best optical performance with highest effective path length, minimum stray light and lowest limit of detection.

3.4.5. Optimisation of path length

Path length is a key element for optical detectors as it ultimately determines the signal intensity and the limit of detection [29, 35]. Sensitivity increases by increasing path length of the flow cell [36] but after certain path length the intensity of light decreases and sensitivity starts to drop [37, 38]. Therefore, it is important to optimise the path length in order to obtain the best performance of the flow cell.

Table 3.2. LOD, noise, and signal to noise (S/N) ratio calculated for orange G(0.0097 mM) using 3D printed photometric detector flow cell with various pathlengths designed(slit size = 500 µm)

Path length	7.5 mm	10 mm	12.5 mm	15 mm
Noise(mAU)	0.012	0.011	0.021	0.030
s/n	8700	15000	7875	5000
LOD (µM) ±SD	0.0033±0.00023	0.0020±0.00010	0.0037±0.00028	0.0058±0.00045

Photometric detectors with different optical path lengths of 7.5, 10, 12.5 and 15 mm were printed, which had measured average path lengths of 7.47, 9.98, 12.47 and 14.98 mm respectively. These cells were evaluated using the approach discussed in 3.2.1. Fig.3.4 shows the sensitivity vs absorbance plot for the different flow cell lengths. From these data, the effective path length was determined to be 5.82 mm (78.0 %), 8.9 mm (90.5 %), 9.3 mm (75.0 %) and 8.4 mm (56.1%) for the 7.5, 10, 12.5 and 15 mm channel lengths, respectively, which are comparable to literature values reported for other systems [5, 14, 26, 27, 29-33].

The sensitivity was found to be in the range of 10808 to 17020 AU.L/ mol. for the 7.5 to 15 mm path length. Again, the sensitivity values obtained using the newly printed flow cell are ~ 20 time better than the previously reported work on 3D printed photometric detection assembly. For the presented photometric cells, the percentage of effective path length increases when the detection path increases from 7.5 mm to 10 mm, but decreases when the channel length exceeds 12.5 mm. This decrease in the percentage of effective path length above 10 mm is possibly because of decreased light intensity at such large path length. Therefore, these results show that a path length of 10 mm has an optimum effective path length with a maximum effective path length of 90 %. These results with the obtained value of 90

% effective path length in optimized flow cell also demonstrate that the transparent window is not very much affected by the layer by layer printing process.

The % stray light was calculated to in the range of 0.1 to 0.3 % for the 7.5 to 15 mm channel lengths, again superior to our previously reported 3D printed photometric detector, and is in good agreement with other reported stray light values (0.6-50%) [29, 31-33]. The reported effective path length and stray light agree with the measured noise level of the photometric detectors, tabulated together with corresponding detection limits in table 3.2. These results showed that the LOD decrease by increasing the path length up to 10 mm, however above this path length there was an increase in LOD which is could be because of decreased light intensity at such large path length, thus showing 10 mm as the optimum path length with maximum light intensity for the 3D printed flow cell. It must also be noted that for noise values the difference between the two smallest windows is relatively small and therefor the small difference in the determined corresponding level of noise can be regarded as acceptable. Importantly, for the larger windows, the noise levels determined follow an expected trend with decreasing levels of noise for larger windows as a result of higher levels of light through the larger windows. The performance of the 3D printed flow cell is comparable to literature values reported for similar detection systems machined using conventional manufacturing approaches. [14, 26, 29-32, 34, 39].

After considering all the optimising parameters, the performance of the flow cell with 10 mm path length and 500 µm slit was found to be the best of the flow cells characterized in this work and was 80% more sensitive than poorest performing photometric flow cell. The sensitivity of the flow cell was improved by a factor 20 compared with our previously work [14].

3.5. Conclusion

Herein, the potential of multi-material 3D printing was explored to fabricate a novel photometric flow cell design which consisted of integrated channel along with cavities for LED and photodiode and incorporates a visibly transparent material in an otherwise opaque embodiment to allow for the light to travel between light source and detector. Simultaneous printing of functional components of variable properties facilitates integration of various parts into a single object, hence providing opportunities to minimise assembly parts and introduce automation. Additionally, the simplicity of design and fabrication suggest that multi-material 3D printing may provide a low-cost and flexible way to construct and integrate photometric detection in instrumentation used for chemical analysis. This study demonstrates the capability of 3D printing to fabricate photometric flow cells with complex features, such as transparent detection window within an opaque body, with an utmost simplicity that is not comparable to existing manufacturing approaches.

3.6. Supplementary information:

TabSle.S3.1. Comparison of designed vs measured pathlengths for the 3D printed flow cells (Average, *n*=3), channel was filled with a coloured dye to observe the length of the flow cells under the microscope.

Designed path length (mm)	3D printed path length (mm)	% RSD
15	14.98	0.067
12.5	12.47	0.081
10	9.98	0.15
7.5	7.47	0.28

3.7. References

[1] G.J. Opiteck, K.C. Lewis, J.W. Jorgenson, R.J. Anderegg, Comprehensive on-line LC/LC/MS of proteins, Anal. Chem. 69 (1997) 1518-1524.

[2] M. Trojanowicz, J. Szpunarlobinska, Simultaneous flow-injection determination of aluminium and zinc using LED photometric detection, Anal. Chim. Acta 230 (1990) 125-130.

[3] R.M. Guijt, C.J. Evenhuis, M. Macka, P.R. Haddad, Conductivity detection for conventional and miniaturised capillary electrophoresis systems, Electrophoresis 25 (2004) 4032-4057.

[4] F. Cecil, M. Zhang, R.M. Guijt, A. Henderson, P.N. Nesterenko, B. Paull, M.C. Breadmore, M. Macka, 3D printed LED based on-capillary detector housing with integrated slit, Anal. Chim. Acta 965 (2017) 131-136.

[5] M. Ryvolova, J. Preisler, F. Foret, P.C. Hauser, P. Krasensky, B. Paull, M. Macka, Combined contactless conductometric, photometric, and fluorimetric single point detector for capillary separation methods, Anal. Chem. 82 (2010) 129-135.

[6] T. R. Dias, M. Brasil, M. Feres, B. Reis, A flow cell with a new design to improve the utilization of the radiation emitted by LED and employed as a radiation source for photometric detection, Sens Actuators B Chem 198 (2014) 448-454.

[7] P. Sitthi-Amorn, J.E. Ramos, Y. Wangy, J. Kwan, J. Lan, W. Wang, W. Matusik, MultiFab: a machine vision assisted platform for multi-material 3D printing, ACM Trans. Graph. 34 (2015) 1-11.

[8] N. Macdonald, J. Cabot, P. Smejkal, R. Guijt, B. Paull, M. Breadmore, Comparing microfluidic performance of 3D printing platforms, Anal. Chem. 89 (2017).

[9] U. Kalsoom, A. Peristyy, P. Nesterenko, B. Paull, A 3D printable diamond polymer composite: A novel material for fabrication of low cost thermally conducting devices, RSC Advances 6 (2016).

[10] V. Gupta, S. Beirne, P. Nesterenko, B. Paull, Investigating the Effect of Column Geometry on Separation Efficiency using 3D Printed Liquid Chromatographic Columns Containing Polymer Monolithic Phases, Anal. Chem. 90 (2017) 1186-1194.

[11] U. Kalsoom, P.N. Nesterenko, B. Paull, Recent developments in 3D printable composite materials, RSC Advances 6 (2016) 60355-60371.

[12] F. Li, N. Macdonald, R. Guijt, M. Breadmore, Using printing orientation for tuning fluidic behaviour in microfluidic chips made by fused deposition modelling (FDM) 3D printing, Anal. Chem. 89 (2017).

[13] J. Prikryl, F. Foret, Fluorescence detector for capillary separations fabricated by 3D printing, Anal. Chem. 86 (2014) 11951-11956.

[14] F. Cecil, M. Zhang, R.M. Guijt, A. Henderson, P.N. Nesterenko, B. Paull, M.C. Breadmore, M. Macka, 3D printed LED based on-capillary detector housing with integrated slit, Analytica Chimica Acta 965 (2017) 131-136.

[15] H. Ota, M. Chao, Y. Gao, E. Wu, L.-C. Tai, K. Chen, Y. Matsuoka, K. Iwai, H.M. Fahad, W. Gao, H.Y.Y. Nyein, L. Lin, A. Javey, 3D Printed "earable" smart devices for real-time detection of core body temperature, ACS Sensors 2 (2017) 990-997.

[16] U. Kalsoom, P.N. Nesterenko, B. Paull, Current and future impact of 3D printing on the separation sciences, Trends Anal. Chem. 105 (2018) 492-502.

[17] E. Macdonald, R. Salas, D. Espalin, M. Perez, E. Aguilera, D. Muse, R.B. Wicker, 3D Printing for the Rapid Prototyping of Structural Electronics, IEEE Access 2 (2014) 234-242.

[18] Y.L. Kong, I.A. Tamargo, H. Kim, B.N. Johnson, M.K. Gupta, T.-W. Koh, H.-A. Chin, D.A. Steingart, B.P. Rand, M.C. McAlpine, 3D Printed quantum dot light-emitting diodes, Nano Lett. 14 (2014) 7017-7023.

[19] H. Gong, A.T. Woolley, G.P. Nordin, High density 3D printed microfluidic valves, pumps, and multiplexers, Lab Chip 16 (2016) 2450-2458.

[20] J.Y. Wang, P. Yao, N.D. Jiao, S. Tung, L.Q. Liu, J.Y. Wang, P. Yao, Ieee, Pneumatic pump chip by 3D printing technology, in: 2015 International Conference on Manipulation, Manufacturing and Measurement on the Nanoscale, 2015, pp. 240-244.

[21] R.P. Oda, J.P. Landers, Introduction to capillary electrophoresis, in: J.P. Landers (Ed.) Handbook of Capillary Electrophoresis, CRC Press LLC, USA, 1996, pp. 1-49.

[22] J.L. Felhofer, L. Blanes, C.D. Garcia, Recent developments in instrumentation for capillary electrophoresis and microchip-capillary electrophoresis, Electrophoresis 31 (2010) 2469-2486.

[23] G.A. Heras, M.C. Breadmore, C. Johns, J.P. Hutchinson, E.F. Hilder, P. Lopez-Mahia, P.R. Haddad, Indirect photometric detection of anions in nonaqueous capillary electrophoresis employing Orange G as probe and a light-emitting diode-based detector, Electrophoresis 29 (2008) 3032-3037.

[24] M. Macka, C. Johns, P. Doble, P.R. Haddad, Indirect photometric detection in CE using buffered electrolytes - Part II, practical rules, LC GC North America 19 (2001) 178.

[25] I. Botev, A new conception of Bouguer-Lambert-Beer's law, Fresenius' Zeitschrift für analytische Chemie 297 (1979) 419-419.

[26] M. Macka, P. Andersson, P.R. Haddad, Linearity evaluation in absorbance detection: The use of light-emitting diodes for on-capillary detection in capillary electrophoresis, Electrophoresis 17 (1996) 1898-1905.

[27] C. Johns, M. Macka, P.R. Haddad, M. King, B. Paull, Practical method for evaluation of linearity and effective pathlength of on-capillary photometric detectors in capillary electrophoresis, J. Chrom. A 927 (2001) 237-241.

[28] S. Sharma, H.D. Tolley, P.B. Farnsworth, M.L. Lee, LED-Based UV Absorption Detector with Low Detection Limits for Capillary Liquid Chromatography, Anal. Chem. 87 (2015) 1381-1386.

[29] K.W. Ro, K. Lim, B.C. Shim, J.H. Hahn, Integrated light collimating system for extended optical-path-length absorbance detection in microchip-based capillary electrophoresis, Anal. Chem. 77 (2005) 5160-5166.

[30] C. Johns, M. Macka, P.R. Haddad, Measurement of detector linearity and effective pathlength in capillary electrophoresis, LC GC Eur. 16 (2003) 290.

[31] Y. Li, P.N. Nesterenko, B. Paull, R. Stanley, M. Macka, Performance of a New 235 nm UV-LED-Based On-Capillary Photometric Detector, Anal. Chem. 88 (2016) 12116-12121.

[32] L. Krcmova, A. Stjernlof, S. Mehlen, P.C. Hauser, S. Abele, B. Paull, M. Macka, Deep-UV-LEDs in photometric detection: a 255 nm LED on-capillary detector in capillary electrophoresis, Analyst 134 (2009) 2394-2396.

[33] M. King, B. Paull, P.R. Haddad, M. Macka, Performance of a simple uv LED light source in the capillary electrophoresis of inorganic anions with indirect detection using a chromate background electrolyte, Analyst 127 (2002) 1564-1567.

[34] L. Van der Sneppen, C. Gooijer, W. Ubachs, F. Ariese, Cavity ring-down spectroscopy in analytical chemistry, in: R.E. Giel Berden (Ed.) Cavity Ring-Down Spectroscopy: Techniques and Applications, Wiley, United Kingdom, 2009, pp. 89-108.

[35] S. Kim, W. Kim, J.H. Hahn, Extended path-length postcolumn flow cell for UV-visible absorbency detection in capillary electrophoresis, J. Chrom. A 680 (1994) 109-116.

[36] S. Liu, P.K. Dasgupta, A simple means to increase absorbance detection sensitivity in capillary zone electrophoresis, Anal. Chim. Acta 283 (1993) 747-753.

[37] P.S. Jensen, J. Bak, Near-infrared transmission spectroscopy of aqueous solutions: influence of optical pathlength on signal-to-noise ratio, Appl. Spectrosc. 56 (2002) 1600-1606.

[38] T. Inagaki, T. Watanabe, S. Tsuchikawa, The effect of path length, light intensity and co-added time on the detection limit associated with NIR spectroscopy of potassium hydrogen phthalate in aqueous solution, PLoS ONE 12 (2017) e0176920.

[39] Z.A. Alothman, Y.E. Unsal, M. Habila, A. Shabaka, M. Tuzen, M. Soylak, Membrane filtration of Sudan orange G on a cellulose acetate membrane filter for separation–preconcentration and spectrophotometric determination in water, chili powder, chili sauce and tomato sauce samples, Food Chem. Toxicol. 50 (2012) 2709-2713.

Table 3.1. LOD, noise, and signal to noise (S/N) ratio calculted for orange G (0.0097 mM) using 3D printed photometric detector f low cell with various slit sizes (path length = 10 mm designed)

Slit size	200 µm	300 µm	400 µm	500 µm
Noise(mAU)	0.40	0.26	0.18	0.011
s/n	320	490	800	15000
LOD (µM) ±SD	0.091±0.0097	0.059±0.0042	0.036±0.0019	0.0020±0.00010

Chapter 4
3D printed non-terminal electroosmotic pump

This chapter is submitted in Anal. Chem. as a research article. Minor changes e.g. numbering font size, layout and style were introduced in order to match the formatting style of the thesis, keeping the original features of the article as much as possible.

4.1. Abstract

Multi-material fused deposition modelling (FDM) facilitated the fabrication of the electrically conducting electrodes and insulating device components all in one-piece, resulting in an assembly free non-terminal EOP. A non-terminal electro-osmotic pumps (EOP) is an EOP with its fluidic terminals grounded therefore not affecting its fluidic environment. An infill mesh with square apertures was used to provide a high surface area element with significantly enhanced surface area compared with a second element with

the same O.D. but only containing a single 1 mm I.D. through cavity. Both elements were printed in non-conductive acrylonitrile butadiene styrene (ABS) and integrated with three electrodes printed in conducting ABS in an alternating configuration. The 3D printed EOP was characterized by measuring the current, flow rate and pressure at various voltages. An increase in voltage from 100 – 500 V resulted in an increase in pressure (11.61 - 255.50 Pa), current (15 - 68 μA) and flow rate (0.3 - 4.9 nL/sec), respectively, which is similar to other EOPs. This non-terminal EOP introduces asymmetry in surface area along the EOP to allow for a net flow, eliminating the need for surface modification. This device, which can be made in 35 min in a single manufacturing step using a consumer-grade 3D printer provides an attractive alternative EOP

4.2. Introduction

Fluid pumping is a key feature of a microfluidic system and usually requires a micro pump to manipulate liquid flow at a smaller scale (≤ 1 mm). The fluid transport through a micro pump can be based on pressure, current, magnetic field, capillary action or electro osmosis. [1-3] Electroosmotic pumps (EOPs) have found wide range of applications including in high performance liquid chromatography (HPLC) [4-6], chip based assays [7-9], microchannel cooling system [10], drug delivery [11, 12], and device actuation [11].

In an EOP, fluidic movement is driven by the electroosmotic flow which is caused by the electric double layer, consisting of a compact layer on the channel walls and a diffused layer in the liquid, formed due the electrostatic interaction between the channel surface and uncharged liquid (e.g. aqueous solution) [13]. EOPs have some limitations: they are not self-priming and must be filled with electrolyte prior to operation, electrolysis produced bubbles may cause blockages and inconsistent flow rates, and the

adsorption of compounds from the liquid onto the surfaces of the pumping elements may affect the reliability and robustness [14]. However, EOPs offer significant advantages over conventional pumping systems in that they exclude the need for moving parts, simplicity in controlling the flow magnitude and directions, and ability to achieve high flow rates [15, 16]. Initially, the integration of EOPs was limited by the requirement of having the high voltage electrode in a terminal position to prevent electrokinetic effects throughout the fluidic system. Through customizing the surface chemistry, non-terminal EOPs were introduced by combining a + EOP and -EOP such that the flow from both pumping elements was in the same direction. In this design, a central electrode for application of the potential is shared allowing for ground electrodes at either end [17]. Additionally, EOPs have been used in microfluidic systems due to their advantages of simple integration, compatibility with the micro technology [14] [18], capability to provide high pressure [19, 20], and a pulse free stable flow rate which is essential for reliable operation of microfluidic devices and flow injection systems [21].

EOPs are typically fabricated using subtractive manufacturing techniques such micromachining [22] and laser ablation [18] which can be expensive, time consuming and offer limited opportunities for iterative design optimization. Electrodes are required for application of the driving potential, and their integration/incorporation further increases the complexity of the manufacturing process. For example, Brask et al. fabricated electrode chambers to allow integration of spiral Pt electrodes into the EOP which resulted in additional assembly parts. The final EOP system consisted of nine assembly layers and required careful alignment of all layers that were bonded thermally with the help of nuts and bolts, which is a time consuming and labor intensive process [18].

The development of solid freeform fabrication techniques, in particular 3D-printing, has considerably enhanced the capability to fabricate structures with complex 3D geometries [23-25]. Its ability to convert

3D models to structures has the potential to quicken the innovation cycle [26-28] and 3D printing has been adopted in industry and research to produce design prototypes [29]. The widespread availability of 3D printers through print shops and their penetration into the consumer market has facilitated global sharing of designs, which allows for a rapid increase in the uptake of design innovations [30, 31]. Focusing on laboratory-based sciences, the most commonly used 3D printing technologies are stereolithography (SLA), inkjet and fused deposition modelling (FDM) [30, 32, 33]. The outstanding features of FDM are low cost and the capability to print a wide range of plastic materials including those used in traditional manufacturing [34]. For FDM printers, there is a wide range of thermoplastic materials including acrylonitrile butadiene styrene (ABS), polylactic acid (PLA), polyamide, polystyrene, and polycarbonate to allow fabrication of structures with a wide range of colours and physical, chemical, mechanical, and optical properties. Modern multi-material FDM printers allow printing with multiple materials, either by splicing filaments or using printers with multiple nozzles. Integrating materials with different properties (porosity, electrical conductivity, rigidity etc.) has allowed for the fabrication of functionally integrated devices in a single print [33, 35].

Here we present, a novel one-piece non-terminal EOP, fabricated by multi-material FDM 3D printing. ABS material was chosen for the fabrication of the pump, polymeric materials though inherently do not contain ionic groups in the chain structure but are known to develop EOF under acidic or basic conditions due to the presence of impurities or additives and therefore providing a suitable material for the fabrication of EOP [36]. Asymmetry in surface area along the pump was realized by printing an infill mesh at one side to increase the surface area in-line with the applied field, leaving the other side as a single open channel. Ground electrodes at either side of the EOP will allow for easy integration of this pump with other fluidic functionalities, while the polarity and magnitude of the applied voltage provide control

over the direction of flow and the flow rate. The performance of the proposed FDM printed EOPs was comparable to previously reported EOPs.

4.3. Materials and methods

Sodium tetraborate ($Na_2B_4O_7$) was obtained from Sigma Aldrich (Missouri, USA). Water was purified from deionized water using a Milli-Q water purification system from Millipore (Massachusetts, USA). A FDM printer from PRUSA (Prague, Czech Republic) used in combination with conductive ABS from SainSmart (Kansas, USA) and transparent ABS from Matter Hackers (CA, USA) was used to print the EOP from the STL files using the printer's proprietary software. The computer aided design (CAD) of the EOP was developed in AutoCAD (Autodesk, California, USA). The software package Labview (National Instruments, New South Wales, Australia) was used to control the power supply (Spellman High Voltage Electronics corp., New York, USA).

The printed EOP was flushed with buffer (sodium tetraborate 0.1 mM, pH 9) before a voltage was applied and the current, flow rate and pressure determined. Each reading was measured in triplicate and in order of increasing voltage. The flow rate within the channel was calculated by multiplying the cross-sectional area of the channel with the velocity of the fluid and the current was a determined directly by Labview software. The pressure was determined by pumping the liquid in a vertical direction against gravity until it became stationary, the measured height allowed for calculation of the backpressure.

4.4. Results and discussion

4.4.1 Electroosmotic Pump Design and General Considerations

EOPs use a potential difference to generate fluid motion from a charged surface. In contrast with most EOPs presented in the literature, the proposed EOP has both fluidic connections of the pump grounded, and the potential applied to drive flow applied to a third electrode positioned centrally in the pump. To prevent the cathodic and anodic flows from cancelling each other out, the EOP is asymmetrical in surface area, rather than surface charge. [16, 17, 19] This is by having 1 mm I.D. channels on each side of the central live electrode, with an empty channel at one end and an 3D printed porous mesh at the other to provide a high surface area. Furthermore, previous studies have shown that an increase in the surface area by introducing high density multiple pumping channels allows the generation of high electric field across the pumping system at relatively low voltage [37]. The design and a photograph of the 3D printed

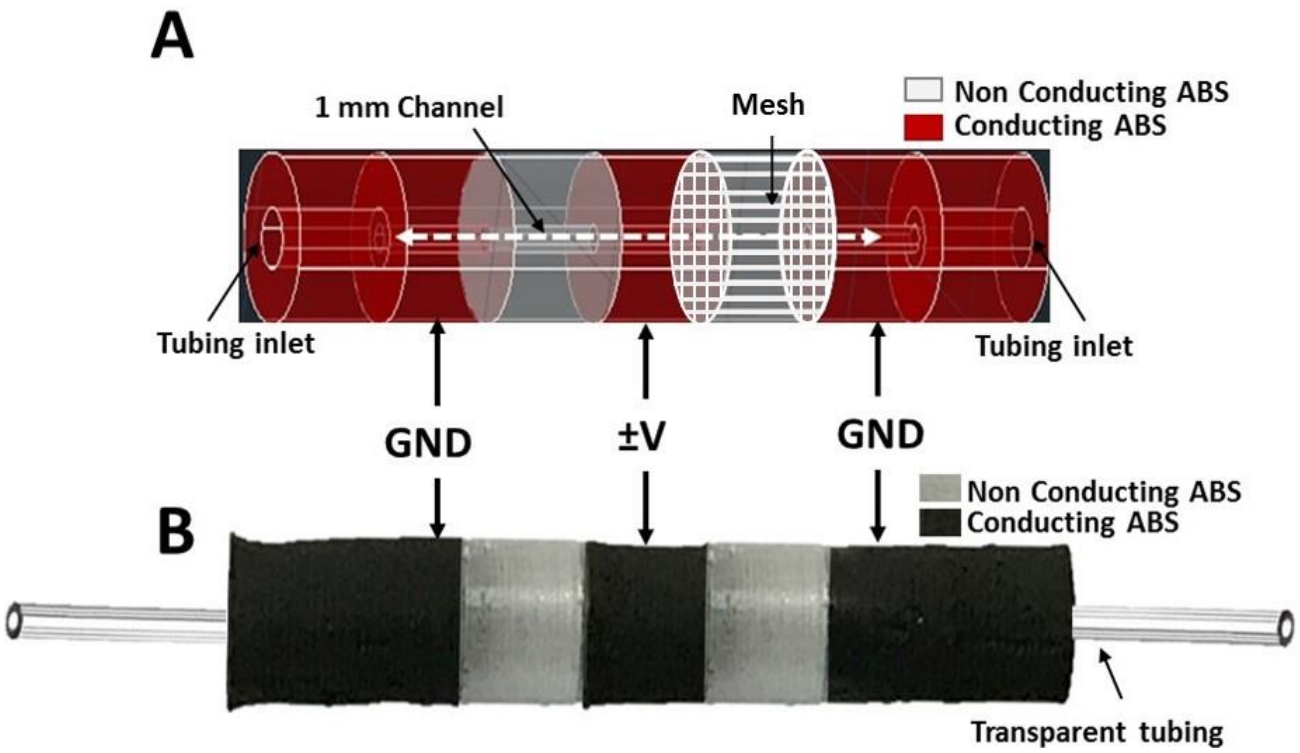

Fig.4.1. (a) CAD design of the electroosmotic pump and illustration of its different parts (b) 3D printed

EOP are shown in Fig.4.1. The EOP is non-terminal and is based on a three electrode design (ground, voltage, ground) to decouple the electric field used to drive the flow from the rest of the system. When a positive voltage is applied to the middle electrode, the EOF is directed towards middle electrode from the ground electrodes. Owing to the higher surface area in the side with the 3D printed mesh, the EOF generated in the mesh is greater than the EOF generated in the 1 mm I.D. channel, allowing for a net flow to be produced by the pump. The EOPs design specifications are summarized in Table 4.1.

4.4.2. Fabrication and Optimization of Mesh

The key concept behind the presented EOP is the different surface area in the two pumping regions. In 3D printing, infills are often used to reduce the amount of material inside an object, reducing the cost

Table 4.1. Key specifics of the fabricated electroosmotic pump

Electroosmotic Pump designs	➢ Two electrode with single channel ➢ Three electrode ➢ Two electrode with mesh
Fabrication material	Conducting and Clear ABS
Volume of the pump	19.64mm^3
Buffer	$Na_2B_4O_7 \cdot 10H_2O$ (0.1 mM)
pH	9
Internal diameter of the single channel	1 mm
Internal diameter of the mesh	100 µm
Outer diameter of the all pumps	5 mm
Length of the mesh	5 mm
Length of each electrode	5 mm
Total length of the pump	25 mm
Voltage kV	0.1-0.5

of the component in terms of material cost and printing time. In the context of this manuscript, infill meshes were used to provide a simple approach to directionally increase the surface area and therefore flow rate, in comparison to previous efforts where surface area was increased by a complex and time consuming process of packing columns sodium silicate and non-porous silica particles in the capillary, baking it at a high temperature (350 ^oC) and then pasteurizing [37].

To evaluate the potential of the use of an infill mesh for increasing the surface area as required for the EOP, infill meshes were printed to evaluate the homogeneity and size of the mesh. This was realized using the infill percentage, the parameter normally used to define the amount of the material inside the printed structure. A 5 mm cube was printed with the infill increasing from 50-80% and the extrusion

width increasing from 150-250 μm. The minimum extrusion width possible was 150 μm. The results are summarized in Fig.4.2, and as anticipated increasing the infill percentage decreases the void size. This is most easily visualized when looking down the column with an extrusion width of 250 μm. Increasing the extrusion width results in larger voids being produced, as illustrated by the images with 50% infill. A considerable variability in the consistency and repeatability of the printed porous structure was noted, with the least regular structures produced with a width of 150 μm. Using a width of 250 μm, the smaller extrudate is achieved by moving the printer quicker and stretching the filament before it hardens when cooled. We believe that the irregularity seen in some of the structures (Fig.4.2 (f)) for example) is due to making this structure using in-fill alone, which has to adjust the extruded filament position to achieve the infill amount and thus the movement of the printing head is not always uniform in the X and Y dimensions. This suggests that with a specifically designed 3D printer mesh with the thickness and spacing explicitly designed it may be possible to achieve smaller void sizes and is something that will be examined in the future.

The smallest and most uniform structure obtained using the infill approach was observed at 70 % infill (Fig.2(k)) and extrusion width of 250 μm, leaving 100 μm voids uniformly distributed throughout the structure. These settings were used for the fabrication of 3D printed EOP described below.

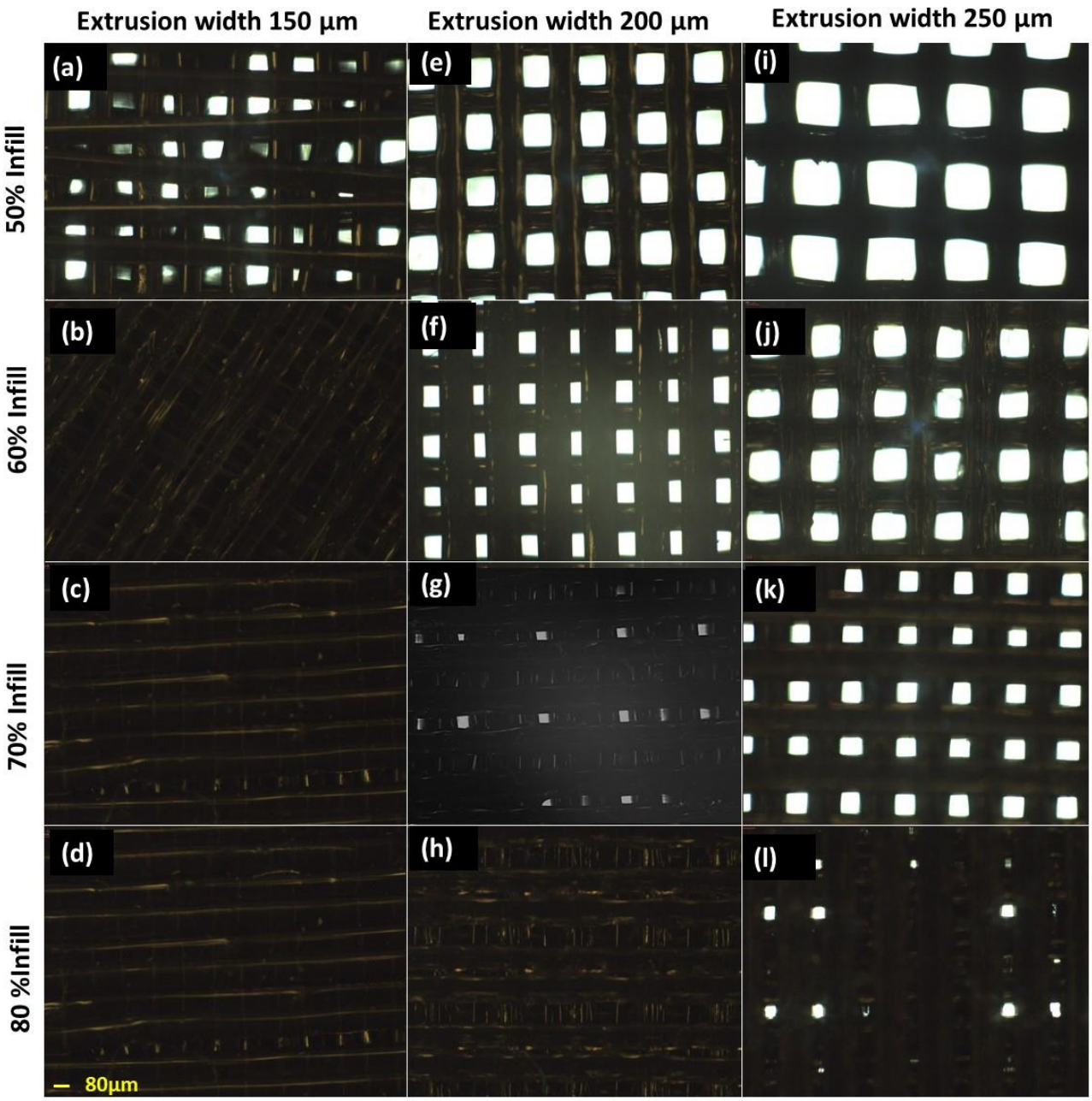

Fig.4.2. Evaluation of various printing parameters for the fabrication of mesh. Fig. 2(a-d) has 150 µm extrusion size and 50-80% infill size, Fig. 2(e-h) has 200 µm extrusion size and 50-80% infill size, Fig. 2(i-l) has 250 µm extrusion size and 50-80% infill size

4.4.3. Performance of the Pump

When designing an EOP, the flow rate is directly proportional to the voltage applied, and thus a higher voltage provides higher flow rates and pressures. However, the amount of electric current generated is one of limiting factors of these pumps, as the Joule heat, heat produced due to the passage of current through conductive ABS, can cause significant bubble generation and/or can damage the sample [38]. Therefore, it is important to understand the operational voltage range of the pump. To determine the operational voltage of the 3D printed EOP, the recorded electric current is visualized as a function of applied voltage when pumping 0.1 mM sodium tetraborate at pH 9.0 using the 3D printed EOP. A linear increase in current from 15 μA – 68 μA was observed with an increase in voltage from 100 – 500 V. Voltages higher than 500 V were not examined because our aim was to develop a low voltage EOP as higher voltages require larger power supplies which reduces portability and ease of use. [39] The use of lower voltages (and hence lower currents) also results in lower bubble production due to electrolysis [40]. Additionally, to further reduce the bubble formation, conductive ABS material was selected as previous reports have shown that conductive polymers can be employed to avoid bubble formation e.g. Kumar et al used, polyaniline wrapped aminated graphene electrodes in combination with a silica frit to produce a long-lasting, non-gassing EOP [41]. Similarly, Bengtsson et al. 2014 used partially-oxidized poly(3,4-ethylenedioxythiophene) to minimize bubble formation due to the ability of this polymer to be oxidized or reduced when the voltage is applied, therefore minimizing the electrolysis of the water/buffer. Therefore, for this study composite of ABS with carbon fiber and carbon black was chosen as the electrode material due to the demonstrated ability of carbon based conductive materials to

undergo reversible redox reaction under the influence of applied voltage [42] hence mitigating the liquid electrolysis.

In order to validate the design of the 3D printed EOP, the flow rate and direction of the fully integrated pump (pump C) was compared with the two pump halves, two electrodes and the single pumping channel (pump A), and the mesh and two electrodes (pump B). Fig. 3 shows the results of the flow rates

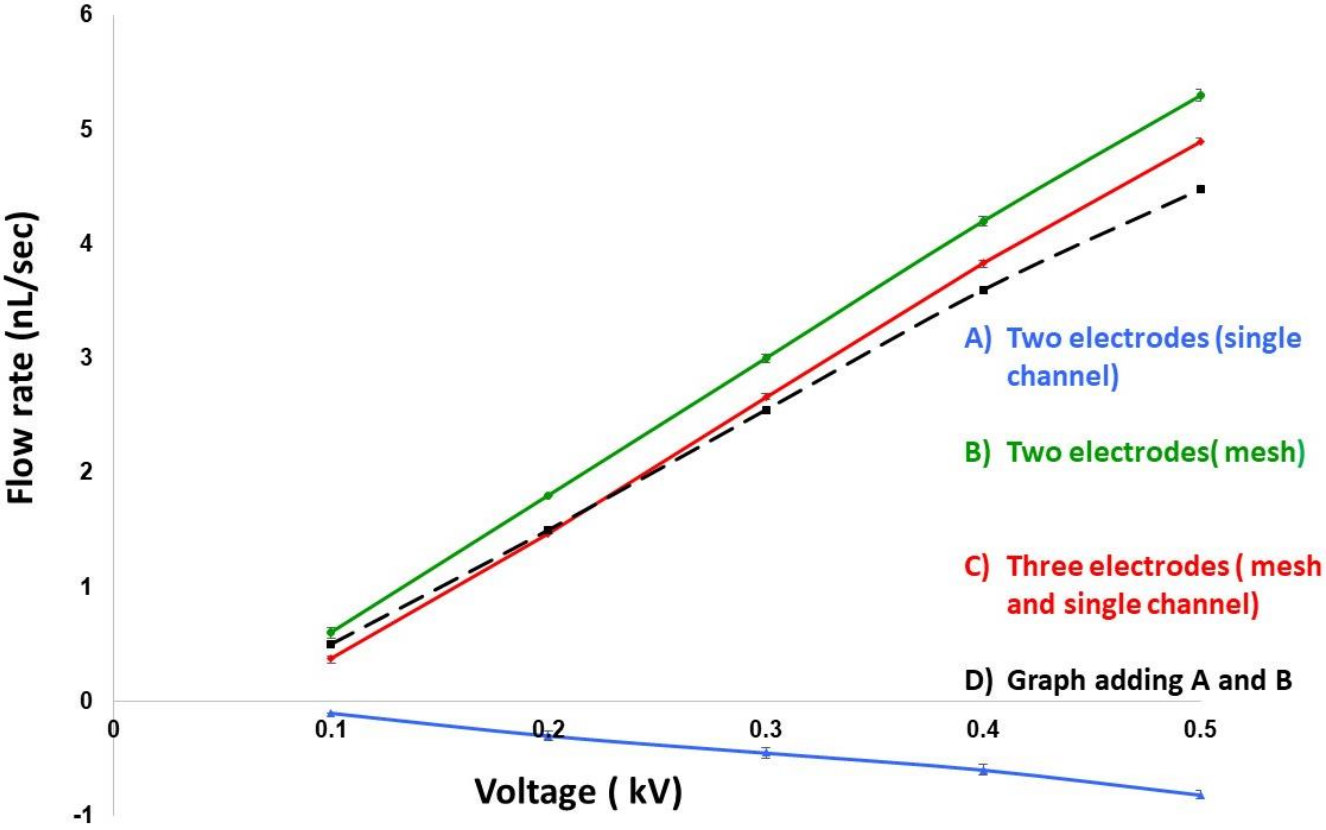

Fig.4.3. Graph of relationship between the flow rate and applied voltage (+ve). sodium tetraborate (0.1 mM buffer) with pH 9 is used. A shows the flow rate at different voltages with single channel pump. B shows the flow rate at different voltages with mesh pump. C shows the flow rate at different voltages with three electrode single and mesh channel pump. D shows adding the flow rate of pump A and D at different voltages.

for the three pumps, as well as the theoretical flow rate (pump D) when pump A and B are combined arithmetically. The figure shows a linear response in flow rate with voltage for all the fabricated EOPs with Pump A showing a 6-fold lower flow rate (0.1- 0.82 nL/sec) in comparison to pump B (0.6- 5.3 nL/sec). This increase in flow rate corresponds to the surface area as the surface area of the 3D printed mesh (714 mm^2) is approximately six times higher than the single channel (132 mm^2).

The resulting flow in the integrated 3D pump (pump C) is from the vector sum of the flow from pumps A and B which are directly opposing each other. The experimental flow rate range was 0.3- 4.9 nL/sec at voltages from 0.1 – 0.5 kV, which is approximately 16% less than the single mesh pump. This flow rate was slightly higher than the theoretical flow rate (pump D) which we attribute to the additional heat generated from the combination of two pumps when compared to A and B operated separately. The flow rate for the integrated 3D printed pump is similar to previously reported values and should therefore be useful for similar applications [5, 38, 43]. It should be noted that using the same EOP configuration and applying a negative voltage to the central electrode, the pump did not operate correctly. We believe that this is due to the liquid flow exiting both ends of the pump, leaving a slight vacuum in the pump which, with the electrolysis products, quickly filled with gas, disrupting the current and liquid flow and stopping liquid flow.

To be practically useful, the EOP has to be able to generate a sufficient pressure to drive fluid through an appropriate system [5, 44-46]. To determine the backpressure of the non-terminal 3D printed EOP, the pump was positioned such that the net flow was in an upward direction, opposing gravity. This way, the backpressure generated by the pump can be determined using the height at which the water becomes stationary. At 0.1-0.5 kv applied voltage pressures between 11- 255 Pa was achieved, with higher voltages higher pressures can be achieved. The pressure generated by 3D printed electroosmotic

pump is expected to be sufficient for microfluidic flow as demonstrated by previous reports on EOP for applications in microfluidics. For example, Du et al. fabricated a peristaltic micro pump driven by a rotating motor with magnetically attracted steel balls. The pump with one ball bearing of 4 mm achieved backpressures of 200 Pa, which was subsequently increased to 600 Pa by increasing to three ball bearings [47]. Similarly Xia et al fabricated an electroactive polymer based microfluidic pump with backpressure 350 Pa [48]. The back pressure of our pump could be increased by increasing voltage, however this was not examined as our focus was to demonstrate the capability of 3D printing to fabricate the complex EOP design consisting of asymmetric channels and integrated electrodes all in one piece to avoid the complicated fabrication procedure and the need for manual assembly of several parts. Further improvement in pressure require printing of smaller voids, which would result in a pump capable of generating a higher pressure. We have also previously demonstrated the ability to print porous membranes inside a fluidic device which will be used to decouple the electroactive surface from the fluidic channel to eliminate the issue of gas generation inside the pump. Together, we believe these improvements would provide a new possibility to create and design of fully 3D printed instrumentation.

4.5. Conclusion

Here we present a 3D printed multi-material non-terminal EOP using asymmetrical surface area to drive fluid flow. No other EOP is characterized in this unique mode of controlling flow on basis of surface area and fabricated in a single step by the combination of the two ground electrode. The novel design exploits the unique ability of 3D printing to define structures in 3 dimensions. Using a multi-material FDM printer, electrodes were seamlessly integrated with the fluidic structures in a single, automated manufacturing step. The performance of the 3D printed EOP was found to be comparable to other pumps, although

improvements in print resolution are required to make pumps that operate pressures> 255 Pa. Multi-material 3D printing provides the opportunity to produce highly customized devices with integrated complementary functionalities. With the presented EOP providing a means for fluid transport, 3D printed instrumentation for chemical analysis has moved a step closer.

4.6. References

[1] D.J. Laser, J.G. Santiago, A review of micropumps, J. Micromech. Microeng. 14 (2004) R35.

[2] N.-T. Nguyen, X.Y. Huang, T. Kok Chuan, MEMS-micropumps: A review, J. Fluids Eng. 124 (2002) 384-392.

[3] B.D. Iverson, S.V. Garimella, Recent advances in microscale pumping technologies: a review and evaluation, Microfluid. Nanofluid. 5 (2008) 145-174.

[4] V. Pretorius, B.J. Hopkins, J.D. Schieke, Electro-osmosis -New concept for high-speed liquid-chromatography, J. Chromatogr. A 99 (1974) 23-30.

[5] L.X. Chen, J.P. Ma, Y.F. Guan, An electroosmotic pump for packed capillary liquid chromatography, Microchem. J. 75 (2003) 15-21.

[6] L.X. Chen, J.P. Ma, Y.F. Guan, Study of an electroosmotic pump for liquid delivery and its application in capillary column liquid chromatography, J. Chromatogr. A 1028 (2004) 219-226.

[7] J.P. Kutter, S.C. Jacobson, J.M. Ramsey, Integrated microchip device with electrokinetically controlled solvent mixing for isocratic and gradient elution in micellar electrokinetic chromatography, Anal. Chem. 69 (1997) 5165-5171.

[8] P.C.H. Li, D.J. Harrison, Transport, manipulation, and reaction of biological cells on-chip using electrokinetic effects, Anal. Chem. 69 (1997) 1564-1568.

[9] A.G. Hadd, D.E. Raymond, J.W. Halliwell, S.C. Jacobson, J.M. Ramsey, Microchip Device for Performing Enzyme Assays, Anal. Chem. 69 (1997) 3407-3412.

[10] J. Linan, J. Mikkelsen, K. Jae-Mo, D. Huber, Y. Shuhuai, Z. Lian, Z. Peng, J.G. Maveety, R. Prasher, J.G. Santiago, T.W. Kenny, K.E. Goodson, Closed-loop electroosmotic microchannel cooling system for VLSI circuits, IEEE Transactions on Components and Packaging Technologies 25 (2002) 347-355.

[11] P.H. Paul, D.J. Rakestraw, Electrokinetic high pressure hydraulic system, in, ; SANDIA CORP, 2000, pp. Medium: ED.

[12] M.J. Pikal, The role of electroosmotic flow in transdermal iontophoresis, Adv. Drug Deliv. Rev. 46 (2001) 281-305.

[13] M. Agarwala, D. Bourell, J. Beaman, H. Marcus, J. Barlow, Direct selective laser sintering of metals, Rapid Prototyping Journal 1 (1995) 26-36.

[14] X. Wang, C. Cheng, S. Wang, S. Liu, Electroosmotic pumps and their applications in microfluidic systems, Microfluid. Nanofluid. 6 (2009) 145.

[15] Q. Lu, G.E. Collins, A fritless, EOF microchip pump for high pressure pumping of aqueous and organic solvents, Lab Chip 9 (2009) 954-960.

[16] C.Y. Gu, Z.J. Jia, Z.F. Zhu, C.Y. He, W. Wang, A. Morgan, J.J. Lu, S.R. Liu, Miniaturized Electroosmotic Pump Capable of Generating Pressures of More than 1200 Bar, Anal. Chem. 84 (2012) 9609-9614.

[17] C. He, J.J. Lu, Z. Jia, W. Wang, X. Wang, P.K. Dasgupta, S. Liu, Flow Batteries for Microfluidic Networks – Configuring An Electroosmotic Pump for Non-Terminal Positions, Anal. Chem. 83 (2011) 2430-2433.

[18] A. Brask, G. Goranovic, M.J. Jensen, H. Bruus, A novel electro-osmotic pump design for nonconducting liquids: theoretical analysis of flow rate-pressure characteristics and stability, J. Micromech. Microeng. 15 (2005) 883-891.

[19] W. Wang, C.Y. Gu, K.B. Lynch, J.J. Lu, Z.Y. Zhang, Q.S. Pu, S.R. Liu, High-Pressure Open-Channel On-Chip Electroosmotic Pump for Nanoflow High Performance Liquid Chromatography, Anal. Chem. 86 (2014) 1958-1964.

[20] I.M. Lazar, P. Trisiripisal, H.A. Sarvaiya, Microfluidic Liquid Chromatography System for Proteomic Applications and Biomarker Screening, Anal. Chem. 78 (2006) 5513-5524.

[21] T.T. Razunguzwa, A.T. Timperman, Fabrication and characterization of a fritless microfabricated electroosmotic pump with reduced pH dependence, Anal. Chem. 76 (2004) 1336-1341.

[22] V. Singhal, S.V. Garimella, A. Raman, Microscale pumping technologies for microchannel cooling systems, Appl. Mech. Rev. 57 (2004) 191-221.

[23] D.W. Hutmacher, M. Sittinger, M.V. Risbud, Scaffold-based tissue engineering: rationale for computer-aided design and solid free-form fabrication systems, Trends Biotechnol. 22 (2004) 354-362.

[24] A.M. Tothill, M. Partridge, S.W. James, R.P. Tatam, Fabrication and optimisation of a fused filament 3D-printed microfluidic platform, J. Micromech. Microeng. 27 (2017).

[25] U. Kalsoom, A. Peristyy, P. Nesterenko, B. Paull, A 3D printable diamond polymer composite: A novel material for fabrication of low cost thermally conducting devices, RSC Adv. 6 (2016) 38140-38147.

[26] B. Gross, S.Y. Lockwood, D.M. Spence, Recent advances in analytical chemistry by 3D printing, Anal. Chem. 89 (2017) 57-70.

[27] P. Sitthi-Amorn, J.E. Ramos, Y. Wangy, J. Kwan, J. Lan, W. Wang, W. Matusik, MultiFab: A machine vision assisted platform for multi-material 3D printing, ACM Trans. Graph. 34 (2015) 1-11.

[28] V. Gupta, P. Mahbub, P. Nesterenko, B. Paull, A new 3D printed radial flow-cell for chemiluminescence detection: Application in ion chromatographic determination of hydrogen peroxide in urine and coffee extracts, Anal. Chim. Acta 1005 (2018) 81-92.

[29] K.B. Anderson, S.Y. Lockwood, R.S. Martin, D.M. Spence, A 3D printed fluidic device that enables integrated features, Anal. Chem. 85 (2013) 5622-5626.

[30] F. Cecil, M. Zhang, R.M. Guijt, A. Henderson, P.N. Nesterenko, B. Paull, M.C. Breadmore, M. Macka, 3D printed LED based on-capillary detector housing with integrated slit, Anal. Chim. Acta 965 (2017) 131-136.

[31] U. Kalsoom, P.N. Nesterenko, B. Paull, Current and future impact of 3D printing on the separation sciences, Trends Anal. Chem. 105 (2018) 492-502.

[32] F. Li, N. Macdonald, R. Guijt, M. Breadmore, Using printing orientation for tuning fluidic behaviour in microfluidic chips made by fused deposition modelling (FDM) 3D printing, Anal. Chem. 89 (2017) 12805–12811.

[33] F. Li, P. Smejkal, N. Macdonald, R. Guijt, M. Breadmore, One-step fabrication of a microfluidic device with an integrated membrane and embedded reagents by multimaterial 3D printing, Anal. Chem. 89 (2017) 4701–4707.

[34] B.C. Gross, J.L. Erkal, S.Y. Lockwood, C. Chen, D.M. Spence, Evaluation of 3D printing and its potential impact on biotechnology and the chemical sciences, Anal. Chem. 86 (2014) 3240-3253.

[35] F. Li, N. Macdonald, R. Guijt, M. Breadmore, Increasing the functionalities of 3D printed microchemical devices by single material, multimaterial, and print-pause-print 3D printing, 19 (2019) 35-49.

[36] M. Macka, W.-C. Yang, P. Zakaria, A. Shitangkoon, E.F. Hilder, P. Andersson, P. Nesterenko, P.R. Haddad, Poly(tetrafluoroethylene) separation capillaries for capillary electrophoresis: Properties and applications, Journal of Chromatography A 1039 (2004) 193-199.

[37] X. Wang, S. Wang, B. Gendhar, C. Cheng, C.K. Byun, G. Li, M. Zhao, S. Liu, C.K. Byun, M. Zhao, Electroosmotic pumps for microflow analysis, Trends Anal. Chem. 28 (2009) 64-74.

[38] M. Gao, L. Gui, Development of a Multi-Stage Electroosmotic Flow Pump Using Liquid Metal Electrodes, Micromachines 7 (2016).

[39] J.L. Snyder, J. Getpreecharsawas, D.Z. Fang, T.R. Gaborski, C.C. Striemer, P.M. Fauchet, D.A. Borkholder, J.L. McGrath, High-performance, low-voltage electroosmotic pumps with molecularly thin silicon nanomembranes, Proc. Natl. Acad. Sci. USA 110 (2013) 18425-18430.

[40] S. Litster, M.E. Suss, J.G. Santiago, A two-liquid electroosmotic pump using low applied voltage and power, Sensor. Actuator. A Phys. 163 (2010) 311-314.

[41] R. Kumar, K. Jahan, R.K. Nagarale, A. Sharma, Nongassing long-lasting electro-osmotic pump with polyaniline-wrapped aminated graphene electrodes, ACS Applied Materials & Interfaces 7 (2015) 593-601.

[42] O.Ö. Ekiz, M. Ürel, H. Güner, A.K. Mizrak, A. Dâna, Reversible electrical reduction and oxidation of graphene oxide, ACS Nano 5 (2011) 2475-2482.

[43] M. Alexander, K. Smith, J. Stark, Voltage effects on the volumetric flow rate and thrust produced in electrospray propulsion systems, in: 29th International Electric Propulsion Conference, Princeton University, 2005, pp. 1-6.

[44] F.F. Zhang, R. Wang, T.T. Han, B.C. Yang, X.M. Liang, Fabrication of a novel cascade high-pressure electro-osmotic pump, Analyst 136 (2011) 2689-2691.

[45] F.Q. Nie, M. Macka, L. Barron, D. Connolly, N. Kent, B. Paull, Robust monolithic silica-based on-chip electro-osmotic micro-pump, Analyst 132 (2007) 417-424.

[46] J. Zheng, Z. Gao, W. Yuan, H. He, S. Yang, C. Sun, Development of pressurized liquid extraction and solid-phase microextraction combined with gas chromatography and flame photometric detection for the determination of organophosphate esters in sediments, J. Sep. Sci. 37 (2014) 2424-2430.

[47] M. Du, X.Y. Ye, K. Wu, Z.Y. Zhou, A peristaltic micro pump driven by a rotating motor with magnetically attracted steel balls, Sensors 9 (2009) 2611-2620.

[48] F. Xia, S. Tadigadapa, Q.M. Zhang, Electroactive polymer based microfluidic pump, Sens. Actuators A Phys 125 (2006) 346-352.

Graphical Abstract

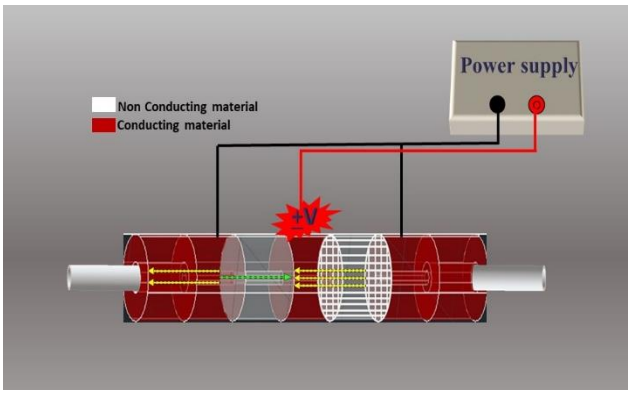

Chapter 5
Robustness and repeatability of 3D printed instrumentation.

Robustness and repeatability are very important factors for determining the accuracy of the results especially in fabrication the devices and instruments. Therefore, it is important to evaluate the reproducibility of the fabrication methods to ensure the repeatability and reliability of the newly developed devices and parts. 3D printing is seen as a feasible alternative manufacturing technique to produce consistent and reliable devices. Various studies have been taken to evaluate the repeatability; degree of agreement between dimensions of the printed objects, and accuracy; consistency between the dimensions of the printed parts and the dimensions intended for the designed mode i.e. STL file [1]. These studies carried on newly designed devices and models have demonstrated the ability of this technique to manufacture highly reproducible parts with remarkable accuracy and consistency [2]. For example, Prashanth and co-workers investigated the reproducibility 3D printing method for fabrication of the metallic parts using five different materials, three specimens manufactured using each material to evaluated the reproducibility of the fabrication process. Their results suggested highly reproducible objects can be printed given the properties of the material remain consistent [2]. Capel et al., fabricated highly reproducible fluidic devices using selective laser melting (SLM) printing technology, capable of manufacturing highly reproducible parts at a layer thickness as low as 20 µm [3].

The accuracy of the printing method is highly dependent of the printer's resolution. The resolutions of the commercially available 3D printers usually fall in the range of 0.05 to 0.30

mm, the print layer thickness i.e. the z-axis resolution of the printer. Furthermore, most of the printers offer the freedom to select z-axis resolution, for example 0.05-0.5 mm for FDM 3D printers, allowing to print fine objects with high repeatability and accuracy by selecting 0.05 mm layer thickness, in comparison to 0.5 mm which is usually used for quick printing of the larger sized objects. However, printing with low cost FDM printer is also susceptible to inaccuracies due to the underlaying printing process such as shrinkage/ and warping during the printing process. However, the success of a repeatable and accurate print is highly dependent on many factors such as material used, object design, chosen resolution, print orientation and printer calibration. Therefore, it is important to evaluate the repeatability and accuracy of the printing method for each given object before arriving to the conclusions.

This chapter highlights the experiments performed for investigating repeatability and accuracy of the all the newly designed and 3D printed components presented in previous chapters including photometric detection assembly, flow cell, and electro-osmotic pump.

3D printed detector housing described in chapter 2 provides a unique feature i.e. the self-alignment of the capillary or tubing in to the V-shaped part consisting of the slit. Alignment of the capillary is critical to photometric detection, therefore, the repeatability of the self-alignment feature of the detector assembly was evaluated for repeatability. The capillary (75 µm i.d.) was re-positioned and removed several times and the absorbance values were recorded for 0.125 mM solution of Orange G injected. Fig.5.1 shows the overlay of absorbance traces for 10 replicate measurements, with an RSD of 1.9 % for the absorbance at the peak maximum.

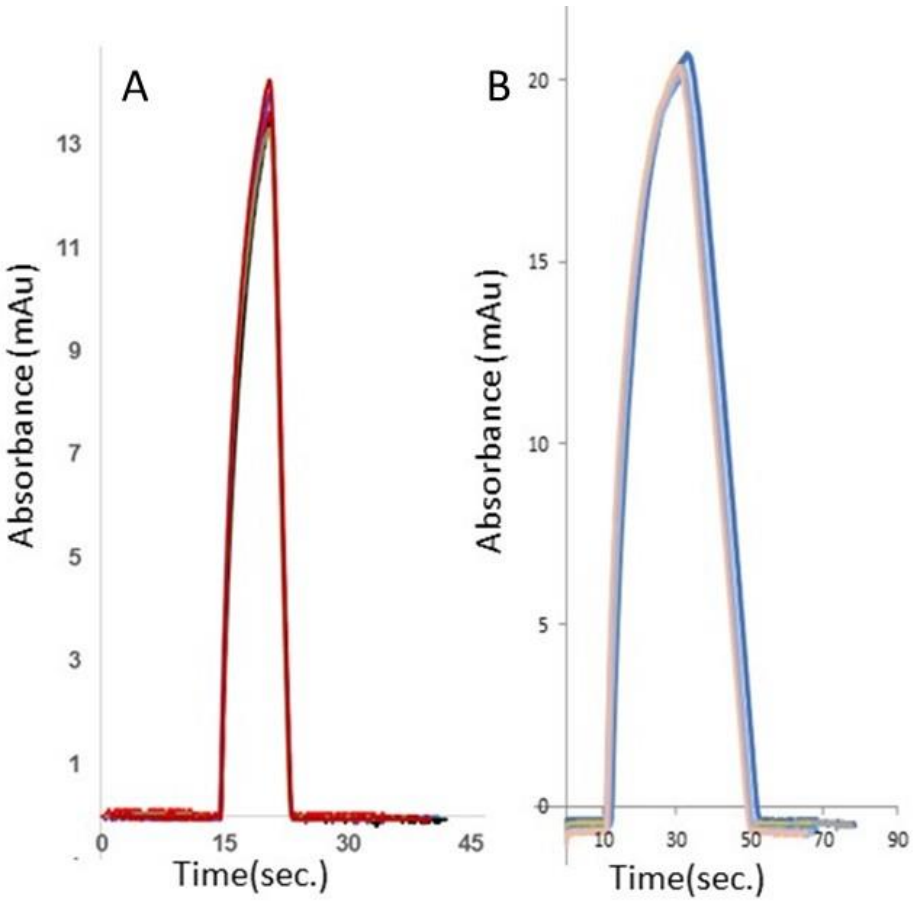

Fig.5.1A and B Absorbance *vs* time graph for 10 replicates of flow injection analysis of 15 µL Orange G (0.125mM) at 90 µL/min and 30 µL/min flow rate using 75 µm i.d capillary respectively

As previously discussed, the printing orientation plays a critical role in the printing of a repeatable and accurate print particularly for objects with fine dimensions. Therefore, the ability of various printing orientations to produce fine features of the detection assembly i.e. hollow slit with smallest possible printable dimension with high accuracy was evaluated. Fig.

Fig.5.1. Absorbance *vs* time graph for 10 replicates of flow injection analysis of 15 µL Orange G (0.125mM) at 90 µL/min flow rate using 75 µm i.d capillary.

2.2 (Chapter 2, page 69) shows a comparison of various printing orientations and agreement between the designed and printed parameters for each orientation for the slit size ranging from 250-50 μm with a length of 1000 μm. This experiment demonstrated that the minimum slit width (70 μm) could be printed when the slit length was parallel to print orientation/direction.

The repeatability and accuracy of the FDM 3D printer for the fabrication of photometric detector flow cell with integrated channel and slit described in chapter 3 was also investigated. For this purpose, four cells with path lengths ranging from ranging from 7.5-15 mm, were printed three times (n=3) and the length of the channel was observed under the microscope with the help of the coloured dye that was used to fill the channel length, please see figure 5.3. Furthermore, a comparison between designed and 3D printed path length and agreement in the printed objects in terms of % RSD is also provided in TabSle.S3.1. (Chapter 3, page 99). These experiments showed a good agreement between the design and printed pathlengths, with the average path length being ~ 99% of the design length. The repeatability of each design was also acceptable, with an error of % RSD ranging from 0.06 to 0.27 %. These

results demonstrate the excellent repeatability of the 3D printed flow cells and a close

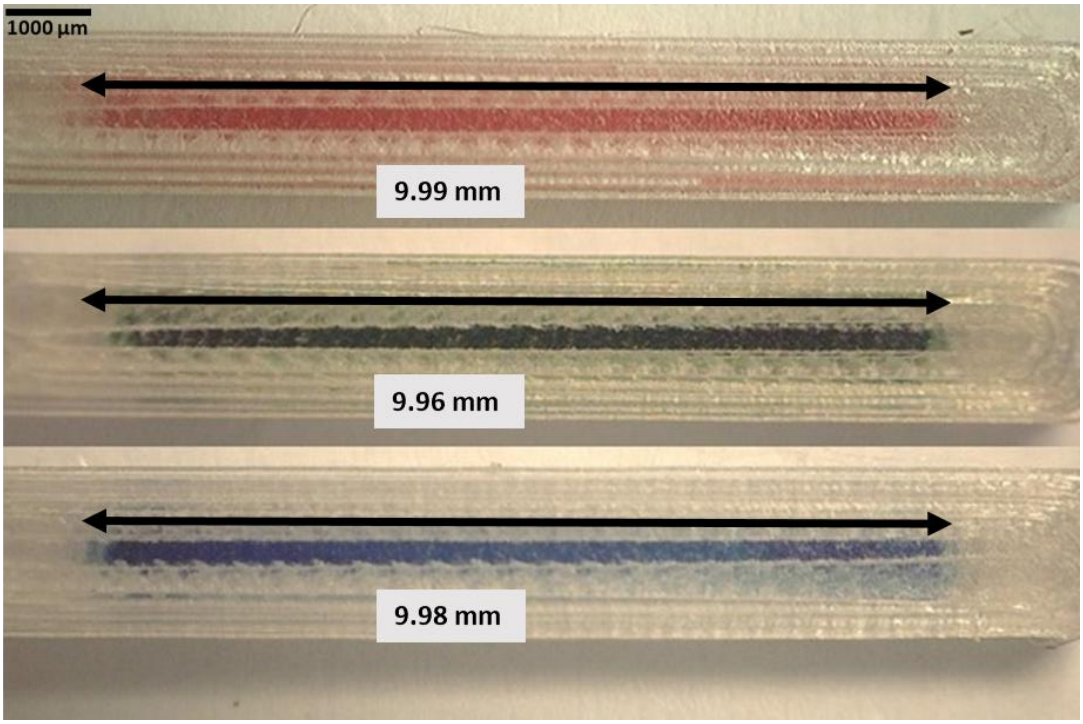

Fig. 5.3 Photographic images of the 3D printed pathlength, designed pathlength= 10mm (CAD design), the printed channel length is shown using different dyes.

agreement of the designed parameters with the printed parts for our device.

In chapter four non-terminal electroosmotic pump made by multi-material 3d printing was fabricated. The key concept behind the presented EOP is the different surface area in the two pumping regions. This was achieved by using the infill parameter, used to reduce the amount of material inside an object, of the 3D printing process. The ability of FDM 3D printer to fabricate the smallest channel size mesh with homogeneity was evaluated. A 5 mm cube was printed with the infill increasing from 50-80% and the extrusion width increasing from 150-

250 µm. The minimum extrusion width possible was 150 µm. The results are summarized in Fig.4.2 (Chapter 4, page 113), and as anticipated increasing the infill percentage decreases the void size. This is most easily visualized when looking down the column with an extrusion width of 250 µm. Increasing the extrusion width results in larger voids being produced, as illustrated by the images with 50% infill. A considerable variability in the consistency and repeatability of the printed porous structure was noted, with the least regular structures produced with a width of 150 µm. Using a width of 250 µm, the smaller extrudate is achieved by moving the printer quicker and stretching the filament before it hardens when cooled. We believe that the irregularity seen in some of the structures (Fig. 4.2 (f)) for example) is due to making this structure using in-fill alone, which requires adjustment of the extruded filament position to achieve the infill amount and thus the movement of the printing head is not always uniform in the X and Y dimensions. The smallest and most uniform structure obtained using the infill approach was at 70 % infill (Fig.4.2(k)) and extrusion width of 250 µm, leaving 100 µm voids uniformly distributed throughout the structure, therefore, these settings were used for the fabrication of 3D printed EOP described in detail chapter 4 section 4.4.2.

5.4. Conclusion

The rapid progress of 3D printing technology and its wide applications in all areas of research shows its ability to create prototypes with great accuracy and repeatability. Although present technologies allow 3D models to be produced with accuracy, the accuracy and repeatability is highly dependent on the design, dimensions of the object and the printer employed for fabrication. The present work investigated the accuracy and repeatability of a low cost FDM printer for the

fabrication of analytical devices including flow cells and pumps for applications in microfluidics. Our results indicated that highly accurate and repeatable devices can be manufactured using a low cost FDM 3D thus showing a great potential of this technology to manufacture fully automated, miniaturised analytical systems for microfluidics.

5.6. References

[1] E. George, P. Liacouras, F.J. Rybicki, D. Mitsouras, Measuring and Establishing the Accuracy and Reproducibility of 3D Printed Medical Models, Radiographics : a review publication of the Radiological Society of North America, Inc 37 (2017) 1424-1450.

[2] K.G. Prashanth, S. Scudino, R.P. Chatterjee, O.O. Salman, J. Eckert, Additive Manufacturing: Reproducibility of Metallic Parts, Technologies 5 (2017) 8.

[3] A.J. Capel, A. Wright, M.J. Harding, G.W. Weaver, Y.Q. Li, R.A. Harris, S. Edmondson, R.D. Goodridge, S.D.R. Christie, 3D printed fluidics with embedded analytic functionality for automated reaction optimisation, Beilstein Journal of Organic Chemistry 13 (2017) 111-119.

Chapter 6 Discussion, Conclusions and Direction of the Future Work

In this thesis, the potential of 3D printing to develop a fully automated integrated analytical instrument was investigated. This was achieved by manufacturing the main components of a simple analytical instrument, such as FIA, using low cost FDM 3D printer.

Fused Deposition Modelling (FDM) benefits from a wide range of available materials, multiple nozzles FDM printers allow combination of different materials into a single object. However, the smallest dimension that can be printed using commercial low-cost FDM is limited by the low-resolution and surface roughness issues associated with these printers. In the first step, a highly customised photometric detection assembly with integrated slit was fabricated using a low-resolution FDM 3D printer. Various printing orientations were explored to push the low-resolution limits of the FDM printer to fabricate the small size slit, as the performance of photometric detector is highly dependent on the slit. Investigation of various printing orientations showed that a slit as small as 70 µm can be fabricated when the printing orientation was parallel to slit, which is otherwise beyond printer's printing ability. This photometric detection assembly was integrated with a commercial CE system to perform photometric detection of inorganic metal ions in river water samples. The performance of newly printed device was found to be comparable to the commercial CE interface.

In the next step, a photometric flow cell with integrated slit and channels was designed and validated to avoid positioning of external tubing/ capillaries as previously required for 3D printed photometric detection assembly. Integration of the microchannel, the detection

window and the slit in a single device eliminates the need for manual alignment of fluidic and optical components, and hence improves repeatability. Multi-material 3D printing allowed the printing of the detection window using transparent material simultaneously with the device body using opaque material. Design optimisation by varying the slit dimension and optical path-length was also achieved. The optimised design was evaluated by determining stray light, effective pathlength and the signal to noise ratio using orange G. The sensitivity was improved by 80% in the process of optimization and approximately 20 fold improved from the previously reported detection assembly using a blue 470 nm LED as a light source.

Fluidic transport underpins most analytical systems. Electroosmotic pumps (EOPs) have been attractive for integration into portable instrumentation because of their instrumental simplicity, eliminating the need for moving parts. Previous reports on EOP rely on surface charge to control the flow direction and require external electrodes to apply the voltage. In this work, multi-material FDM 3D printing was used to fabricate a novel EOP design in which an asymmetrical increase in surface area was used to drive fluid flow. Meshing, parallel to flow, was used to dramatically increase in surface area at one side of the EOP, allowing the flow generated by the mesh to cancel out the flow generated in opposite direction. The flow rates generated by the two halves of the pump (high and low surface area) were determined individually, with the values confirming the hypothesis the net flow generated by the non-terminal EOP based on surface area is the sum of the EOF generated in the low and high surface area regions. The performance of the 3D printed EOP batter was found to be comparable to traditional EOP, although improvements in resolution are required to make pumps that operate at a higher pressure.

The ability to produce highly customised devices with integrated different functionalities within a single piece that multi-material 3D printing provides may be a simple and quick way for on demand production of EOP that could easily be integrated with instrumentation used for chemical analysis.

The future direction for this work will be to create an integrated 3D printed device including photometric flow cell, EOP and evaluate their performance as a simple analytical instrument. Furthermore, simultaneous printing of functional components of variable properties facilitates integration of various parts into a single object provides opportunities to minimise assembly parts and introduce automation. For example, the combination of pump, a mixing chamber, and the flow cell, will allow the creation of a simple fully integrated FIA instrument which could potentially be realised using the modern 5 nozzle FDM print